

# **An NMR Relaxometry Study of Heteronuclear Effects Upon Proton Transfer in Hydrogen Bonds**

Ilya Frantsuzov, MSci

Thesis submitted to the University of Nottingham  
for the degree of Doctor of Philosophy

· July 2010 ·

## Abstract

The inherent quantum-mechanical nature of the proton transfer process in hydrogen bonds has been investigated through its effects on the nuclear spin-lattice relaxation rate. The fast magnetic field-cycling techniques employed allowed a direct measure of the rate characterising this dynamic process, which is closely related to the potential energy environment experienced by the mobile proton.

Various heteronuclear effects from magnetic and non-magnetic nuclei outside the hydrogen bond were characterised. The contribution to proton tunnelling from the displacement of heavy atoms in the molecule is an important consideration within a complete description of the process. This interdependence was accurately measured for the carboxyl-group oxygen atoms in benzoic acid dimers through the isotope effect. Careful comparison of  $^{16}\text{O}$  and  $^{18}\text{O}$ -enriched benzoic acid relaxation allowed this relationship to be measured from the difference in low-temperature tunnelling rates.

Fluctuating dipolar interactions caused by proton transfer motion couples the Zeeman states of different nuclear species. The cross-relaxation occurring through this natural coupling was explored as a function of field in 2,4,6-trifluorobenzoic acid and  $^{13}\text{C}$ -enriched pure benzoic acid. Characterising the strength of this interaction endeavoured to broaden the comprehension of heteronuclear coupling and served as confirmation of the model used.

Beyond the carboxylic acid dimer, this investigation also showed dynamic disorder in intermolecular short, strong hydrogen bonds of pyridine-3,5-dicarboxylic acid. This proton transfer mechanism was found to be strongly dependent on the molecular vibrational modes creating a pathway between two potential minima. A finite change in entropy between the proton sites ensured that greatest proton mobility occurred at intermediate temperature, between relatively stable configurations at the extremes of temperature.

A study of different sources of molecular dynamics within one compound showed the efficiency of field-cycling NMR at separating their contributions to relaxation. Dynamic rates from the proton transfer and methyl group rotation in 4-methylbenzoic acid were reliably extracted to the extent of identifying separate contributions from a small percentage of molecules around impurity centres.

# Acknowledgements

First and foremost I would like to thank my supervisor Professor Tony Horsewill for his tutelage and guiding wisdom throughout the course of my studies. This thesis is an extension of his hard work and dedication to this field of physics. Equally, my research group co-workers, Dr. Kuldeep Singh Panesar and Dr. Cheng Sun must be acknowledged for their support of my work, and numerous enlightening discussions on a variety of topics ranging from ping-pong to polarisation. Recognition should also be given to my partner Cheryl Nicklin for her generous emotional support during periods of difficulty.

The technical staff at The University of Nottingham Physics Department provided invaluable assistance to the practical aspects of my research. Namely, the electronics prowess of Bob Chettle, mechanical skills of David Holt, and a reliable supply of cryogens from Chris Pallender. Additionally, the expertise of IT specialists Andrew Wilson and Philip Hawker was greatly appreciated on many occasions.

I would like to further acknowledge the research teams of Dr. Ivana Evans at Durham University and Dr. Mark Johnson at the Institut Laue-Langevin for their fruitful collaboration, which led to some truly intriguing results.

Finally, I thank my family for inspiring me to achieve something worthwhile.

# Contents

<b>1</b>	<b>Introduction</b>	<b>1</b>
1.1	Proton Transfer in the Hydrogen Bond . . . . .	1
1.1.1	The Benzoic Acid Dimer . . . . .	2
1.2	NMR Relaxometry . . . . .	3
1.2.1	Heteronuclear Effects . . . . .	3
1.3	Thesis Layout . . . . .	4
<b>2</b>	<b>Theory</b>	<b>6</b>
2.1	Fundamentals of NMR . . . . .	6
2.2	Asymmetric Double-Minimum Potential Model . . . . .	11
2.2.1	Autocorrelation and Spectral Density Functions . . . . .	13
2.2.2	Dipole-Dipole Spin-Lattice Relaxation . . . . .	14
2.2.3	Heteronuclear Effects . . . . .	17
2.3	Heteronuclear Relaxation Matrix . . . . .	22
2.3.1	Single-Crystal . . . . .	23
2.3.2	Isotropic Powder . . . . .	29
2.4	Carboxylic Acid Dimers . . . . .	33
2.5	The Methyl Rotor Model . . . . .	35
<b>3</b>	<b>Experimental Details</b>	<b>37</b>
3.1	Field-Cycling NMR . . . . .	37
3.1.1	Field-Cycling Magnet . . . . .	38
3.1.2	Cryostat and Variable Temperature Insert . . . . .	39
3.1.3	Probes . . . . .	40
3.1.4	Spectrometer . . . . .	42
3.2	Data Processing . . . . .	43
3.2.1	Fitting Equations . . . . .	43
3.3	Pulse Sequences . . . . .	46

## CONTENTS

---

3.3.1	Static-Field Homonuclear Saturation Recovery Pulse Sequence . . . . .	47
3.3.2	Homonuclear Saturation Recovery Pulse Sequence . . . . .	49
3.3.3	Homonuclear Polarisation Recovery Pulse Sequence . . . . .	50
3.3.4	Heteronuclear Saturation Recovery Pulse Sequence . . . . .	52
3.3.5	Zero-Field Heteronuclear Saturation Recovery Pulse Sequence . . . . .	53
3.3.6	Cross-Relaxation Pulse Sequence . . . . .	54
<b>4</b>	<b>The Isotope Effect</b>	<b>56</b>
4.1	Introduction . . . . .	56
4.2	Experimental Procedure . . . . .	58
4.3	Results . . . . .	60
4.3.1	Spectral Density Amplitudes . . . . .	61
4.3.2	Proton Transfer Correlation Rates . . . . .	62
4.4	Summary . . . . .	64
<b>5</b>	<b>Heteronuclear Cross-Relaxation</b>	<b>69</b>
5.1	Introduction . . . . .	69
5.2	Experimental Procedure . . . . .	72
5.3	Results . . . . .	74
5.3.1	$^{13}\text{C}$ -Benzoic Acid . . . . .	75
5.3.2	2,4,6-Trifluorobenzoic Acid . . . . .	78
5.4	Summary . . . . .	81
<b>6</b>	<b>Short, Strong Hydrogen Bond Motion</b>	<b>82</b>
6.1	Introduction . . . . .	82
6.2	Experimental Procedure . . . . .	87
6.3	Results . . . . .	89
6.3.1	Spectral Density Function . . . . .	90
6.3.2	Further Data Analysis . . . . .	92
6.3.3	Data Modelling . . . . .	95
6.4	Summary . . . . .	96
<b>7</b>	<b>Multiple Relaxation Sources</b>	<b>101</b>
7.1	Introduction . . . . .	101
7.2	Experimental Procedure . . . . .	103
7.3	Results . . . . .	104

*CONTENTS*

---

7.3.1	Data Modelling . . . . .	107
7.4	Summary . . . . .	108
<b>8</b>	<b>Summary and Concluding Remarks</b>	<b>115</b>
	<b>Bibliography</b>	<b>118</b>

# List of Figures

2.1	Zeeman splitting of a spin-1/2 particle. . . . .	9
2.2	Diagrammatic representation of the double-minimum potential. . . . .	11
2.3	Spherical polar coordinate geometry of proton transfer with respect to the dipolar Hamiltonian. . . . .	13
2.4	Zeeman splitting of two coupled spins-1/2. . . . .	15
2.5	Relaxation pathways between Zeeman reservoirs in a heteronuclear system. . . . .	18
2.6	Lorentzian functions $L(\omega)$ and $L(2\omega)$ . . . . .	32
2.7	Correlation rate dependence of the Lorentzian function $L(\omega)$ . .	32
2.8	Tautomeric forms of benzoic acid. . . . .	33
3.1	Magnetic field switching profiles. . . . .	39
3.2	Cryostat and variable-temperature insert. . . . .	40
3.3	Probe head structure. . . . .	41
3.4	Heterodyne spectrometer design. . . . .	42
3.5	Static-field homonuclear saturation recovery pulse sequence. .	47
3.6	Example of saturation recovery data. . . . .	48
3.7	Homonuclear saturation recovery pulse sequence. . . . .	49
3.8	Homonuclear polarisation recovery pulse sequence. . . . .	50
3.9	Example of polarisation recovery data. . . . .	51
3.10	Heteronuclear saturation recovery pulse sequence. . . . .	52
3.11	Zero-field heteronuclear saturation recovery pulse sequence. .	53
3.12	Cross-relaxation pulse sequence. . . . .	54
3.13	Example of cross-relaxation experiment data. . . . .	55
4.1	$^{16}\text{O}$ and $^{18}\text{O}$ benzoic acid dimers. . . . .	59
4.2	Isotope effect on the intramolecular bond lengths. . . . .	62
4.3	Spectral densities of $^{16}\text{O}$ -BA and $^{18}\text{O}$ -BA at 23 K - 80 K. . .	65

---

*LIST OF FIGURES*

---

4.4	Spectral densities of $^{16}\text{O}$ -BA and $^{18}\text{O}$ -BA at 13 K - 20 K. . . . .	66
4.5	Spectral density amplitudes of $^{16}\text{O}$ -BA and $^{18}\text{O}$ -BA. . . . .	67
4.6	Correlation rates of $^{16}\text{O}$ -BA and $^{18}\text{O}$ -BA. . . . .	68
5.1	2,4,6-Fluorobenzoic acid dimer. . . . .	70
5.2	$^{13}\text{C}$ benzoic acid dimer. . . . .	71
5.3	Cross-relaxation rate of $^{13}\text{C}$ -BA. . . . .	76
5.4	Cross-relaxation magnetisation recoveries of $^{13}\text{C}$ -BA. . . . .	77
5.5	Cross-relaxation rate of 2,4,6-FBA. . . . .	79
5.6	Spin-lattice relaxation rates of 2,4,6-FBA as a function of temperature. . . . .	80
6.1	Pyridine-3,5-dicarboxylic acid molecules. . . . .	83
6.2	PES along the proton transfer coordinate in the hydrogen bond of 3,5-PDA. . . . .	84
6.3	Multi-dimensional PES of the 3,5-PDA hydrogen bond. . . . .	86
6.4	Spectral densities of 3,5-PDA. . . . .	97
6.5	Spin-lattice relaxation rates of 3,5-PDA as a function of temperature. . . . .	98
6.6	Spectral density amplitudes of 3,5-PDA (non-zero entropy term). . . . .	99
6.7	Spectral density amplitudes of 3,5-PDA (zero entropy term). . . . .	100
7.1	4-Methylbenzoic acid dimer. . . . .	101
7.2	Crystal structure of neighbouring 4-MBA molecules. . . . .	102
7.3	Spin-lattice relaxation rate of 4-MBA as a function of temperature. . . . .	110
7.4	Spectral densities of 4-MBA at 24 K - 83 K. . . . .	111
7.5	Spectral densities of 4-MBA at 13 K - 23 K. . . . .	112
7.6	Correlation rates of 4-MBA. . . . .	113
7.7	Spectral density amplitudes of 4-MBA. . . . .	114

# Chapter 1

## Introduction

### 1.1 Proton Transfer in the Hydrogen Bond

Hydrogen bonds were first proposed in the early 20th century to describe the discrepancies in bonding energies of certain compounds; most notably, the stability of water is entirely due to this source of intramolecular bonding. Subsequently, hydrogen bonding was found to be ubiquitous in nature and an essential component for life as we know it. For example, many large organic molecules and structures, such as proteins, are shaped by their intra and intermolecular hydrogen bonds. Although the work presented in this thesis focuses mainly on O–H $\cdots$ O hydrogen bonds, N–H $\cdots$ O bonds - which are more prevalent in biological molecules - are also explored in chapter 6.

Proton transfer is a mechanism via which a hydrogen nucleus (proton) undergoes translational motion from one stable site to another, usually breaking a covalent bond with the donor atom and forming a new one with the receptor in the process. Some hydrogen bonds, such as those found in carboxylic dimers, are conducive to proton transfer, but this process is not restricted to them.

All reactions at the atomic level are fundamentally governed by quantum-mechanical principles. However, in most cases such systems can be considered to be in the high-mass and high-temperature regime, and are described equally well in terms of classical mechanics, in accordance with the Correspondence Principle. Proton transfer in the hydrogen bond is chosen here to expose and study this underlying quantised nature because it satisfies certain conditions that would otherwise obscure it. Namely, the small proton mass compared to other nuclei allows it to have a proportionately large de Broglie wavelength. If the two stable sites between proton transfer configurations, typically 0.6 Å, are

of a comparable separation to this wavelength then significant overlap between the proton wavefunctions in each pocket state will occur. This process must then be considered in terms of the quantum tunnelling phenomenon through the interceding potential barrier, with the extent of wavefunction overlap being represented by the tunnelling matrix element. Although this manifestation of quantum principles can be observed at room-temperature, as a proton transfer rate well in excess of what should be classically possible, it is most pronounced at low temperature.

### 1.1.1 The Benzoic Acid Dimer

Carboxylic acid dimers formed between molecules of benzoic acid ( $C_6H_5COOH$ ) readily exhibit proton transfer in both bridging hydrogen bonds, and are the principal subject of the investigations presented in this thesis. This compound forms a good basis for exploring quantum-mechanical and nuclear spin phenomena in unison because in its pure form it is uncomplicated by other magnetic nuclear species apart from protons, and exhibits fast proton transfer rates even at temperatures approaching absolute zero. However, the system can be readily elaborated to explore more complex phenomena by isotopic enrichment and substitution of the aromatic-group hydrogens.

Even in a simple compound such as benzoic acid, the tunnelling dynamics are non-trivial. As explained in chapter 2, accurate modelling of proton transfer across the hydrogen bonds involves motion of the heavier atoms in the molecule. These specific molecular vibrational modes combine to create a multi-dimensional potential energy surface experienced by the mobile proton.

The crystal field, experienced by pure benzoic acid dimers in the condensed phase, induces a slight preference for one particular arrangement of the mobile protons over the other. In pure benzoic acid and the majority of its derivatives, this energy asymmetry ( $\gtrsim 50$  K) is much larger than the tunnelling matrix element (0.4 K [1]). As a result, incoherent tunnelling occurs between the two configurations, supported by crystal lattice phonon contributions, leading to the proton wavefunctions being relatively localised in their respective sites. At low temperature, the constant transition probability from the high-energy ground state to the low-energy one gives rise to a constant proton transfer rate, independent of temperature. However, the amplitude of these transitions is reduced somewhat by the Boltzmann population in the high-energy state.

## 1.2 NMR Relaxometry

A precise way of measuring the quantised environment in hydrogen bonds is to detect it indirectly through the phenomenon of spin-lattice relaxation. At the low temperatures of interest in this investigation, the samples studied were in the solid state, and the dominant source of relaxation was dynamic disorder in the hydrogen bond. Proton transfer provides an efficient mechanism for spin-lattice relaxation to occur by generating a local fluctuating dipolar field, that affects other magnetic species in their vicinity. The efficiency of this process, observed as a function of magnetic field using a field-cycling spectrometer, then gives a direct measure of the proton motion. From this information, the potential energy environment of the hydrogen bond, fundamental to its quantised motion, can then be inferred.

The lack of motional averaging of the intramolecular dipolar field in solid samples leads to significant broadening of the NMR absorption peak. A good degree of averaging can be re-instated to solids through magic-angle spinning, but is not necessary in the context of this investigation, since the spin-lattice relaxation can be measured from a broad lineshape regardless.

For a static solid sample, the strength of the dipolar interaction, and hence of the observed relaxation, is also dependent on the molecule orientation relative to the magnetic field. This orientation dependence can be negated by preparing the sample as an isotropic powder; the microscopic crystals in this case would be randomly aligned resulting in some average dipolar interaction strength. Alternatively, the molecular orientation can be restricted to a specific value by using a single crystal sample. If the compound crystallises readily, this approach can offer significant advantages in signal to noise ratio over a powder sample due to a higher density of spins, and a well-defined value of the relaxation rate rather than an average.

### 1.2.1 Heteronuclear Effects

The coupling between Zeeman reservoirs of different magnetic species has been of topical interest in the field of NMR since 1953, when the Overhauser effect was first reported as a method of transferring the inherently large electron spin polarisation to a weakly polarised nuclear spin reservoir [2]. This dramatic feat was achieved by irradiating the sample at a frequency matching the resonance between the electron and nuclear Zeeman levels, and effectively coupling the

two.

Instead of electron-nuclear spin coupling, several of the experiments presented here are concerned with inter-nuclear coupling through a fundamentally similar process. The dipolar field, created by stochastic hydrogen bond motion, includes components at appropriate coupling frequencies to facilitate cross-relaxation between different Zeeman reservoirs. Measurement of these cross-relaxation phenomena is relevant for understanding relaxation and the transfer of polarisation in complex molecules, where several magnetic species are naturally present.

Beyond the coupling of nearby magnetic species within a molecule, even magnetically neutral (spin-0) nuclei can have an observable effect on the NMR of proton transfer through the isotope effect. Proton tunnelling is complemented by vibrational modes of the molecule, to the extent that the other atoms in the molecule also possess tunnelling matrix elements. Changing the mass of these heavier nuclei affects their tunnelling matrix element accordingly, thereby distorting the resulting proton tunnelling behaviour.

### 1.3 Thesis Layout

Some theoretical background concerning the general aspects of low-resolution solid-state NMR and modelling of quantum molecular dynamics in a double-minimum potential are explored in chapter 2. The experimental techniques used to measure spin-lattice relaxation rates of the variety of samples studied during this investigation are covered in chapter 3. Also discussed in chapter 3 is the field-cycling spectrometer used to study relaxation across a range of temperatures and fields.

Utilising the isotope effect, the results in chapter 4 present a clear demonstration of how the carboxylic-group oxygen atoms in benzoic acid contribute to proton tunnelling. This chapter also serves as an introduction to the low-temperature dynamics observed in the model system of pure benzoic acid. Chapter 5 examines in detail the cross-relaxation behaviour in  $^{13}\text{C}$ -enriched benzoic acid, and fluorobenzoic acid. The proton transfer motion in short, strong hydrogen bonds, which interlink pyridine dicarboxylic acid molecules, is the subject of chapter 6. It is demonstrated that the robust double-minimum potential model is applicable even in this very different proton environment. Chapter 7 presents a study of the effectiveness of the field-cycling technique

## *CHAPTER 1. INTRODUCTION*

---

at separating and identifying relaxation components from multiple sources of molecular motion. Finally, a summary of conclusions from the experiments presented here can be found in chapter 8.

# Chapter 2

## Theory

This section will be used to review the theoretical understanding of nuclear magnetic resonance, concentrating on the spin-lattice relaxation mechanisms in solids; the relaxation due to proton transfer in carboxylic acid dimers being of greatest relevance to my investigation. More general descriptions of the topic can be found in textbooks [3, 4, 5].

### 2.1 Fundamentals of NMR

The origins of nuclear magnetic resonance lie in the intrinsic property of ‘spin’ possessed by all nuclei, inherited from their subatomic constituents. In that sense it is akin to mass and charge, but instead relates to the particle’s magnetic moment. The quantum mechanical representation of angular momentum and its allowed operations is found to be applicable to spin, hence the quantity is sometimes called spin angular momentum. Despite the name ‘spin angular momentum’ implying some sort of physical rotation in space, as was initially theorised to be its origin, the source of spin actually lies in relativistic quantum mechanics of the nucleus, but the nomenclature has remained.

The eigenstates of the spin angular momentum vector along an arbitrary direction, chosen to be the z-axis in cartesian coordinates, can be represented by two quantum numbers  $I$  and  $m_I$ , which can be thought of as the vector magnitude and its orientation relative to the chosen direction. The functions  $|I, m_I\rangle$  are orthonormal and form a good basis set for matrix operations, called the ‘Zeeman eigenbasis’. The operator for spin angular momentum along the z-axis is  $\hat{I}_z$ , such that

$$\hat{I}_z|I, m_I\rangle = m_I|I, m_I\rangle, \quad (2.1)$$

where  $m_I$  can take any of  $2I + 1$  eigenvalues in the range  $m_I = I, I - 1, \dots - I$ . If all the coordinates are taken into account by applying the total square angular momentum operator  $\hat{I}^2 = \hat{I}_x^2 + \hat{I}_y^2 + \hat{I}_z^2$ , then

$$\hat{I}^2|I, m_I\rangle = I(I + 1)|I, m_I\rangle. \quad (2.2)$$

The spin quantum number  $I$  is commonly referred to as the ‘spin’ of a particle, and can take integer or half-integer values including zero. In terms of the protons and neutrons comprising the nucleus, both of which are spin-1/2 ( $I = 1/2$ ), the nuclear spin  $I$  represents the total combined spin of these components depending on whether they are arranged parallel or antiparallel relative to each other. For example, a deuteron may have nuclear spin quantum numbers  $I = 0, 1$  given by the two possible configurations  $(\uparrow\downarrow)$  and  $(\uparrow\uparrow)$ . However, due to the large energy gaps between nuclear spin states, well in excess of those available at room temperature, in general only the ground state is populated. Thus in the context of NMR only the ground state spin will be relevant.

To quantify a particle’s spin in terms of SI units, the total spin angular momentum,  $S$ , is related to the spin quantum number,  $I$ , via Planck’s constant,

$$\hat{S} = \hbar\hat{I}. \quad (2.3)$$

By considering equations (2.2) and (2.3), we can say that the magnitude of the total spin angular momentum is

$$|S| = \hbar\sqrt{I(I + 1)}. \quad (2.4)$$

It has been shown from quantum mechanical theory that the magnetic moment,  $\mu$ , is proportional and parallel to the spin angular momentum according to

$$\hat{\mu} = \gamma\hat{S}, \quad (2.5)$$

where the ‘gyromagnetic ratio’,  $\gamma$ , is unique for each particle species. Table 2.1 is provided as a reference for the spin and gyromagnetic ratios of nuclear isotopes pertinent to this thesis.

Nuclear isotope	Spin quantum number, $I$	Magnetogyric ratio, $\gamma / \text{rad s}^{-1}\text{T}^{-1}$
$^1\text{H}$	1/2	$26.7522 \times 10^7$
$^{12}\text{C}$	0	
$^{13}\text{C}$	1/2	$6.7283 \times 10^7$
$^{14}\text{N}$	1	$1.9338 \times 10^7$
$^{16}\text{O}$	0	
$^{17}\text{O}$	5/2	$-3.6281 \times 10^7$
$^{18}\text{O}$	0	
$^{19}\text{F}$	1/2	$25.1815 \times 10^7$

Table 2.1: Nuclear isotopes relevant to this thesis and their spin properties.

Combining equations (2.3) and (2.5) we can now define the magnetic moment operator along the arbitrary  $z$ -direction as

$$\hat{\mu} = \gamma \hbar \hat{I}_z. \quad (2.6)$$

Applying a constant magnetic field  $B$  produces an interaction with the magnetic moment for which the Hamiltonian is

$$\hat{\mathcal{H}} = -\hat{\mu} \cdot \hat{B}. \quad (2.7)$$

If the applied field is then taken to be along the  $z$ -direction,  $B_0$ , then the Hamiltonian can be simplified to

$$\hat{\mathcal{H}} = -\gamma \hbar \hat{I}_z B_0. \quad (2.8)$$

Hence according to equation (2.1), the energy of the interaction is quantised according to the quantum number  $m_I$

$$E = -\gamma \hbar m_I B_0 \quad \text{where } m_I = I, I-1, \dots, -I. \quad (2.9)$$

This energy multiplet structure is called the ‘Zeeman splitting’, containing in total  $(2I + 1)$  energy levels separated by

$$\Delta E = \gamma \hbar B_0, \quad (2.10)$$

as shown in figure 2.1 for a spin-1/2 ( $I = 1/2$ ) nucleus.

Spin-1/2 nuclei such as hydrogen nuclei are the most studied in NMR, in this work and in the wider field. For convenience, the two Zeeman eigenstates

of such nuclei  $|1/2, 1/2\rangle$  and  $|1/2, -1/2\rangle$  are given the symbols  $|\alpha\rangle$  and  $|\beta\rangle$  respectively. Due to the negative sign in equation (2.7), the spins with positive gyromagnetic ratios tend to align parallel with the applied field, representing the lowest Zeeman state, and those with negative  $\gamma$  align antiparallel. The materials studied during this investigation were diamagnetic, indicating that their magnetic moments are induced by the applied field,  $B_0$ , and are not permanent. In the absence of an external magnetic field, for such a nucleon, the the Zeeman eigenstates are degenerate.

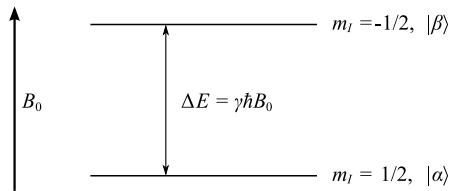


Figure 2.1: The Zeeman splitting of a spin-1/2 particle in a static magnetic field  $B_0$ . The  $|\beta\rangle$  eigenstate is a higher energy state relative to  $|\alpha\rangle$ .

Given this set of energy levels, it is possible to detect transitions between them using spectroscopic techniques. This is usually achieved by creating an alternating magnetic field perpendicular to  $B_0$ , supplied by photons at frequency,  $\omega_L$ , such that

$$\hbar\omega_L = \Delta E = \gamma\hbar B_0. \quad (2.11)$$

This frequency,  $\omega_L$ , is called the angular ‘resonance frequency’ or ‘Larmor frequency’ of the system, which for most nuclei at reasonable static fields (around 1 Tesla) is a few tens of Megahertz, in the radio frequency part of the spectrum.

Because of this energy difference, if the  $B_0$  field is maintained, then the relative spin populations of the two levels over a large number of spins will eventually be determined by the Boltzmann distribution. This would give rise to a finite bulk magnetisation parallel to the applied field,  $M_z = M_0$ , since the  $|\alpha\rangle$  eigenstate is more energetically favourable than  $|\beta\rangle$ . Such a stable state is then referred to as having come to ‘thermal equilibrium’ with the ‘lattice’, the lattice being a combination of all the molecular degrees of freedom - representing the sample temperature. The mechanism via which the Zeeman populations come to thermal equilibrium with their environment following a disturbance is hence called ‘spin-lattice relaxation’, characterised by the  $T_1$

relaxation time.

If  $N_\alpha$  and  $N_\beta$  are the number of spins in the  $|\alpha\rangle$  and  $|\beta\rangle$  states respectively then the polarisation of an ensemble of spins can be defined as

$$\langle \hat{I}_z \rangle = \frac{N_\alpha - N_\beta}{N_\alpha + N_\beta}. \quad (2.12)$$

This ensemble average expectation value will then be proportional to the induced magnetisation along  $B_0$  for the both the equilibrium and non-equilibrium cases,  $\langle \hat{I}_z \rangle \propto M_z$  and  $I_0 \propto M_0$ , so the two can be equated on relative terms.

## 2.2 Asymmetric Double-Minimum Potential Model

The work presented in this thesis will concentrate on the motion of hydrogen nuclei (protons) in an asymmetric double-minimum potential (DMP), via a process called ‘proton transfer’. This potential energy surface is created by the rest of the molecule’s atoms, which in relative terms can be considered stationary compared with the hydrogen nucleus, forming a ‘molecular lattice’. As will be discussed in subsections 2.2.1 and 2.2.2 the proton motion causes relaxation of the molecule’s nuclear spins through variation in the dipole-dipole interaction.

For the purposes of constructing a working model of relaxation, the potential energy surface (PES) can be simplified to a one-dimensional representation as shown in figure 2.2. In reality the PES is multi-dimensional with the motion of the proton coupled to various vibrational modes of the molecular lattice, which can aid or hinder proton transfer. Distortions of the molecule thus occur as part of the proton transfer process, as will be discussed in chapter 4. Figure 2.2 represents the potential energy measured along the reaction coordinate for proton transfer, which other investigations [6, 7] show cannot always be assumed to be the most direct path.

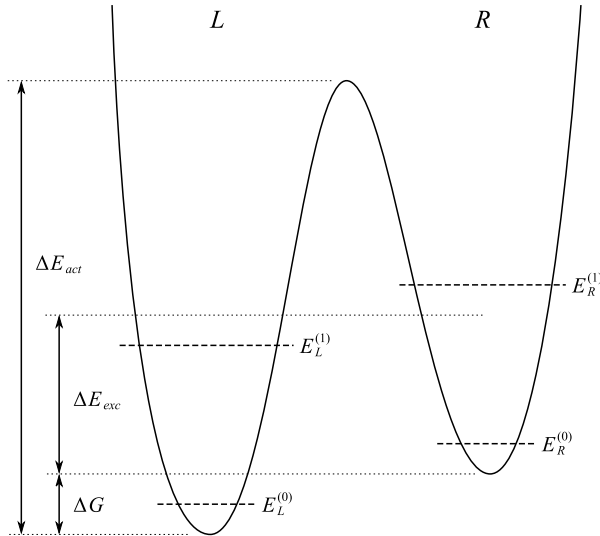


Figure 2.2: A diagrammatic representation of the double-minimum potential experienced by a hydrogen nucleus. The two potential energy wells are arbitrarily labelled *L* and *R*, in this figure corresponding to low and high energy respectively.  $\Delta E_{act}$  is the effective interceding barrier height,  $\Delta E_{exc}$  is the energy of the first excited state, and  $\Delta G$  is the difference in the Gibbs energy of the two DMP minima.

The classical mechanism for proton transfer is one of thermally activated ‘barrier hopping’ whereby the proton acquires enough energy to overcome the potential barrier and is free to occupy either site. In the high-temperature regime it has been shown [8] that these dynamics can very adequately be described by an Arrhenius law with an activation energy  $\Delta E_{act}$ . This effective activation energy from the phenomenological description is much smaller than the actual barrier height because the high-temperature dynamics include contributions from both barrier hopping and through-barrier tunnelling. At lower temperatures however, the transfer mechanism becomes increasingly dominated by quantum tunnelling through the potential barrier, observed experimentally [8, 9] as a much faster transfer rate than would be allowed by the classical mechanism.

In most cases the energy asymmetry,  $\Delta G$ , between the two potential wells is much larger than the tunnelling matrix element. As a result of this, tunnelling can only occur through incoherent pathways via interactions with a ‘heat bath’, containing phonons with energy comparable to  $\Delta G$  [10]. For a given temperature the Gibbs energy can be expressed as two terms,

$$\Delta G = \Delta H - T\Delta S. \quad (2.13)$$

The enthalpy change,  $\Delta H$ , is the energy released or gained during proton transfer, and  $\Delta S$  is the change in entropy associated with molecular lattice vibrations involved in proton transfer. Both of these quantities should be constant for a given molecular structure.

As mentioned earlier, the relaxation measured in the experiments presented here was due to modulation of the dipole-dipole coupling between nuclei. It is convenient now to define the geometry of such interactions in the context of proton transfer in a DMP. Consider hydrogen nucleus  $i$  in the molecular lattice experiencing a dipolar interaction with the mobile proton labelled  $j$ , moving between sites  $L$  and  $R$  in the DMP. The spatial components of the dipolar Hamiltonian depend on the relative positions of the two mobile proton sites relative to proton  $i$  at the origin, with  $B_0$  along the z-axis, as shown in figure 2.3 in terms of spherical polar coordinates  $(r, \theta, \phi)$ . When considering an isotropic powder average, it is useful to define an angle  $\alpha$  subtended by the two internuclear vectors.

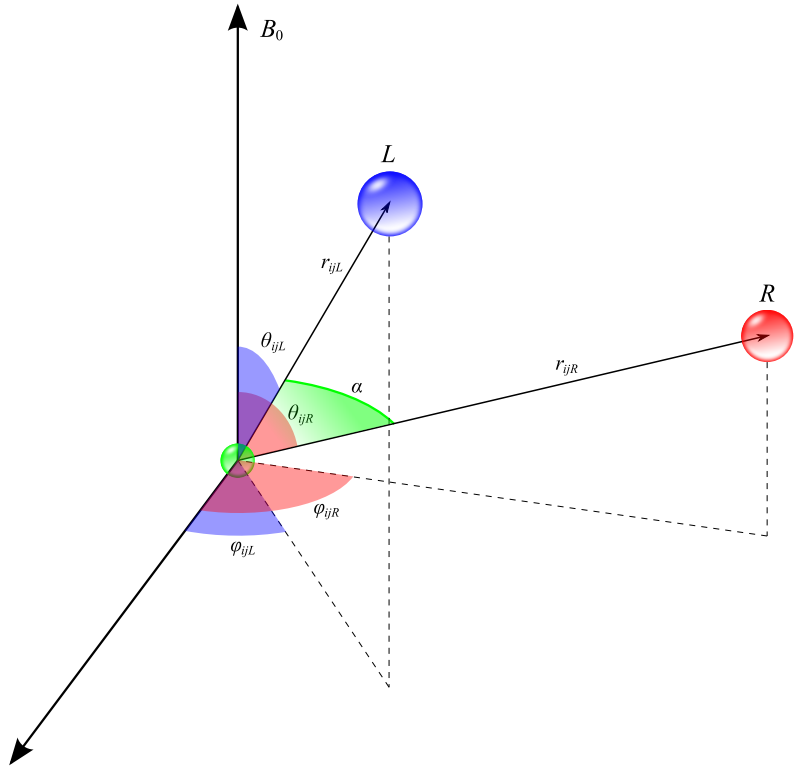


Figure 2.3: Application of the DMP proton transfer geometry with respect to the dipolar Hamiltonian. The spherical polar coordinates of the two mobile proton sites,  $L$  (blue) and  $R$  (red), are measured from proton  $i$  (green) at the origin.

### 2.2.1 Autocorrelation and Spectral Density Functions

Because the quantum tunnelling process in the asymmetric DMP is incoherent, requiring contributions from a phonon heat-bath, the proton transfer motion can be considered stochastic at low temperature. Similarly, it will be stochastic at high temperature during thermally activated transitions. Considering a classical interpretation of this proton transfer motion, where a particle moves between two well-defined states at random, we can write down the probability the proton will be in its starting position after a time  $\tau$  as an autocorrelation function

$$G(\tau) = \overline{p(t) \cdot p(t + \tau)}, \quad (2.14)$$

where  $p(t)$  and  $p(t + \tau)$  are the particle positions at those respective times, and the over-bar represents an ensemble average over many such systems. Numerical simulation can be used to show that the functional form of  $G(\tau)$  is

that of a decaying exponential,

$$G(\tau) = \text{const.} \times \exp\left(\frac{-|\tau|}{\tau_c}\right), \quad (2.15)$$

which will be large for small  $\tau$  and decrease with increasing  $\tau$  as the likelihood of the proton staying in its original position diminishes. The time constant,  $\tau_c$ , is called the ‘correlation time’ and is an average measure of how quickly proton transfer is occurring. Large correlation times indicate that the system changes slowly while small  $\tau_c$  is characteristic of more frequent motion. Taking a Fourier transform of the autocorrelation function we can resolve the frequency spectrum of the stochastic proton transfer motion,

$$J(\omega) = \int_{-\infty}^{\infty} G(\tau) \exp(-i\omega\tau) d\tau = \text{const.} \times \frac{\tau_c}{1 + \omega^2\tau_c^2}. \quad (2.16)$$

This function is called the ‘spectral density’ and has the form of a Lorentzian with half-width at half-maximum equal to  $\tau_c^{-1}$ .

### 2.2.2 Dipole-Dipole Spin-Lattice Relaxation

To make this analysis relevant to NMR we have to consider how the proton transfer motion would be observed macroscopically in terms of transitions between Zeeman energy levels. This can be achieved by inspecting the dipole-dipole interaction between a stationary nucleus  $i$  and proton  $j$  undergoing proton transfer. The magnetic field associated with the mobile proton will have some finite value experienced by nucleus  $i$ , and this value will change as proton transfer occurs. If this modulating magnetic field has a spectral density component perpendicular to  $B_0$  and at the resonance frequency  $\omega_L$  it will cause transitions between the Zeeman eigenstates. Through this dipolar coupling spins  $i$  and  $j$  can come to thermal equilibrium over time assuming they started in non-equilibrium.

To investigate this interaction in more detail the dipolar Hamiltonian, which has the following standard form, needs to be considered,

$$\hat{\mathcal{H}}_{DD} = \gamma_i \gamma_j \hbar^2 \left(\frac{\mu_0}{4\pi}\right) \sum_{m=-2}^2 \hat{A}^m F^m, \quad (2.17)$$

where  $m$  represents the total number of Zeeman state transitions between the two coupled nucleons.  $A^m$  and  $F^m$  represent the spin and spatial components

of the Hamiltonian respectively:

$$\hat{A}^0 = \hat{I}_z^i \hat{I}_z^j - \left(\frac{1}{4}\right) [\hat{I}_+^i \hat{I}_-^j + \hat{I}_-^i \hat{I}_+^j] \quad (2.18a)$$

$$\hat{A}^{\mp 1} = -\left(\frac{3}{2}\right) [\hat{I}_{\mp}^i \hat{I}_z^j + \hat{I}_z^i \hat{I}_{\mp}^j] \quad (2.18b)$$

$$\hat{A}^{\mp 2} = -\left(\frac{3}{4}\right) \hat{I}_{\mp}^i \hat{I}_{\mp}^j \quad (2.18c)$$

$$F^0 = r_{ij}^{-3} (1 - 3 \cos^2 \theta) \quad (2.18d)$$

$$F^{\mp 1} = r_{ij}^{-3} \sin \theta \cos \theta \exp(\pm i\phi) \quad (2.18e)$$

$$F^{\mp 2} = r_{ij}^{-3} \sin^2 \theta \exp(\pm 2i\phi) \quad (2.18f)$$

The operators  $\hat{I}_+$  and  $\hat{I}_-$  are raising and lowering operators respectively. If both nucleons are spin-1/2, then their coupled Zeeman eigenstates have the form  $|\alpha\beta\rangle$ , forming a four-level system. The dipolar Hamiltonian components can cause transitions between these energy levels as shown in figure 2.4.

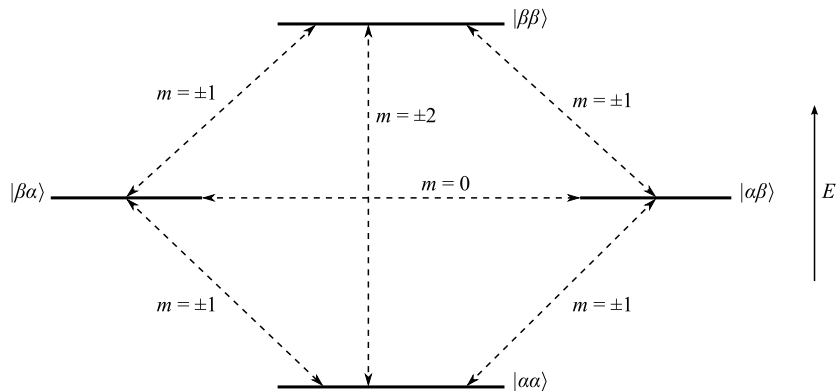


Figure 2.4: Zeeman energy levels of two coupled spins-1/2. The number of energy quanta required to make each transition is represented by  $m$ .

The autocorrelation function as expressed in equation (2.14) no longer applies in this case; instead of measuring the position change of one particle, it is the varying dipolar interaction between a mobile nucleus and another that is probed. Therefore, the autocorrelation function is expressed as an ensemble average in terms of the dipolar interaction spatial components,  $F^m$ ,

$$G^m(\tau) = \langle F^{m*}(t) F^m(t + \tau) \rangle, \quad (2.19)$$

where  $F^{m*}(t)$  represents the complex conjugate of  $F^m(t)$ . Consequently, the spectral density function can be defined as

$$J^m(\omega) = \int_{-\infty}^{\infty} \langle F^{m*}(t) F^m(t + \tau) \rangle \exp(-i\omega\tau) d\tau. \quad (2.20)$$

Since there are only two possible positions for the mobile proton,  $L$  and  $R$ , the ensemble average can be separated into components such as  $\langle F_L^{m*} F_R^m \rangle$ , representing the proton making a transition from  $L$  to  $R$  during time  $\tau$ , with which there is an associated probability depending on the system temperature. Then, assuming the functional form of equation (2.19) is the same as (2.15), the spectral density can be resolved further

$$J^m(\omega) = \frac{1}{2} \frac{4a}{(1+a)^2} \frac{\tau_c}{1 + \omega^2 \tau_c^2} [\langle F_L^{m*} F_L^m \rangle - \langle F_L^{m*} F_R^m \rangle - \langle F_R^{m*} F_L^m \rangle + \langle F_R^{m*} F_R^m \rangle]. \quad (2.21)$$

The factor  $4a/(1+a)^2$ , where  $a = \exp(\Delta G/k_B T)$ , is associated with the transition probability as a function of temperature [11]. These spectral density functions can be calculated precisely if the coordinates of the nuclei  $i$  and  $j$  are known from the molecular crystal structure. If the mobile proton  $j$  is coupled to numerous nucleons  $i$ , all the interactions need to be summed. However, it can be seen from equations (2.18) that the terms  $\langle F_L^{m*} F_R^m \rangle$  have an  $r^{-6}$  dependence and only the nearest interactions will give significant contributions. Section 2.3 shows the spectral density functions  $J^m(\omega)$  evaluated fully in terms of the dipolar contributions (2.18d - 2.18f) for both the single crystal and isotropic powder average cases.

Taking the energy levels of two coupled spins-1/2, figure 2.4, a set of coupled differential equations can be written to show how the population of each eigenstate depends on the transition probabilities between the levels. Further assuming that both spins are of the same nuclear species,  $\gamma_i = \gamma_j$ , the polarisation for an ensemble of such systems will be governed by

$$\frac{d}{dt} \langle \hat{I}_z \rangle = -\frac{1}{T_1} [\langle \hat{I}_z \rangle - I_0], \quad (2.22)$$

where  $\langle \hat{I}_z \rangle = \langle \hat{I}_z^i \rangle + \langle \hat{I}_z^j \rangle$  and  $I_0 = I_0^i + I_0^j$  [3]. The spin-lattice relaxation time,  $T_1$ , characterises the rate at which the coupled spins come to thermal

equilibrium. Equation (2.22) has a general solution of the form

$$\langle \hat{I}_z \rangle = I_0 \left( 1 - \exp \left( \frac{-t}{T_1} \right) \right). \quad (2.23)$$

Since the macroscopic magnetisation  $M_z$  is proportional to the total polarisation  $\langle \hat{I}_z \rangle$ , this equation describes the exponential recovery of the longitudinal magnetisation following a disturbance away from equilibrium.

It is possible to express the  $T_1$  time in terms of spectral density components  $J^m(\omega)$  that drive energy level transitions and contribute to spin-lattice relaxation, as will be seen in the following section. Analysis of these components by exploring the frequency domain, utilising a variable  $B_0$  field, can yield greater insight into the system dynamics than simply the temperature dependance.

### 2.2.3 Heteronuclear Effects

Consider now the case where the mobile hydrogen nucleus  $j$  experiences a dipolar interaction with a nearby spin-1/2 nucleus  $k$  of a different species (a ‘heteronucleus’). Similar to the homonuclear case in the previous section, consideration of the transition probabilities between the resulting four Zeeman eigenstates can lead to differential equations similar to (2.22) for the polarisation recovery [3]. This however is more complicated for the heteronuclear case because the equilibrium Boltzamnn population distributions are different for the two species, since  $\gamma_k \neq \gamma_j$ . It is convenient at this point to introduce the symbol  $S$  to represent the operators and polarisations of heteronucleus  $k$ , and reserve the use of  $I$  for homonuclei  $i$  and  $j$ , which in most cases are hydrogen nuclei. The coupled spin-lattice relaxation of an ensemble of homonuclear and heteronuclear spins is given by

$$\begin{bmatrix} \frac{d}{dt} \langle \hat{I}_z \rangle \\ \frac{d}{dt} \langle \hat{S}_z \rangle \end{bmatrix} = - \begin{bmatrix} \rho_I & \sigma_I \\ \sigma_S & \rho_S \end{bmatrix} \begin{bmatrix} \langle \hat{I}_z \rangle - I_0 \\ \langle \hat{S}_z \rangle - S_0 \end{bmatrix}, \quad (2.24)$$

where the relaxation matrix is composed of the heteronuclear and homonuclear parts as follows

$$\begin{bmatrix} \rho_I & \sigma_I \\ \sigma_S & \rho_S \end{bmatrix} = \begin{bmatrix} \rho_{II}^{IS} & \sigma_{IS}^{IS} \\ \sigma_{SI}^{IS} & \rho_{SS}^{IS} \end{bmatrix} + \begin{bmatrix} \rho_{II}^{II} & 0 \\ 0 & 0 \end{bmatrix}. \quad (2.25)$$

The terms  $\rho$  and  $\sigma$  are equivalent to spin-lattice relaxation rates. It can be seen that in the absence of a heteronuclear interaction, equation (2.24) can be simplified to that for the homonuclear case (2.22), where  $\rho_{II}^H = 1/T_1$ . The terms  $\sigma^{IS}$  are cross-relaxation rates at which the non-equilibrium polarisations of spins  $I$  and  $S$  equilibrate, in addition to equilibrating with the lattice.

To explain this further, the concept of a spin ‘reservoir’ needs to be introduced. When a set of spins  $I$  are placed in an excited state away from thermal equilibrium, the energy of those spins is said to be contained within the Zeeman spin reservoir  $I$ , which has a finite heat capacity. In this interpretation the lattice is considered to be a much larger reservoir at thermal equilibrium; such that if there is a flow of energy between the two, say through dipolar coupling due to proton transfer, then the  $I$  spin reservoir will tend towards the thermal equilibrium energy of the lattice reservoir. This can equivalently be considered in terms of equilibration of temperatures between a ‘hot’ reservoir  $I$  and a large lattice reservoir at the thermal equilibrium temperature. In a heteronuclear system, the  $S$  spin reservoir may also be coupled to the lattice, as well as to the  $I$  spin reservoir, through the dipolar interaction as shown in figure 2.5.

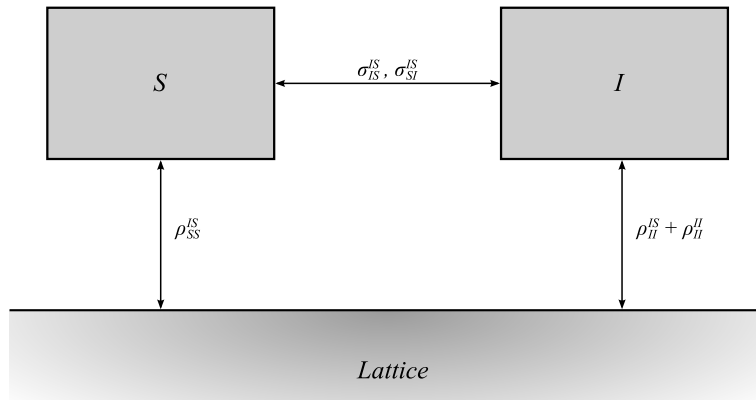


Figure 2.5: Relaxation pathways of the homonuclear ( $I$ ) and heteronuclear ( $S$ ) spin reservoirs between each other and the lattice.

General solutions of the coupled differential equations (2.24) following a disturbance away from equilibrium are weighted sums of two exponential

recoveries

$$\langle \hat{I}_z \rangle = I_0(1 + c_1^I \exp(-R_1 t) + c_2^I \exp(-R_2 t)), \quad (2.26a)$$

$$\langle \hat{S}_z \rangle = S_0(1 + c_1^S \exp(-R_1 t) + c_2^S \exp(-R_2 t)), \quad (2.26b)$$

where the weighting coefficients,  $c$ , are functions of the relaxation matrix elements and determined by the initial reservoir polarisation boundary conditions. For this reason, the preparation of the spin reservoirs prior to the recovery part of a pulse sequence is important in a heteronuclear sample, as will be discussed in chapter 3. Equations (2.26) indicate that the magnetisation recovery of a spin reservoir in a heteronuclear system will in general be bi-exponential. The relaxation rates  $R_1$  and  $R_2$  are the eigenvalue solutions of the relaxation matrix, given by

$$R_{1,2} = \frac{1}{2} \left( (\rho_I + \rho_S) \pm \sqrt{(\rho_I - \rho_S)^2 + 4\sigma_I\sigma_S} \right), \quad (2.27)$$

where the usual convention is that  $R_1 > R_2$ . The weighting coefficients  $c$  can be evaluated analytically by solving equations (2.26) with certain idealised initial reservoir polarisation boundary conditions.

For  $\langle \hat{I}_z \rangle_{t=0} = I_0$   $\langle \hat{S}_z \rangle_{t=0} = 0$ :

$$c_1^I = \frac{\gamma_S}{\gamma_I} \frac{\sigma_S}{R_2 - R_1} \quad \text{and} \quad c_2^I = -c_1^I, \quad (2.28)$$

$$c_1^S = \frac{\rho_S - R_2}{R_2 - R_1} \quad \text{and} \quad c_2^S = -(1 + c_1^S). \quad (2.29)$$

For  $\langle \hat{I}_z \rangle_{t=0} = 0$   $\langle \hat{S}_z \rangle_{t=0} = S_0$ :

$$c_1^I = \frac{\rho_I - R_2}{R_2 - R_1} \quad \text{and} \quad c_2^I = -(1 + c_1^I), \quad (2.30)$$

$$c_1^S = \frac{\gamma_I}{\gamma_S} \frac{\sigma_I}{R_2 - R_1} \quad \text{and} \quad c_2^S = -c_1^S. \quad (2.31)$$

For  $\langle \hat{I}_z \rangle_{t=0} = 0$   $\langle \hat{S}_z \rangle_{t=0} = 0$ :

$$c_1^I = \frac{\frac{\sigma_S \gamma_S}{\gamma_I} + \rho_I - R_2}{R_2 - R_1} \quad \text{and} \quad c_2^I = -(1 + c_1^I), \quad (2.32)$$

$$c_1^S = \frac{\frac{\sigma_I \gamma_I}{\gamma_S} + \rho_S - R_2}{R_2 - R_1} \quad \text{and} \quad c_2^S = -(1 + c_1^S). \quad (2.33)$$

Combining equations (2.26 - 2.33) it can be shown that if there is no

coupling between the homonuclear and heteronuclear reservoirs,  $\sigma_I = \sigma_S = 0$ , then equations (2.26) reduce to the same form as the homonuclear single exponential relaxation (2.23). There are three conditions under which the intrinsically bi-exponential recoveries of a heteronuclear spin system with a non-zero off-diagonal relaxation matrix element,  $\sigma$ , would appear to be single-exponential.

1. When there is less than an order of magnitude difference between the two spin-lattice relaxation rates,  $\log_{10}(R_1) \approx \log_{10}(R_2)$ , and the weighting coefficients of the measured species are non-zero,  $|c_1|, |c_2| > 0$ .
2. When the relaxation rates  $R_1$  and  $R_2$  are sufficiently different, but one of the weighting coefficients for the observed species is approximately zero,  $|c_1| \approx 0$  or  $|c_2| \approx 0$ .
3. A combination of both of the above conditions, where  $\log_{10}(R_1) \approx \log_{10}(R_2)$ , and  $|c_1| \approx 0$  or  $|c_2| \approx 0$ . In this case, any change in the minor relaxation rate, that associated with the weighting coefficient closest to zero, would be insignificant compared with the changes in the dominant relaxation rate. Hence, until the system changes to become either case 1 or case 2, the magnetisation recovery can be adequately described by the dominant component.

For cases 1 and 2, where the apparent single-exponential recovery cannot be well described by  $R_1$  or  $R_2$ , the observed magnetisation recovery follows some average effective relaxation time,  $T_1^{eff}$ . The exact value of this apparent relaxation time is difficult to model since it involves some degree of approximation and can also depend on the data fitting algorithm used. The following weighted sums of the relaxation rates show good correlation to the measured  $T_1^{eff}$  of test data sets:

$$T_1^{eff} \approx \frac{c_1 + c_2}{c_1 R_1 + c_2 R_2} \quad \text{for} \quad c_1 R_1 \not\approx -c_2 R_2, \quad (2.34)$$

$$T_1^{eff} \approx \frac{c_1/R_1 + c_2/R_2}{c_1 + c_2} \quad \text{for} \quad c_1 R_1 \approx -c_2 R_2. \quad (2.35)$$

With a field-cycling spectrometer it is possible to explore the frequency distribution of the spin-lattice relaxation rates. Each relaxation matrix element is composed of spectral density functions at a frequency appropriate to a

coupled Zeeman eigenstate transition contributing to that particular relaxation mechanism. The following equations can be derived by considering the dipolar Hamiltonian as a time-dependent perturbation of the Zeeman Hamiltonian [3].

$$\rho_{II}^{IS} = \frac{\gamma_I^2 \gamma_S^2 \hbar^2 S(S+1)}{12N_I} \left( \frac{\mu_0}{4\pi} \right)^2 [J^0(\omega_I - \omega_S) + 18J^1(\omega_I) + 9J^2(\omega_I + \omega_S)] \quad (2.36)$$

$$\sigma_{IS}^{IS} = \frac{\gamma_I^2 \gamma_S^2 \hbar^2 I(I+1)}{12} \left( \frac{\mu_0}{4\pi} \right)^2 [-J^0(\omega_I - \omega_S) + 9J^2(\omega_I + \omega_S)] \quad (2.37)$$

$$\sigma_{SI}^{IS} = \frac{\gamma_I^2 \gamma_S^2 \hbar^2 S(S+1)}{12} \left( \frac{\mu_0}{4\pi} \right)^2 [-J^0(\omega_S - \omega_I) + 9J^2(\omega_S + \omega_I)] \quad (2.38)$$

$$\rho_{SS}^{IS} = \frac{\gamma_I^2 \gamma_S^2 \hbar^2 I(I+1)}{12N_S} \left( \frac{\mu_0}{4\pi} \right)^2 [J^0(\omega_S - \omega_I) + 18J^1(\omega_S) + 9J^2(\omega_S + \omega_I)] \quad (2.39)$$

$$\rho_{II}^{II} = \frac{3\gamma_I^4 \hbar^2 I(I+1)}{N_I} \left( \frac{\mu_0}{4\pi} \right)^2 [J^1(\omega_I) + J^2(2\omega_I)] \quad (2.40)$$

Here,  $N_I$  and  $N_S$  are the numbers of nucleons  $I$  and nucleons  $S$  per mobile proton in the sample, including the mobile proton. These dilution factors result from efficient spin-diffusion within the homonuclear and heteronuclear spin reservoirs. The spectral densities  $J^m(\omega)$  are given by equation (2.21), and a full evaluation of the spatial dipolar components  $\langle F^m * F^m \rangle$  for each relaxation matrix element can be found in section 2.3. Also, the Lorentzian spectral density function is symmetric about  $\omega = 0$ , such that  $J(\omega) = J(-\omega)$ .

Note that in equations (2.36 - 2.39) there is a zero-quantum transition contribution. These are present because in the heteronuclear system the coupled Zeeman eigenstates  $|\alpha\beta\rangle$  and  $|\beta\alpha\rangle$  have different relative energies, and transitions between them allow thermal equilibration of the populations, whereas for the homonuclear case they do not. In other words, the dipolar Hamiltonian components  $\hat{A}^0$  are secular for the homonuclear case, and non-secular for the heteronuclear one. The matrix elements  $\sigma$  are not strictly spin-lattice relaxation rates, since they only represent the polarisation transfer rate between the two reservoirs  $I$  and  $S$ , as shown in figure 2.5.

Although  $J^m(\omega)$  is the spectral density function, it is not a measurable quantity, hence any relaxation rates measured as a function of frequency may later be referred to as ‘spectral density distributions’ or ‘spectral densities’.

## 2.3 Heteronuclear Relaxation Matrix

In this section the heteronuclear relaxation matrix elements will be derived for the single-crystal and isotropic powder average cases. In the case of a single crystal, every unit cell is aligned identically with the static field,  $B_0$ , the orientation of which will vary the strength of the dipolar coupling between nuclei. For a powder sample the microscopic grains are aligned randomly, creating some average dipolar interaction strength independent of the direction relative to  $B_0$ . The relaxation matrix is given by

$$\begin{bmatrix} \rho_I & \sigma_I \\ \sigma_S & \rho_S \end{bmatrix} = \begin{bmatrix} \rho_{II}^{IS} & \sigma_{IS}^{IS} \\ \sigma_{SI}^{IS} & \rho_{SS}^{IS} \end{bmatrix} + \begin{bmatrix} \rho_{II}^{II} & 0 \\ 0 & 0 \end{bmatrix}.$$

This consists of the heteronuclear and homonuclear contributions respectively, which can be expressed in terms of spectral density functions according to equations (2.36 - 2.40).

The spectral density functions  $J^m(\omega)$  are derived from the Fourier transform of the autocorrelation function. In this case the autocorrelation function is an ensemble average of products between the spatial components of the dipolar hamiltonian  $F$ , measured at two different times  $t$  and  $t + \tau$ . The Lorentzian function will be defined here as  $L(\omega) = \frac{\tau_c}{1+\omega^2\tau_c^2}$ .

$$\begin{aligned} J^m(\omega) &= \int_{-\infty}^{\infty} \langle F^{m*}(t)F^m(t + \tau) \rangle \exp(-i\omega\tau) d\tau \\ &= \frac{1}{2} \frac{4a}{(1+a)^2} \frac{\tau_c}{1+\omega^2\tau_c^2} [\langle F_L^{m*}F_L^m \rangle - \langle F_L^{m*}F_R^m \rangle - \langle F_R^{m*}F_L^m \rangle + \langle F_R^{m*}F_R^m \rangle] \\ &= \frac{1}{2} \frac{4a}{(1+a)^2} L(\omega) [\langle F_L^{m*}F_L^m \rangle - \langle F_L^{m*}F_R^m \rangle - \langle F_R^{m*}F_L^m \rangle + \langle F_R^{m*}F_R^m \rangle] \end{aligned} \tag{2.41}$$

### 2.3.1 Single-Crystal

Utilising equations (2.18d - 2.18f) it is possible to explicitly define the ensemble averages  $\langle F_A^{m*} F_B^m \rangle$ , for the zero-quantum, single-quantum and double-quantum transitions. These terms will depend on the crystal orientation relative to  $B_0$ . Refer to figure 2.3 for an illustration of the spherical polar coordinates used here.

For zero-quantum transitions, ( $m = 0$ ):

$$\begin{aligned}\langle F_L^{0*} F_L^0 \rangle &= r_L^{-6} (1 - 3 \cos^2 \theta_L) (1 - 3 \cos^2 \theta_L) \\ \langle F_L^{0*} F_R^0 \rangle &= \langle F_R^{0*} F_L^0 \rangle = r_L^{-3} r_R^{-3} (1 - 3 \cos^2 \theta_L) (1 - 3 \cos^2 \theta_R) \\ \langle F_R^{0*} F_R^0 \rangle &= r_R^{-6} (1 - 3 \cos^2 \theta_R) (1 - 3 \cos^2 \theta_R)\end{aligned}$$

For single-quantum transitions, ( $m = 1$ ):

$$\begin{aligned}\langle F_L^{1*} F_L^1 \rangle &= r_L^{-6} \sin \theta_L \cos \theta_L \exp(-i\phi_L) \sin \theta_L \cos \theta_L \exp(+i\phi_L) \\ &= r_L^{-6} \sin^2 \theta_L \cos^2 \theta_L \\ \langle F_L^{1*} F_R^1 \rangle &= r_L^{-3} r_R^{-3} \sin \theta_L \cos \theta_L \exp(-i\phi_L) \sin \theta_R \cos \theta_R \exp(+i\phi_R) \\ &= r_L^{-3} r_R^{-3} \sin \theta_L \cos \theta_L \sin \theta_R \cos \theta_R \exp(i(\phi_R - \phi_L)) \\ \langle F_R^{1*} F_L^1 \rangle &= r_R^{-3} r_L^{-3} \sin \theta_R \cos \theta_R \exp(-i\phi_R) \sin \theta_L \cos \theta_L \exp(+i\phi_L) \\ &= r_L^{-3} r_R^{-3} \sin \theta_L \cos \theta_L \sin \theta_R \cos \theta_R \exp(-i(\phi_R - \phi_L)) \\ \langle F_R^{1*} F_R^1 \rangle &= r_R^{-6} \sin \theta_R \cos \theta_R \exp(-i\phi_R) \sin \theta_R \cos \theta_R \exp(+i\phi_R) \\ &= r_R^{-6} \sin^2 \theta_R \cos^2 \theta_R\end{aligned}$$

For double-quantum transitions, ( $m = 2$ ):

$$\begin{aligned}\langle F_L^{2*} F_L^2 \rangle &= r_L^{-6} \sin^2 \theta_L \exp(-2i\phi_L) \sin^2 \theta_L \exp(+2i\phi_L) \\ &= r_L^{-6} \sin^4 \theta_L \\ \langle F_L^{2*} F_R^2 \rangle &= r_L^{-3} r_R^{-3} \sin^2 \theta_L \exp(-2i\phi_L) \sin^2 \theta_R \exp(+2i\phi_R) \\ &= r_L^{-3} r_R^{-3} \sin^2 \theta_L \sin^2 \theta_R \exp(2i(\phi_R - \phi_L)) \\ \langle F_R^{2*} F_L^2 \rangle &= r_R^{-3} r_L^{-3} \sin^2 \theta_R \exp(-2i\phi_R) \sin^2 \theta_L \exp(+2i\phi_L) \\ &= r_L^{-3} r_R^{-3} \sin^2 \theta_L \sin^2 \theta_R \exp(-2i(\phi_R - \phi_L)) \\ \langle F_R^{2*} F_R^2 \rangle &= r_R^{-6} \sin^2 \theta_R \exp(-2i\phi_R) \sin^2 \theta_R \exp(+2i\phi_R) \\ &= r_R^{-6} \sin^4 \theta_R\end{aligned}$$

If the angle between the two internuclear vectors is  $\alpha$ , as seen in figure 2.3, considering their dot product we may write  $\sin \theta_L \sin \theta_R \cos(\phi_L - \phi_R) = \cos \alpha - \cos \theta_L \cos \theta_R$ . Using the above equations and this identity, the spectral density functions (2.41) can be fully expressed as follows:

$$\begin{aligned}
 J^0(\omega) &= \frac{1}{2} \frac{4a}{(1+a)^2} L(\omega) \begin{bmatrix} r_L^{-6}(1-3\cos^2\theta_L)(1-3\cos^2\theta_L) \\ -2r_L^{-3}r_R^{-3}(1-3\cos^2\theta_L)(1-3\cos^2\theta_R) \\ +r_R^{-6}(1-3\cos^2\theta_R)(1-3\cos^2\theta_R) \end{bmatrix} \\
 &= \frac{1}{2} \frac{4a}{(1+a)^2} L(\omega) [r_L^{-3}(1-3\cos^2\theta_L) + r_R^{-3}(1-3\cos^2\theta_R)]^2 \\
 J^1(\omega) &= \frac{1}{2} \frac{4a}{(1+a)^2} L(\omega) \begin{bmatrix} r_L^{-6}\sin^2\theta_L\cos^2\theta_L \\ -r_L^{-3}r_R^{-3}\sin\theta_L\cos\theta_L\sin\theta_R\cos\theta_R\exp(i(\phi_R-\phi_L)) \\ -r_L^{-3}r_R^{-3}\sin\theta_L\cos\theta_L\sin\theta_R\cos\theta_R\exp(-i(\phi_R-\phi_L)) \\ +r_R^{-6}\sin^2\theta_R\cos^2\theta_R \end{bmatrix} \\
 &= \frac{1}{2} \frac{4a}{(1+a)^2} L(\omega) \begin{bmatrix} r_L^{-6}\sin^2\theta_L\cos^2\theta_L + r_R^{-6}\sin^2\theta_R\cos^2\theta_R \\ -2r_L^{-3}r_R^{-3}\sin\theta_L\cos\theta_L\sin\theta_R\cos\theta_R\cos(\phi_R-\phi_L) \end{bmatrix} \\
 &= \frac{1}{2} \frac{4a}{(1+a)^2} L(\omega) \begin{bmatrix} r_L^{-6}\sin^2\theta_L\cos^2\theta_L + r_R^{-6}\sin^2\theta_R\cos^2\theta_R \\ -2r_L^{-3}r_R^{-3}\cos\theta_L\cos\theta_R(\cos\alpha - \cos\theta_L\cos\theta_R) \end{bmatrix} \\
 J^2(\omega) &= \frac{1}{2} \frac{4a}{(1+a)^2} L(\omega) \begin{bmatrix} r_L^{-6}\sin^4\theta_L \\ -r_L^{-3}r_R^{-3}\sin^2\theta_L\sin^2\theta_R\exp(2i(\phi_R-\phi_L)) \\ -r_L^{-3}r_R^{-3}\sin^2\theta_L\sin^2\theta_R\exp(-2i(\phi_R-\phi_L)) \\ +r_R^{-6}\sin^4\theta_R \end{bmatrix} \\
 &= \frac{1}{2} \frac{4a}{(1+a)^2} L(\omega) \begin{bmatrix} r_L^{-6}\sin^4\theta_L + r_R^{-6}\sin^4\theta_R \\ -2r_L^{-3}r_R^{-3}\sin^2\theta_L\sin^2\theta_R\cos(2(\phi_R-\phi_L)) \end{bmatrix} \\
 &= \frac{1}{2} \frac{4a}{(1+a)^2} L(\omega) \begin{bmatrix} r_L^{-6}\sin^4\theta_L + r_R^{-6}\sin^4\theta_R \\ -2r_L^{-3}r_R^{-3}\sin^2\theta_L\sin^2\theta_R(2\cos^2(\phi_R-\phi_L)-1) \end{bmatrix} \\
 &= \frac{1}{2} \frac{4a}{(1+a)^2} L(\omega) \begin{bmatrix} r_L^{-6}\sin^4\theta_L + r_R^{-6}\sin^4\theta_R \\ -4r_L^{-3}r_R^{-3}\sin^2\theta_L\sin^2\theta_R\cos^2(\phi_R-\phi_L) \\ +2r_L^{-3}r_R^{-3}\sin^2\theta_L\sin^2\theta_R \end{bmatrix} \\
 &= \frac{1}{2} \frac{4a}{(1+a)^2} L(\omega) \begin{bmatrix} r_L^{-6}\sin^4\theta_L + r_R^{-6}\sin^4\theta_R \\ -4r_L^{-3}r_R^{-3}(\cos\alpha - \cos\theta_L\cos\theta_R)^2 \\ +2r_L^{-3}r_R^{-3}\sin^2\theta_L\sin^2\theta_R \end{bmatrix}
 \end{aligned}$$

These spectral density functions can now be substituted in the relaxation matrix elements:

$$\begin{aligned}
 \rho_{II}^{IS} &= \frac{\gamma_I^2 \gamma_S^2 \hbar^2 S(S+1)}{24N_I} \left( \frac{\mu_0}{4\pi} \right)^2 \frac{4a}{(1+a)^2} \\
 &\times \begin{bmatrix} L(\omega_I - \omega_S) [r_L^{-3}(1 - 3 \cos^2 \theta_L) + r_R^{-3}(1 - 3 \cos^2 \theta_R)]^2 \\ + 18L(\omega_I) \begin{bmatrix} r_L^{-6} \sin^2 \theta_L \cos^2 \theta_L + r_R^{-6} \sin^2 \theta_R \cos^2 \theta_R \\ - 2r_L^{-3}r_R^{-3} \cos \theta_L \cos \theta_R (\cos \alpha - \cos \theta_L \cos \theta_R) \end{bmatrix} \\ + 9L(\omega_I + \omega_S) \begin{bmatrix} r_L^{-6} \sin^4 \theta_L + r_R^{-6} \sin^4 \theta_R \\ - 4r_L^{-3}r_R^{-3} (\cos \alpha - \cos \theta_L \cos \theta_R)^2 \\ + 2r_L^{-3}r_R^{-3} \sin^2 \theta_L \sin^2 \theta_R \end{bmatrix} \end{bmatrix} \\
 \sigma_{IS}^{IS} &= \frac{\gamma_I^2 \gamma_S^2 \hbar^2 I(I+1)}{24} \left( \frac{\mu_0}{4\pi} \right)^2 \frac{4a}{(1+a)^2} \\
 &\times \begin{bmatrix} -L(\omega_I - \omega_S) [r_L^{-3}(1 - 3 \cos^2 \theta_L) + r_R^{-3}(1 - 3 \cos^2 \theta_R)]^2 \\ + 9L(\omega_I + \omega_S) \begin{bmatrix} r_L^{-6} \sin^4 \theta_L + r_R^{-6} \sin^4 \theta_R \\ - 4r_L^{-3}r_R^{-3} (\cos \alpha - \cos \theta_L \cos \theta_R)^2 \\ + 2r_L^{-3}r_R^{-3} \sin^2 \theta_L \sin^2 \theta_R \end{bmatrix} \end{bmatrix} \\
 \sigma_{SI}^{IS} &= \frac{\gamma_I^2 \gamma_S^2 \hbar^2 S(S+1)}{24} \left( \frac{\mu_0}{4\pi} \right)^2 \frac{4a}{(1+a)^2} \\
 &\times \begin{bmatrix} -L(\omega_S - \omega_I) [r_L^{-3}(1 - 3 \cos^2 \theta_L) + r_R^{-3}(1 - 3 \cos^2 \theta_R)]^2 \\ + 9L(\omega_S + \omega_I) \begin{bmatrix} r_L^{-6} \sin^4 \theta_L + r_R^{-6} \sin^4 \theta_R \\ - 4r_L^{-3}r_R^{-3} (\cos \alpha - \cos \theta_L \cos \theta_R)^2 \\ + 2r_L^{-3}r_R^{-3} \sin^2 \theta_L \sin^2 \theta_R \end{bmatrix} \end{bmatrix} \\
 \rho_{SS}^{IS} &= \frac{\gamma_I^2 \gamma_S^2 \hbar^2 I(I+1)}{24N_S} \left( \frac{\mu_0}{4\pi} \right)^2 \frac{4a}{(1+a)^2} \\
 &\times \begin{bmatrix} L(\omega_S - \omega_I) [r_L^{-3}(1 - 3 \cos^2 \theta_L) + r_R^{-3}(1 - 3 \cos^2 \theta_R)]^2 \\ + 18L(\omega_S) \begin{bmatrix} r_L^{-6} \sin^2 \theta_L \cos^2 \theta_L + r_R^{-6} \sin^2 \theta_R \cos^2 \theta_R \\ - 2r_L^{-3}r_R^{-3} \cos \theta_L \cos \theta_R (\cos \alpha - \cos \theta_L \cos \theta_R) \end{bmatrix} \\ + 9L(\omega_S + \omega_I) \begin{bmatrix} r_L^{-6} \sin^4 \theta_L + r_R^{-6} \sin^4 \theta_R \\ - 4r_L^{-3}r_R^{-3} (\cos \alpha - \cos \theta_L \cos \theta_R)^2 \\ + 2r_L^{-3}r_R^{-3} \sin^2 \theta_L \sin^2 \theta_R \end{bmatrix} \end{bmatrix}
 \end{aligned}$$

$$\rho_{II}^{II} = \frac{3\gamma_I^4 \hbar^2 I(I+1)}{2N_I} \left( \frac{\mu_0}{4\pi} \right)^2 \frac{4a}{(1+a)^2} \\ \times \begin{bmatrix} L(\omega_I) \begin{bmatrix} r_L^{-6} \sin^2 \theta_L \cos^2 \theta_L + r_R^{-6} \sin^2 \theta_R \cos^2 \theta_R \\ -2r_L^{-3} r_R^{-3} \cos \theta_L \cos \theta_R (\cos \alpha - \cos \theta_L \cos \theta_R) \end{bmatrix} \\ + L(2\omega_I) \begin{bmatrix} r_L^{-6} \sin^4 \theta_L + r_R^{-6} \sin^4 \theta_R \\ -4r_L^{-3} r_R^{-3} (\cos \alpha - \cos \theta_L \cos \theta_R)^2 \\ +2r_L^{-3} r_R^{-3} \sin^2 \theta_L \sin^2 \theta_R \end{bmatrix} \end{bmatrix}$$

These relaxation matrix elements can be generalised for any number of protons  $j$  in motion between sites  $L$  and  $R$ , interacting with stationary homonuclei  $i$ , and heteronuclei  $k$ .

$$\rho_{II}^{IS} = \frac{\gamma_I^2 \gamma_S^2 \hbar^2 S(S+1)}{24N_I} \left( \frac{\mu_0}{4\pi} \right)^2 \frac{4a}{(1+a)^2} \\ \times \begin{bmatrix} L(\omega_I - \omega_S) \sum_{k,j} \left[ r_{kjL}^{-3} (1 - 3 \cos^2 \theta_{kjL}) + r_{kjR}^{-3} (1 - 3 \cos^2 \theta_{kjR}) \right]^2 \\ + 18L(\omega_I) \sum_{k,j} \begin{bmatrix} r_{kjL}^{-6} \sin^2 \theta_{kjL} \cos^2 \theta_{kjL} + r_{kjR}^{-6} \sin^2 \theta_{kjR} \cos^2 \theta_{kjR} \\ -2r_{kjL}^{-3} r_{kjR}^{-3} \cos \theta_{kjL} \cos \theta_{kjR} (\cos \alpha - \cos \theta_{kjL} \cos \theta_{kjR}) \end{bmatrix} \\ + 9L(\omega_I + \omega_S) \sum_{k,j} \begin{bmatrix} r_{kjL}^{-6} \sin^4 \theta_{kjL} + r_{kjR}^{-6} \sin^4 \theta_{kjR} \\ -4r_{kjL}^{-3} r_{kjR}^{-3} (\cos \alpha - \cos \theta_{kjL} \cos \theta_{kjR})^2 \\ +2r_{kjL}^{-3} r_{kjR}^{-3} \sin^2 \theta_{kjL} \sin^2 \theta_{kjR} \end{bmatrix} \end{bmatrix}$$

$$\sigma_{IS}^{IS} = \frac{\gamma_I^2 \gamma_S^2 \hbar^2 I(I+1)}{24} \left( \frac{\mu_0}{4\pi} \right)^2 \frac{4a}{(1+a)^2} \\ \times \begin{bmatrix} -L(\omega_I - \omega_S) \sum_{k,j} \left[ r_{kjL}^{-3} (1 - 3 \cos^2 \theta_{kjL}) + r_{kjR}^{-3} (1 - 3 \cos^2 \theta_{kjR}) \right]^2 \\ + 9L(\omega_I + \omega_S) \sum_{k,j} \begin{bmatrix} r_{kjL}^{-6} \sin^4 \theta_{kjL} + r_{kjR}^{-6} \sin^4 \theta_{kjR} \\ -4r_{kjL}^{-3} r_{kjR}^{-3} (\cos \alpha - \cos \theta_{kjL} \cos \theta_{kjR})^2 \\ +2r_{kjL}^{-3} r_{kjR}^{-3} \sin^2 \theta_{kjL} \sin^2 \theta_{kjR} \end{bmatrix} \end{bmatrix}$$

$$\sigma_{SI}^{IS} = \frac{\gamma_I^2 \gamma_S^2 \hbar^2 S(S+1)}{24} \left( \frac{\mu_0}{4\pi} \right)^2 \frac{4a}{(1+a)^2} \\ \times \begin{bmatrix} -L(\omega_S - \omega_I) \sum_{k,j} \left[ r_{kjL}^{-3} (1 - 3 \cos^2 \theta_{kjL}) + r_{kjR}^{-3} (1 - 3 \cos^2 \theta_{kjR}) \right]^2 \\ + 9L(\omega_S + \omega_I) \sum_{k,j} \begin{bmatrix} r_{kjL}^{-6} \sin^4 \theta_{kjL} + r_{kjR}^{-6} \sin^4 \theta_{kjR} \\ -4r_{kjL}^{-3} r_{kjR}^{-3} (\cos \alpha - \cos \theta_{kjL} \cos \theta_{kjR})^2 \\ +2r_{kjL}^{-3} r_{kjR}^{-3} \sin^2 \theta_{kjL} \sin^2 \theta_{kjR} \end{bmatrix} \end{bmatrix}$$

$$\begin{aligned} \rho_{SS}^{IS} &= \frac{\gamma_I^2 \gamma_S^2 \hbar^2 I(I+1)}{24N_S} \left( \frac{\mu_0}{4\pi} \right)^2 \frac{4a}{(1+a)^2} \\ &\times \left[ \begin{array}{l} L(\omega_S - \omega_I) \sum_{k,j} \left[ r_{kjL}^{-3} (1 - 3 \cos^2 \theta_{kjL}) + r_{kjR}^{-3} (1 - 3 \cos^2 \theta_{kjR}) \right]^2 \\ + 18L(\omega_S) \sum_{k,j} \left[ \begin{array}{l} r_{kjL}^{-6} \sin^2 \theta_{kjL} \cos^2 \theta_{kjL} + r_{kjR}^{-6} \sin^2 \theta_{kjR} \cos^2 \theta_{kjR} \\ - 2r_{kjL}^{-3} r_{kjR}^{-3} \cos \theta_{kjL} \cos \theta_{kjR} (\cos \alpha - \cos \theta_{kjL} \cos \theta_{kjR}) \end{array} \right] \\ + 9L(\omega_S + \omega_I) \sum_{k,j} \left[ \begin{array}{l} r_{kjL}^{-6} \sin^4 \theta_{kjL} + r_{kjR}^{-6} \sin^4 \theta_{kjR} \\ - 4r_{kjL}^{-3} r_{kjR}^{-3} (\cos \alpha - \cos \theta_{kjL} \cos \theta_{kjR})^2 \\ + 2r_{kjL}^{-3} r_{kjR}^{-3} \sin^2 \theta_{kjL} \sin^2 \theta_{kjR} \end{array} \right] \end{array} \right] \\ \rho_{II}^{II} &= \frac{3\gamma_I^4 \hbar^2 I(I+1)}{2N_I} \left( \frac{\mu_0}{4\pi} \right)^2 \frac{4a}{(1+a)^2} \\ &\times \left[ \begin{array}{l} L(\omega_I) \sum_{i,j} \left[ \begin{array}{l} r_{ijL}^{-6} \sin^2 \theta_{ijL} \cos^2 \theta_{ijL} + r_{ijR}^{-6} \sin^2 \theta_{ijR} \cos^2 \theta_{ijR} \\ - 2r_{ijL}^{-3} r_{ijR}^{-3} \cos \theta_{ijL} \cos \theta_{ijR} (\cos \alpha - \cos \theta_{ijL} \cos \theta_{ijR}) \end{array} \right] \\ + L(2\omega_I) \sum_{i,j} \left[ \begin{array}{l} r_{ijL}^{-6} \sin^4 \theta_{ijL} + r_{ijR}^{-6} \sin^4 \theta_{ijR} \\ - 4r_{ijL}^{-3} r_{ijR}^{-3} (\cos \alpha - \cos \theta_{ijL} \cos \theta_{ijR})^2 \\ + 2r_{ijL}^{-3} r_{ijR}^{-3} \sin^2 \theta_{ijL} \sin^2 \theta_{ijR} \end{array} \right] \end{array} \right] \end{aligned}$$

Identifying the common factors, these relaxation matrix equations can be simplified further:

$$\begin{aligned} \rho_{II}^{IS} &= \frac{\gamma_I^2 \gamma_S^2 \hbar^2 S(S+1)}{24N_I} \left( \frac{\mu_0}{4\pi} \right)^2 \frac{4a}{(1+a)^2} \\ &\times [L(\omega_I - \omega_S)G_{Het}^0 + 18L(\omega_I)G_{Het}^1 + 9L(\omega_I + \omega_S)G_{Het}^2] \end{aligned} \quad (2.42)$$

$$\begin{aligned} \sigma_{IS}^{IS} &= \frac{\gamma_I^2 \gamma_S^2 \hbar^2 I(I+1)}{24} \left( \frac{\mu_0}{4\pi} \right)^2 \frac{4a}{(1+a)^2} \\ &\times [-L(\omega_I - \omega_S)G_{Het}^0 + 9L(\omega_I + \omega_S)G_{Het}^2] \end{aligned} \quad (2.43)$$

$$\begin{aligned} \sigma_{SI}^{IS} &= \frac{\gamma_I^2 \gamma_S^2 \hbar^2 S(S+1)}{24} \left( \frac{\mu_0}{4\pi} \right)^2 \frac{4a}{(1+a)^2} \\ &\times [-L(\omega_S - \omega_I)G_{Het}^0 + 9L(\omega_S + \omega_I)G_{Het}^2] \end{aligned} \quad (2.44)$$

$$\begin{aligned} \rho_{SS}^{IS} &= \frac{\gamma_I^2 \gamma_S^2 \hbar^2 I(I+1)}{24N_S} \left( \frac{\mu_0}{4\pi} \right)^2 \frac{4a}{(1+a)^2} \\ &\times [L(\omega_S - \omega_I)G_{Het}^0 + 18L(\omega_S)G_{Het}^1 + 9L(\omega_S + \omega_I)G_{Het}^2] \end{aligned} \quad (2.45)$$

$$\rho_{II}^{II} = \frac{3\gamma_I^4 \hbar^2 I(I+1)}{2N_I} \left( \frac{\mu_0}{4\pi} \right)^2 \frac{4a}{(1+a)^2} [L(\omega_I)G_{Homo}^1 + L(2\omega_I)G_{Homo}^2] \quad (2.46)$$

The homonuclear and heteronuclear dipolar coupling strengths  $G$  are then given by the following:

$$G_{H\text{et}}^0 = \sum_{k,j} \left[ r_{kjL}^{-3} (1 - 3 \cos^2 \theta_{kjL}) + r_{kjR}^{-3} (1 - 3 \cos^2 \theta_{kjR}) \right]^2 \quad (2.47)$$

$$G_{H\text{et}}^1 = \sum_{k,j} \left[ \begin{array}{l} r_{kjL}^{-6} \sin^2 \theta_{kjL} \cos^2 \theta_{kjL} + r_{kjR}^{-6} \sin^2 \theta_{kjR} \cos^2 \theta_{kjR} \\ -2r_{kjL}^{-3} r_{kjR}^{-3} \cos \theta_{kjL} \cos \theta_{kjR} (\cos \alpha - \cos \theta_{kjL} \cos \theta_{kjR}) \end{array} \right] \quad (2.48)$$

$$G_{H\text{et}}^2 = \sum_{k,j} \left[ \begin{array}{l} r_{kjL}^{-6} \sin^4 \theta_{kjL} + r_{kjR}^{-6} \sin^4 \theta_{kjR} + 2r_{kjL}^{-3} r_{kjR}^{-3} \sin^2 \theta_{kjL} \sin^2 \theta_{kjR} \\ -4r_{kjL}^{-3} r_{kjR}^{-3} (\cos \alpha - \cos \theta_{kjL} \cos \theta_{kjR})^2 \end{array} \right] \quad (2.49)$$

$$G_{Homo}^1 = \sum_{i,j} \left[ \begin{array}{l} r_{ijL}^{-6} \sin^2 \theta_{ijL} \cos^2 \theta_{ijL} + r_{ijR}^{-6} \sin^2 \theta_{ijR} \cos^2 \theta_{ijR} \\ -2r_{ijL}^{-3} r_{ijR}^{-3} \cos \theta_{ijL} \cos \theta_{ijR} (\cos \alpha - \cos \theta_{ijL} \cos \theta_{ijR}) \end{array} \right] \quad (2.50)$$

$$G_{Homo}^2 = \sum_{i,j} \left[ \begin{array}{l} r_{ijL}^{-6} \sin^4 \theta_{ijL} + r_{ijR}^{-6} \sin^4 \theta_{ijR} + 2r_{ijL}^{-3} r_{ijR}^{-3} \sin^2 \theta_{ijL} \sin^2 \theta_{ijR} \\ -4r_{ijL}^{-3} r_{ijR}^{-3} (\cos \alpha - \cos \theta_{ijL} \cos \theta_{ijR})^2 \end{array} \right] \quad (2.51)$$

### 2.3.2 Isotropic Powder

A similar analysis can now be performed for the isotropic powder case, for which the ensemble average dipolar spatial components have no orientation dependence, and are given by [12]:

For zero-quantum transitions, ( $m = 0$ ):

$$\begin{aligned}\langle F_L^{0*} F_L^0 \rangle &= \frac{4}{5} r_L^{-6} \\ \langle F_L^{0*} F_R^0 \rangle &= \langle F_R^{0*} F_L^0 \rangle = \frac{4}{10} r_L^{-3} r_R^{-3} (3 \cos^2 \alpha - 1) \\ \langle F_R^{0*} F_R^0 \rangle &= \frac{4}{5} r_R^{-6}\end{aligned}$$

For single-quantum transitions, ( $m = 1$ ):

$$\begin{aligned}\langle F_L^{1*} F_L^1 \rangle &= \frac{2}{15} r_L^{-6} \\ \langle F_L^{1*} F_R^1 \rangle &= \langle F_R^{1*} F_L^1 \rangle = \frac{2}{30} r_L^{-3} r_R^{-3} (3 \cos^2 \alpha - 1) \\ \langle F_R^{1*} F_R^1 \rangle &= \frac{2}{15} r_R^{-6}\end{aligned}$$

For double-quantum transitions, ( $m = 2$ ):

$$\begin{aligned}\langle F_L^{2*} F_L^2 \rangle &= \frac{8}{15} r_L^{-6} \\ \langle F_L^{2*} F_R^2 \rangle &= \langle F_R^{2*} F_L^2 \rangle = \frac{8}{30} r_L^{-3} r_R^{-3} (3 \cos^2 \alpha - 1) \\ \langle F_R^{2*} F_R^2 \rangle &= \frac{8}{15} r_R^{-6}\end{aligned}$$

The powder average spectral density functions can then be expressed as follows:

$$J^0(\omega) = \frac{4}{10} \frac{4a}{(1+a)^2} L(\omega) [r_L^{-6} - r_L^{-3} r_R^{-3} (3 \cos^2 \alpha - 1) + r_R^{-6}]$$

$$J^1(\omega) = \frac{2}{30} \frac{4a}{(1+a)^2} L(\omega) [r_L^{-6} - r_L^{-3} r_R^{-3} (3 \cos^2 \alpha - 1) + r_R^{-6}]$$

$$J^2(\omega) = \frac{8}{30} \frac{4a}{(1+a)^2} L(\omega) [r_L^{-6} - r_L^{-3} r_R^{-3} (3 \cos^2 \alpha - 1) + r_R^{-6}]$$

The relaxation matrix elements can now be expressed in terms of these spectral density functions. As in the previous subsection, they can also be generalised for numerous mobile protons  $j$ , coupled to stationary homonuclei  $i$  and heteronuclei  $k$ .

$$\begin{aligned} \rho_{II}^{IS} &= \frac{\gamma_I^2 \gamma_S^2 \hbar^2 S(S+1)}{30N_I} \left(\frac{\mu_0}{4\pi}\right)^2 \frac{4a}{(1+a)^2} \sum_{k,j} \left[ r_{kjL}^{-6} - r_{kjL}^{-3} r_{kjR}^{-3} (3 \cos^2 \alpha - 1) + r_{kjR}^{-6} \right] \\ &\quad \times [L(\omega_I - \omega_S) + 3L(\omega_I) + 6L(\omega_I + \omega_S)] \\ \sigma_{IS}^{IS} &= \frac{\gamma_I^2 \gamma_S^2 \hbar^2 I(I+1)}{30} \left(\frac{\mu_0}{4\pi}\right)^2 \frac{4a}{(1+a)^2} \sum_{k,j} \left[ r_{kjL}^{-6} - r_{kjL}^{-3} r_{kjR}^{-3} (3 \cos^2 \alpha - 1) + r_{kjR}^{-6} \right] \\ &\quad \times [-L(\omega_I - \omega_S) + 6L(\omega_I + \omega_S)] \\ \sigma_{SI}^{IS} &= \frac{\gamma_I^2 \gamma_S^2 \hbar^2 S(S+1)}{30} \left(\frac{\mu_0}{4\pi}\right)^2 \frac{4a}{(1+a)^2} \sum_{k,j} \left[ r_{kjL}^{-6} - r_{kjL}^{-3} r_{kjR}^{-3} (3 \cos^2 \alpha - 1) + r_{kjR}^{-6} \right] \\ &\quad \times [-L(\omega_S - \omega_I) + 6L(\omega_S + \omega_I)] \\ \rho_{SS}^{IS} &= \frac{\gamma_I^2 \gamma_S^2 \hbar^2 I(I+1)}{30N_S} \left(\frac{\mu_0}{4\pi}\right)^2 \frac{4a}{(1+a)^2} \sum_{k,j} \left[ r_{kjL}^{-6} - r_{kjL}^{-3} r_{kjR}^{-3} (3 \cos^2 \alpha - 1) + r_{kjR}^{-6} \right] \\ &\quad \times [L(\omega_S - \omega_I) + 3L(\omega_S) + 6L(\omega_S + \omega_I)] \\ \rho_{II}^{II} &= \frac{\gamma_I^4 \hbar^2 I(I+1)}{5N_I} \left(\frac{\mu_0}{4\pi}\right)^2 \frac{4a}{(1+a)^2} \sum_{i,j} \left[ r_{ijL}^{-6} - r_{ijL}^{-3} r_{ijR}^{-3} (3 \cos^2 \alpha - 1) + r_{ijR}^{-6} \right] \\ &\quad \times [L(\omega_I) + 4L(2\omega_I)] \end{aligned}$$

The dipolar interaction strength sums are common factors, and the above equations can be reduced to the following commonly recognised form:

$$\rho_{II}^{IS} = \frac{\gamma_I^2 \gamma_S^2 \hbar^2 S(S+1)}{30N_I} \left( \frac{\mu_0}{4\pi} \right)^2 \frac{4a}{(1+a)^2} G_{Het}^{Pow} [L(\omega_I - \omega_S) + 3L(\omega_I) + 6L(\omega_I + \omega_S)] \quad (2.52)$$

$$\sigma_{IS}^{IS} = \frac{\gamma_I^2 \gamma_S^2 \hbar^2 I(I+1)}{30} \left( \frac{\mu_0}{4\pi} \right)^2 \frac{4a}{(1+a)^2} G_{Het}^{Pow} [-L(\omega_I - \omega_S) + 6L(\omega_I + \omega_S)] \quad (2.53)$$

$$\sigma_{SI}^{IS} = \frac{\gamma_I^2 \gamma_S^2 \hbar^2 S(S+1)}{30} \left( \frac{\mu_0}{4\pi} \right)^2 \frac{4a}{(1+a)^2} G_{Het}^{Pow} [-L(\omega_S - \omega_I) + 6L(\omega_S + \omega_I)] \quad (2.54)$$

$$\rho_{SS}^{IS} = \frac{\gamma_I^2 \gamma_S^2 \hbar^2 I(I+1)}{30N_S} \left( \frac{\mu_0}{4\pi} \right)^2 \frac{4a}{(1+a)^2} G_{Het}^{Pow} [L(\omega_S - \omega_I) + 3L(\omega_S) + 6L(\omega_S + \omega_I)] \quad (2.55)$$

$$\rho_{II}^{II} = \frac{\gamma_I^4 \hbar^2 I(I+1)}{5N_I} \left( \frac{\mu_0}{4\pi} \right)^2 \frac{4a}{(1+a)^2} G_{Homo}^{Pow} [L(\omega_I) + 4L(2\omega_I)] \quad (2.56)$$

The dipolar interaction lattice sums  $G$  are then given by:

$$G_{Het}^{Pow} = \sum_{k,j} \left[ r_{kjL}^{-6} - r_{kjL}^{-3} r_{kjR}^{-3} (3 \cos^2 \alpha - 1) + r_{kjR}^{-6} \right] \quad (2.57)$$

$$G_{Homo}^{Pow} = \sum_{i,j} \left[ r_{ijL}^{-6} - r_{ijL}^{-3} r_{ijR}^{-3} (3 \cos^2 \alpha - 1) + r_{ijR}^{-6} \right] \quad (2.58)$$

When working with purely homonuclear spin systems, equations (2.56) and (2.58) are usually combined

$$\frac{1}{T_1} = C_{II} \frac{4a}{(1+a)^2} [L(\omega_I) + 4L(2\omega_I)], \quad (2.59)$$

where the dipolar coupling constant  $C_{II}$  is given by

$$C_{II} = \frac{\gamma_I^4 \hbar^2 I(I+1)}{5N_I} \left( \frac{\mu_0}{4\pi} \right)^2 \sum_{k,j} \left[ r_{kjL}^{-6} - r_{kjL}^{-3} r_{kjR}^{-3} (3 \cos^2 \alpha - 1) + r_{kjR}^{-6} \right] \quad (2.60)$$

To demonstrate graphically the general behaviour of spin-lattice relaxation as a function of frequency, equation (2.59) will be taken here as an example. For

a constant temperature, figure 2.6 shows how the different-width Lorentzians  $L(\omega)$  and  $L(2\omega)$  combine to give the overall form of equation (2.59).

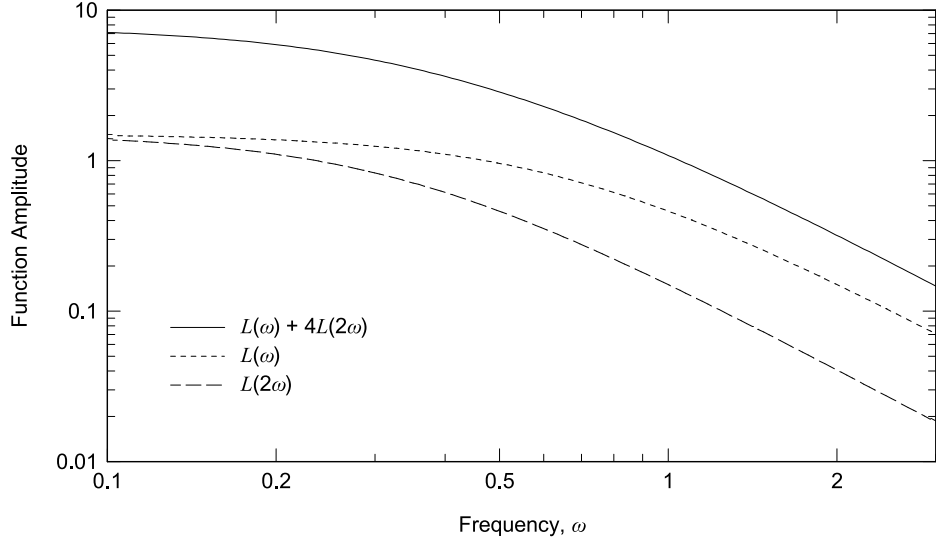


Figure 2.6: Combination of Lorentzian functions  $L(\omega)$  and  $L(2\omega)$  as in equation (2.59).

Increasing the temperature generally has the effect of also increasing the proton transfer rate,  $\tau_c^{-1}$ . This change tends to broaden the Lorentzian lineshape, as demonstrated in figure 2.7. For simplicity, the temperature-dependent amplitude factor  $\frac{4a}{(1+a)^2}$  has been kept constant in this illustration.

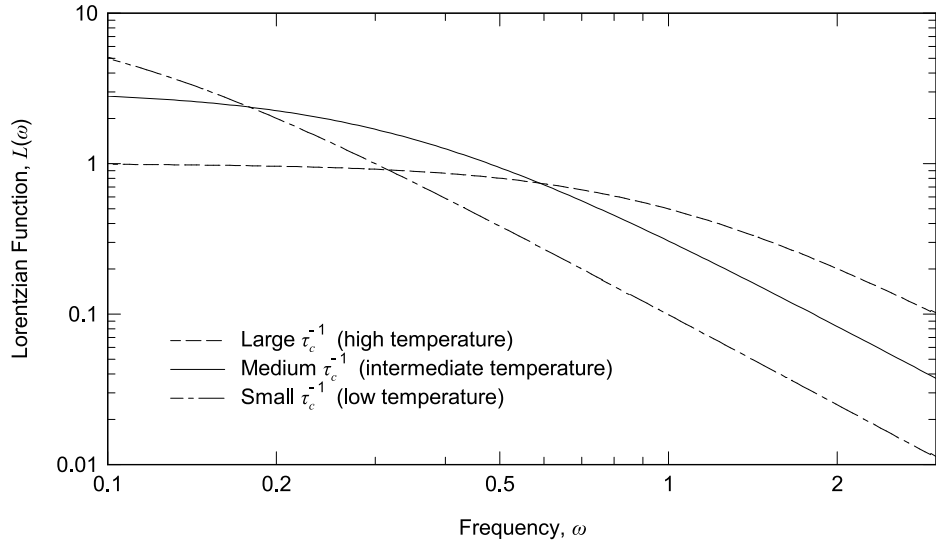


Figure 2.7: Dependence of the Lorentzian function  $L(\omega)$  on the correlation rate  $\tau_c^{-1}$ .

## 2.4 Carboxylic Acid Dimers

Carboxylic acid molecules often form dimers when in the solid state, which provides a good environment for proton transfer to occur across the connecting hydrogen bonds. This thesis focuses on the study of benzoic acid and its derivatives as described in chapter 1. A wider overview of hydrogen bond tunnelling can be found elsewhere [13], with the majority of discussions therein being applicable to carboxylic acid dimers.

Hydrogen bonds can form when a hydrogen atom shares a covalent bond with a strongly electronegative atom such as oxygen, nitrogen, or fluorine. This induces a partial positive charge on the hydrogen, which then can form a weak dipolar attraction to a lone pair of electrons on a heteroatom, creating the hydrogen bond. In benzoic acid, two bridging hydrogen bonds form between two carboxyl groups of neighbouring benzoic acid molecules to form the dimer.

The protons involved in the hydrogen bond can undergo motion from the nearest electronegative oxygen to the other it shares the bond with. This interchange produces the two tautomeric forms of benzoic acid as shown in figure 2.8. From measurement of the dipolar interactions in a similar system [14] the proton transfer is known to occur simultaneously across both hydrogen bonds in the dimer rather than a stepwise process, hence it is referred to as ‘concerted proton transfer’.

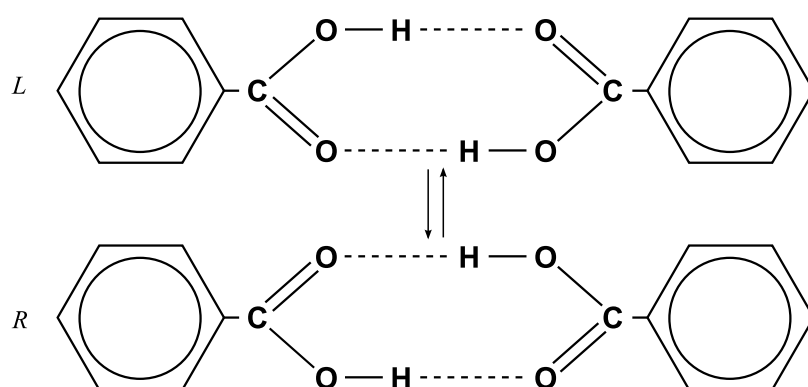


Figure 2.8: The two tautomeric configurations of a benzoic acid dimer labelled *L* and *R*.

For an isolated benzoic acid dimer the two tautomers have equivalent energy. However, in the solid state the crystal unit cell is monoclinic [15], which introduces an asymmetry to the electrostatic environments of the two tautomers. For this reason the asymmetric double-minimum potential model

is applicable to benzoic acid, with the two tautomers being labelled *L* and *R* to represent the low and high energy configurations.

As discussed in section 2.2 the DMP is a one-dimensional representation of the proton transfer PES, which is formed from a combination of intermolecular and intramolecular vibrational modes coupled to this process. The temperature-dependence of these contributions is represented by the entropy term in equation (2.13). For the case of benzoic acid, the change in entropy,  $\Delta S$ , is found experimentally to be approximately zero, such that the DMP asymmetry is independent of temperature,

$$\Delta G \approx \Delta H. \quad (2.61)$$

The dynamics of proton transfer in benzoic acid as a function of temperature have been studied and observed to undergo a smooth transition from a thermally-activated high-temperature regime to quantum tunnelling at low temperatures [8]. The correlation rate,  $\tau_c^{-1}$ , of the motion can be modelled as a combination of an Arrhenius type law and two terms derived from the quantum mechanical description of transitions between the ground states and the first excited states of the DMP [10, 16]. Despite modelling only a limited number of transitions of those possible, this formulation appears sufficient at all temperatures relevant to this study,  $4.2K \lesssim T \lesssim 300K$ .

$$\tau_c^{-1} = k_0 \coth\left(\frac{\Delta H}{2k_B T}\right) + \tau_{exc}^{-1} \exp\left(\frac{-\Delta E_{exc}}{k_B T}\right) + \tau_{act}^{-1} \exp\left(\frac{-\Delta E_{act}}{k_B T}\right) \quad (2.62)$$

The constants  $\tau_{exc}^{-1}$  and  $\tau_{act}^{-1}$  are correlation rates from the relevant modes at infinite temperature, whereas  $k_0$  is the zero-temperature tunnelling rate limit.

## 2.5 The Methyl Rotor Model

Although not being directly relevant to the topic of this thesis, it is important to quantify here the relaxation behaviour caused by the presence of a methyl group for interpreting the results presented in chapter 7. Beyond the summary presented here, a very good overview of methyl group dynamics studied by NMR can be found elsewhere [17].

At room temperature and below only the ground vibrational eigenstate is occupied, hence it can be considered as a rigid rotor. The methyl group as a whole experiences some form of potential energy restriction, created by inter-molecular and intra-molecular interactions, that hinders its rotation. Due to the tetrahedral arrangement of the methyl hydrogen nuclei, such rotations are hindered by a three-fold symmetric sinusoidal PES before regaining the original orientation. Each PES well then has a series of librational excitation states which the methyl group can occupy.

At low temperatures the rotation can occur via coherent quantum tunnelling between the three PES minima, resulting in a tunnelling splitting of each librational eigenstate into *A* and *E* states. The dipole-dipole interaction is able to induce changes between these tunnelling states of the rotor, as well as between the Zeeman eigenstates. Consideration of the transition probabilities involved in this energy manifold leads to the following formulation of the spin-lattice relaxation rate for a powder sample [18].

$$\frac{1}{T_1} = C_{AE} \sum_{n=1}^2 \left( \frac{n^2 \tau_c}{1 + (\omega_t + n\omega_L)^2 \tau_c^2} + \frac{n^2 \tau_c}{1 + (\omega_t - n\omega_L)^2 \tau_c^2} \right) + C_{EE} \sum_{n=1}^2 \frac{n^2 \tau_c^2}{1 + n^2 \omega_L^2 \tau_c^2} \quad (2.63)$$

The first term here represents relaxation due to conversion between the two tunnelling states *A* and *E*, hence it depends on the tunnelling frequency  $\omega_t$ . The tunnelling frequency for each excited librational state is different, and tends to decrease with energy. Hence, as higher energy states become populated, the observed tunnelling frequency becomes a temperature-dependent average of those frequencies [19]. The second term in this equation is very similar to equation (2.59), the homonuclear relaxation of two hydrogen nuclei, resulting from the allowed Zeeman transitions in the energy manifold. The quantities  $C_{AE}$  and  $C_{EE}$  are dipolar relaxation strength constants, similar to those derived

in section 2.3, that depend strongly on the proximity of other protons and can be determined experimentally. For ease of identification, the two terms terms of equation (2.63) will be referred to as the ‘Haupt’ and ‘BPP’ terms respectively.

The temperature dependence of the methyl rotor correlation rate can be described phenomenologically in terms of Arrhenius type laws for low, high, and intermediate temperature ranges [20].

$$\tau_c^{-1} = \tau_L^{-1} \exp\left(\frac{-E_L}{k_B T}\right) + \tau_I^{-1} \exp\left(\frac{-E_I}{k_B T}\right) + \tau_H^{-1} \exp\left(\frac{-E_H}{k_B T}\right) \quad (2.64)$$

This formulation works well at all temperatures relevant to the work in this thesis, with the parameters being determined experimentally. Apart from the activation energy  $E_L$ , which is usually found to be equivalent to the first librational excitation energy of the potential well, these parameters have no explicit physical counterparts but represent the averages of such quantities. It is worth noting here that due to the presence of coherent tunnelling, there is no zero-temperature minimum correlation rate equivalent to  $k_0$  for the asymmetric DMP. This will become important when considering the relaxation contributions from both types of motion in chapter 7.

## Chapter 3

# Experimental Details

In this chapter the experimental apparatus, data acquisition and processing methods used will be described in detail. All of the work presented in this thesis was conducted on the superconducting field-cycling spectrometer at the University of Nottingham quantum molecular dynamics laboratory. In terms of its specifications, this spectrometer was designed to study the NMR of solid samples, with no magic-angle spinning. As explained in chapter 1, such conditions resulted in a broad Lorentzian lineshape due to dipolar interactions, and the time-dependent measurement of its amplitude was used to extract the spin-lattice relaxation rate.

### 3.1 Field-Cycling NMR

A field-cycling spectrometer is characterised by the ability to periodically and significantly vary its longitudinal magnetic field strength,  $B_0$ , on a timescale short compared to the spin-lattice relaxation times studied [21, 22]. This is usually achieved by either rapidly moving the sample between regions of different field strength via mechanical methods, or keeping the sample stationary and changing the external field by varying the current through the solenoid.

The main benefits of field-cycling over fixed-field spectrometers is their ability to affect spins with different magnetogyric ratios without the need for multi-channel spectrometers with electronics tuned to multiple frequencies. Also, the preparation, recovery and detection of the spins can occur at different fields, allowing the frequency dependence of the relaxation rates to be studied, a feature that was used extensively during this investigation.

### 3.1.1 Field-Cycling Magnet

Once a superconducting magnet is cooled below its critical temperature, a current is established in the solenoid to induce the magnetic field. For a normal persistent-mode magnet the driving power supply is then isolated from the solenoid to avoid Ohmic loss along the power supply leads, after which the field should remain constant indefinitely. The University of Nottingham field-cycling spectrometer was designed with a Niobium-Tin superconducting solenoid that is connected to the magnet power supply at all times. This allows the field to be constantly varied, such that the instantaneous current supplied by the power supply is proportional to the induced field. While the current and temperature are maintained the magnet has an infinite duty cycle, allowing it to be used for studying both short and long recovery times.

As mentioned earlier, one of the requirements of a field-cycling system is to be able to change the field on a short timescale. Following the laws of electromagnetic induction, a compromise had to be made between the maximum field strength and field ramp rate. This resulted in a solenoid capable of  $10 \text{ Ts}^{-1}$  ramping rate, with a peak operating field of 2.5 T at a current of 150 A. During operation, a voltage of up to  $\pm 15 \text{ V}$  is applied across the power leads to ramp the current through the solenoid. Once the desired current is achieved the ramp voltage is switched off, apart from a few millivolts to account for the resistance in the supply leads.

Due to physical limitations of power supply, it was impossible to produce perfect field switching profiles. The resulting overshoot amplitude and duration depended on the circuit parameters, and required a settle period as the field stabilised at the set value. Generally speaking, the settle period duration increased with the difference between switching fields and ramp rate as shown in figure 3.1. Following extensive testing [23], it was found that the best balance between field switch time and settle period was at  $5 \text{ Ts}^{-1}$  for switching to the resonance field prior to acquisition, and  $8 \text{ Ts}^{-1}$  for all others. Further calibration of the resonance field prior to acquisition is discussed in section 3.3.

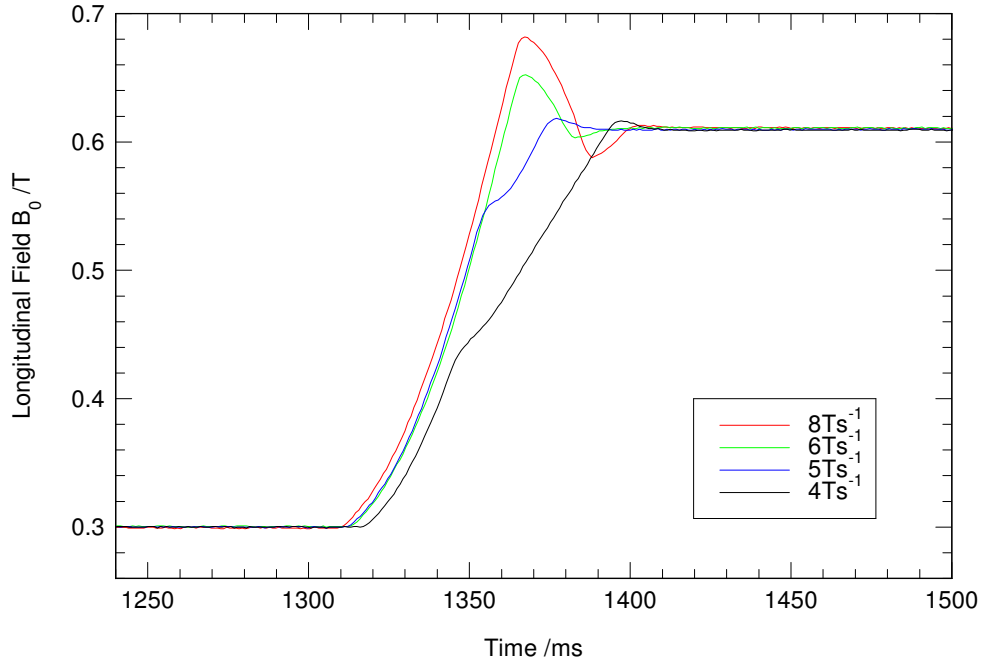


Figure 3.1: Longitudinal field switching profiles for different switching rates. Data adapted from [23].

### 3.1.2 Cryostat and Variable Temperature Insert

The superconducting solenoid is fixed at the bottom of the variable temperature insert (VTI), which in turn is located inside the cryostat. The cryostat functions as an insulating barrier between the VTI and the environment, and as a supply of liquid helium-4 (LHe). From the outside-in, it consists of an evacuated area, followed by a liquid nitrogen-14 ( $\text{LN}_2$ ) reservoir connected to a copper heat shield. Within the heat shield, but separated by another vacuum space, is the LHe reservoir in which the VTI sits, as shown in figure 3.2.

The VTI is a housing for the superconducting solenoid and probe. The lower half of the VTI, with the solenoid, is immersed in the cryostat LHe reservoir, whilst the probe bore within is protected from cryogenic temperatures with another vacuum. A capillary tube, with an externally-operated needle valve, provides a supply of LHe to the probe bore, via a heat exchanger. Varying the helium flow through the capillary and a probe-mounted heater allowed the sample temperature to be controlled in the range 4.2 K – 300 K, and maintained to within  $\pm 1\%$  once stable. The cryostat, VTI, superconducting solenoid and power supply were made by CRYOGENIC Ltd.

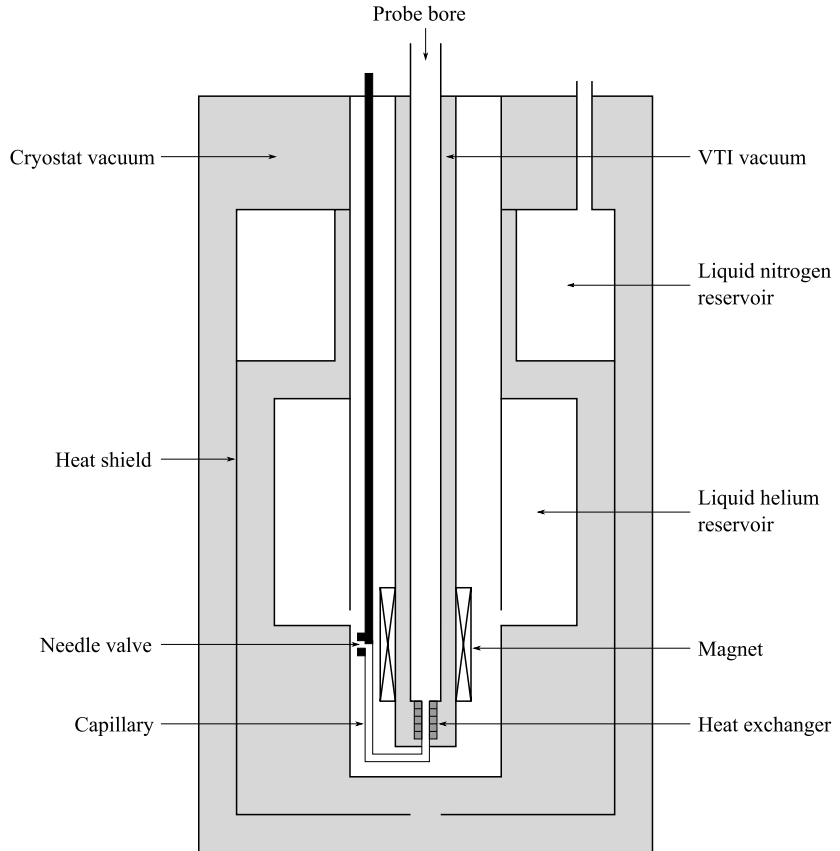


Figure 3.2: A schematic diagram of the field-cycling spectrometer cryostat and VTI assembly. Vacuum spaces are shaded in grey.

### 3.1.3 Probes

Three home-built probes were used to collect the results presented in this thesis, each one tuned to different resonant frequency and suited for studying a particular nuclear species. The probes tuned to be resonant at 36.8 MHz and 38.64 MHz were used for studying hydrogen, whilst the 21.9 MHz probe was used for carbon-13 measurements.

The probe head structure consisted of a radio frequency (RF) coil made from copper wire wound around a Kel-F former, mounted in a solid brass block. The LC circuit tuning capacitor and Cernox calibrated resistance thermometer were also mounted nearby, as shown in figure 3.3. A resistive heating element made from copper-nickel wire was wound around the base of the brass block to control the temperature of the sample. Both the thermometer and heater were connected to a Lake Shore 311 temperature controller.

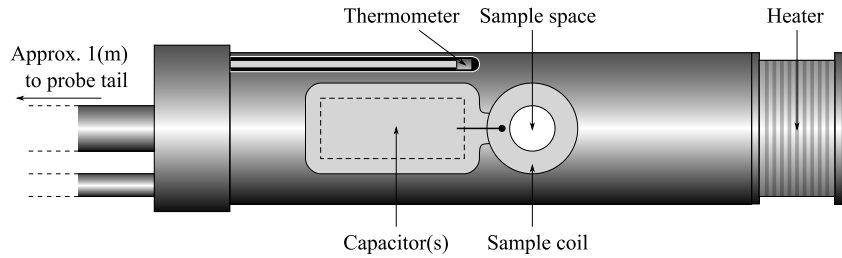


Figure 3.3: A schematic diagram of the probe head structure.

For these probes the NMR LC circuit design consisted of a solenoid, which was used for both excitation and detection of the sample spins, mounted in series with a tuning capacitor to establish a resonant circuit. Since pulsed NMR is an inherently narrowband technique, the quality factor of the probe LC circuit was an important consideration in their design. A high quality factor indicates that the LC circuit Lorentzian frequency response has an increased sensitivity at the resonant frequency with a narrow bandwidth, whereas a smaller quality factor indicates increased bandwidth at the expense of sensitivity.

For optimal power transfer from the LC circuit at the probe head, along the metre-long solid triaxial transmission line, to the duplexer at the probe tail both ends should be matched to the same impedance, in this case  $50\ \Omega$ . To achieve this matching condition at the probe head a variable tuning capacitor can be connected in parallel with the LC circuit. Although this design increased the quality factor of the circuit [24], placing the tuning capacitor at the probe head, where it would be subject to large temperature changes, made it difficult to tune due to the temperature-dependence of the components. Alternatively, the impedance matching can be done at room temperature just prior to the duplexer at the probe tail, reducing the quality factor and increasing its stability. The first approach was adopted for the 21.9 MHz probe, where the weak  $^{13}\text{C}$  signal benefited from a high quality factor, whilst not suffering much field fluctuation at the resonance field, 2.042 T. Resonant field stability was more important for the 36.8 MHz and 38.64 MHz probes, which employed the latter design, with the lower quality factor producing a wider frequency response curve with less variation near resonance, whilst relying on the abundance of hydrogen in most samples to offset the signal loss.

### 3.1.4 Spectrometer

A heterodyne spectrometer design is necessary to work with probes tuned to different frequencies. For optimal efficiency, all the spectrometer components should be tuned to a particular carrier (intermediate) frequency,  $\nu_I$ . The heterodyning technique converts the Larmor frequency,  $\nu_L$ , signal of the probe to  $\nu_I$  through a series of mixing steps as shown in figure 3.4. The particular spectrometer used in this case was a Tecmag Apollo console.

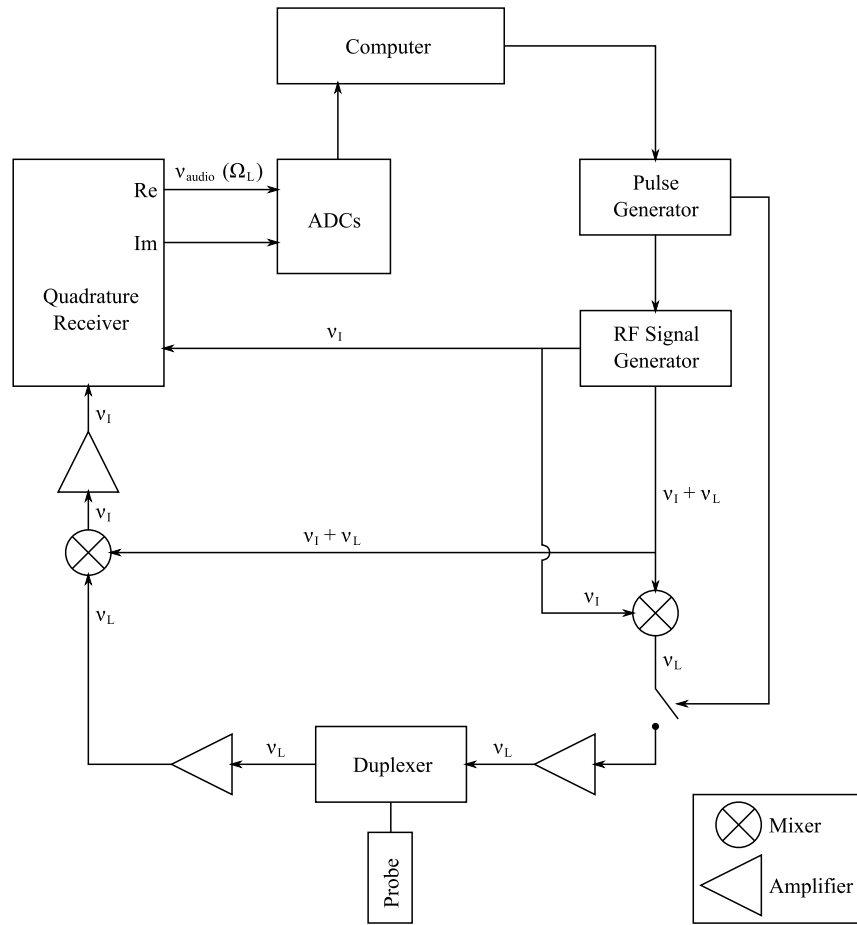


Figure 3.4: The heterodyne spectrometer design with a carrier frequency  $\nu_I$ .

## 3.2 Data Processing

The acquired FID data were processed using a combination of the spectrometer software and in-house Visual Basic code. After an exponential apodization function was applied to the FID, with the exponent determined by  $T_2$ , it was Fourier transformed and phased to separate the real part of the signal into the absorption component. An integral of the real signal was then taken as a measure of the recovered longitudinal polarisation. This reduced the measured noise compared with an integral of the magnitude signal because the absorption peak has a larger central intensity with noise from only one channel.

Due to physical limitations of the magnet power supply, the field during FID acquisition was offset from resonance by a few gauss, the exact value depending on the particularities of each experiment. To account for the signal drop when slightly off-resonance, the integral amplitude was adjusted according to a calibration curve. This calibration curve was the normalised frequency response of the probe, which is a product of the Lorentzian probe quality factor and the sinc function frequency profile of the measurement pulse. The calibration curve was determined empirically by measuring the recovered polarisation for a fixed time after saturation as a function of measurement field.

The majority of data analysis, such as curve fitting of the magnetisation recovery curves to extract relaxation rates, was performed using the EasyPlot software. MATLAB was then utilised for more complex analysis and modelling of the data.

### 3.2.1 Fitting Equations

The particular function used to interpret the magnetisation recovery data and extract meaningful parameters such as the spin-lattice relaxation time depended on the sample studied and on the pulse sequence used. The data from any of the pulse sequences employed during this investigation could be interpreted by one of the following equations.

Consider first a homonuclear sample where the magnetisation recovery and relaxation occur at the same  $B_0$  field, similar to a static-field saturation recovery experiment (subsection 3.3.1). Some relaxation will occur between saturation and measurement during the necessary settle times, in addition to that happening during the recovery time  $\tau_R$ . Letting the sum of such additional relaxation times be  $D$ , the magnetisation recovery can be described by adapting

equation (2.23) as follows:

$$\begin{aligned}
 M_z &= M_0 \left( 1 - \exp \left( \frac{-(D+t)}{T_1} \right) \right) \\
 &= M_0 \left( 1 - \exp \left( \frac{-D}{T_1} \right) \exp \left( \frac{-t}{T_1} \right) \right) \\
 &= M_0 \left( 1 - \exp \left( \frac{-D}{T_1} \right) + \exp \left( \frac{-D}{T_1} \right) - \exp \left( \frac{-D}{T_1} \right) \exp \left( \frac{-t}{T_1} \right) \right) \\
 &= M_0 \left( 1 - \exp \left( \frac{-D}{T_1} \right) \right) + M_0 \exp \left( \frac{-D}{T_1} \right) \left( 1 - \exp \left( \frac{-t}{T_1} \right) \right) \\
 &= M_0 \left( 1 - \exp \left( \frac{-D}{T_1} \right) \right) + M_0 \left( 1 - 1 + \exp \left( \frac{-D}{T_1} \right) \right) \left( 1 - \exp \left( \frac{-t}{T_1} \right) \right) \\
 &= M_0 \left( 1 - \exp \left( \frac{-D}{T_1} \right) \right) + \left[ M_0 - M_0 \left( 1 - \exp \left( \frac{-D}{T_1} \right) \right) \right] \left( 1 - \exp \left( \frac{-t}{T_1} \right) \right)
 \end{aligned} \tag{3.1}$$

At a fixed  $B_0$  field the time  $D$  will be equivalent between repetitions of a pulse sequence, meaning the relaxation occurring during that time can be considered constant for an experiment. Equation (3.1) can then be expressed as

$$M_z = [M_0 - b] \left( 1 - \exp \left( \frac{-t}{T_1} \right) \right) + b, \tag{3.2}$$

where the additional relaxation  $b = M_0(1 - \exp(-D/T_1))$  is observed as a constant baseline offset. If the constant-field constraint is now lifted, then the additional relaxation will include field-switching times at a variety of relaxation rates. This will result in a different offset  $b$  depending on the recovery field, but it will remain constant for each set of pulse sequences at a given recovery field, maintaining the validity of equation (3.2).

Results from homonuclear saturation recovery experiments can be interpreted using equation (3.2). Occasionally the magnetisation recovery of a heteronuclear sample will appear single-exponential, under the conditions described in subsection 2.2.3, in which case this equation will also be applicable. In other cases, where multiple relaxation components can be clearly identified, the following equation would be used. Applying the same arguments as above regarding additional relaxation to equations (2.26) we get

$$M_z = [M_0 - b](1 + c_1 \exp(-R_1 t) + c_2 \exp(-R_2 t)) + b. \tag{3.3}$$

The homonuclear polarisation recovery experiment (subsection 3.3.3) data can be modelled by an equation similar to (2.23),

$$M_z = [M_{pol} - M_0] \exp\left(\frac{-t}{T_1}\right) + M_0, \quad (3.4)$$

where the magnetisation begins at a large polarised value  $M_{pol}$  and relaxes towards thermal equilibrium. Since an accurate measurement of  $M_{pol}$  is not necessary as long as  $M_{pol} \gg M_0$ , the offset from additional relaxation is usually incorporated in the polarised magnetisation value  $M_{pol} = M_{pol}^{actual} - b$ .

Through trial and error it was found that the EasyPlot nonlinear least squares curve fitting algorithm tended to systematically underestimate the spin-lattice relaxation rate by c.a. 10% when the magnetisation dynamic range was small. This error could be mitigated by acquiring more data for that experiment, or employing the polarisation recovery pulse sequence (subsection 3.3.3) for homonuclear samples.

### 3.3 Pulse Sequences

The individual pulse sequences and field-switching profiles as shown by the figures in this section were written in the spectrometer software. The in-house Visual Basic code was then used to interface with the spectrometer software and automate measurements by supplying the parameters for each repetition of the pulse sequence and storing the data afterwards. To clarify further discussions, each instance of a pulse sequence, with a particular recovery time, will be called a ‘run’. A series of implemented pulse sequences, with logarithmically increasing recovery times, will then be referred to as an ‘experiment’. The recovery times were incremented logarithmically as opposed to linearly in time to provide better data sampling distribution for an exponential recovery. Also, for a multi-exponential magnetisation recovery curve, a linear increment distribution would be biased towards components with longer relaxation times. In most cases the range of  $\tau_R$  went from  $T_1/1000$  to  $20T_1$  to provide a good measure of the relaxation rate.

The aforementioned fluctuation of the  $B_0$  field immediately after a field gradient required a few hundred milliseconds to fully stabilise to within  $\pm 3$  G. This delay was unacceptable prior to the measurement pulse because the NMR signal would decay in that time. The greatest deviation could be avoided by reducing the delay to 40 ms, but this then required a measurement field offset to account for the remaining difference. This offset depended predictably on the field prior to the switch and the time spent at that field, which in all the experiments below was the recovery field and recovery time. A systematic study was performed to measure the required offset across the full range of recovery fields and recovery times, and coded into the Visual Basic script. These measurement field offsets together with the frequency response calibration curve discussed in section 3.2 were sufficient to make reliable and reproducible measurements of the magnetisation.

All the different pulse sequences used in the course of this investigation, and their application are described in the subsections below.

### 3.3.1 Static-Field Homonuclear Saturation Recovery Pulse Sequence

This pulse sequence was used for samples with a single non-spin-zero species, or for heteronuclear samples with zero cross-relaxation rate,  $\sigma$ , to measure the spin-lattice relaxation time,  $T_1$ , at the probe resonance field. This approach negated inaccuracies due to field fluctuations of the field-cycling method.

- (a) The longitudinal magnetic field,  $B_0$ , is pre-set to match the primary species',  $I$ , resonance of the probe. The primary spins are saturated with a train of  $12 \pi/2$  radio frequency (RF) pulses so as to recreate identical polarisation conditions,  $\langle I_z \rangle_{t=0} = 0$ .
- (b) The sample magnetisation is allowed to recover for a time  $\tau_R$ . The recovery time,  $\tau_R$ , is incremented logarithmically after each run. For convenience, the beginning of this section is set to be at time  $t = 0$ .
- (c) The primary species' magnetisation is then measured with a single  $\pi/2$  RF pulse.

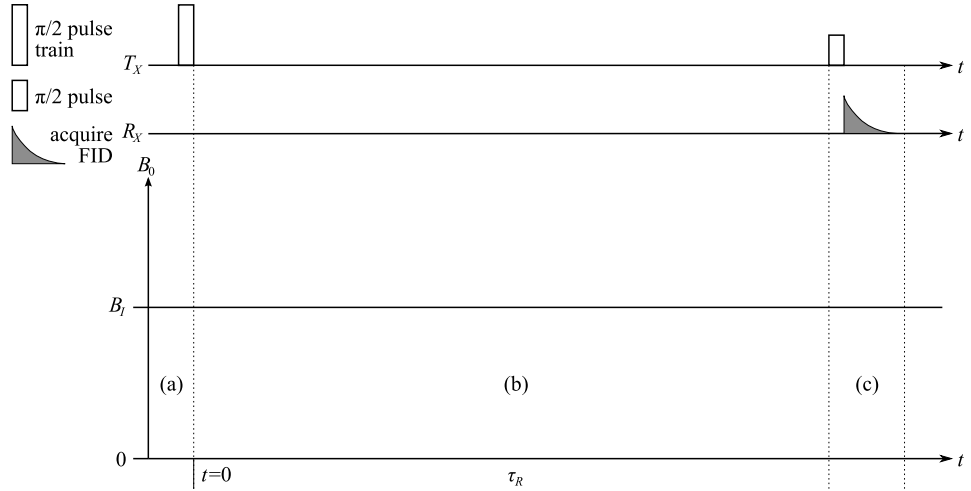


Figure 3.5: The static-field homonuclear saturation recovery pulse sequence. Schematic: the axes are not to scale.

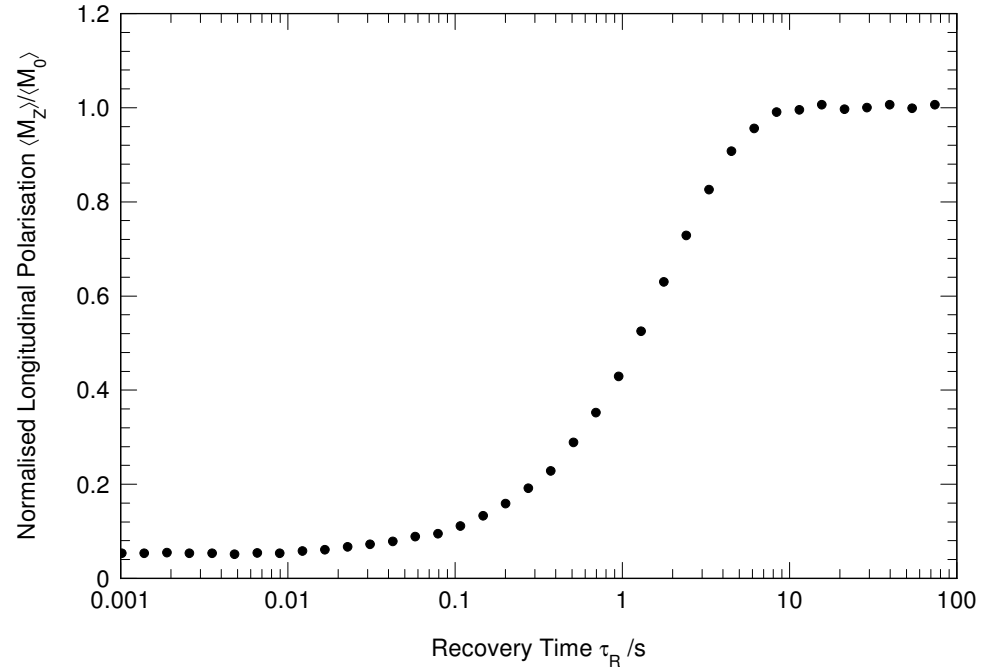


Figure 3.6: Sample saturation recovery experiment data.

Figure 3.6 shows a typical example of data from a saturation recovery experiment. The polarisation is observed to increase from near-zero towards thermal equilibrium with increasing recovery time,  $\tau_R$ , the experimental variable during each experiment. The non-zero starting polarisation, due to relaxation occurring during necessary delays, is accounted for by a constant parameter during fitting as described in subsection 3.2.1.

### 3.3.2 Homonuclear Saturation Recovery Pulse Sequence

This pulse sequence was used for samples with a single non-spin-zero species, or for heteronuclear samples with zero cross-relaxation rate,  $\sigma$ , to measure the spin-lattice relaxation time,  $T_1$ , as a function of field.

- (a) The longitudinal magnetic field,  $B_0$ , is raised to match the primary species',  $I$ , resonance of the probe at a rate of  $\Delta_1 = 8 \text{ Ts}^{-1}$ . The primary spins are saturated with a train of  $12 \pi/2$  radio frequency (RF) pulses so as to recreate identical polarisation conditions,  $\langle I_z \rangle_{t=0} = 0$ .
- (b) The sample magnetisation is allowed to recover at a field  $B_R$ , for a time  $\tau_R$ . The recovery time,  $\tau_R$ , is incremented logarithmically after each run. For convenience, the beginning of this section is set to be at time  $t = 0$ .
- (c) The field is then switched back to  $B_I$ , at a rate of  $\Delta_2 = 5 \text{ Ts}^{-1}$  for increased field stability, and the magnetisation is measured with a single  $\pi/2$  RF pulse.

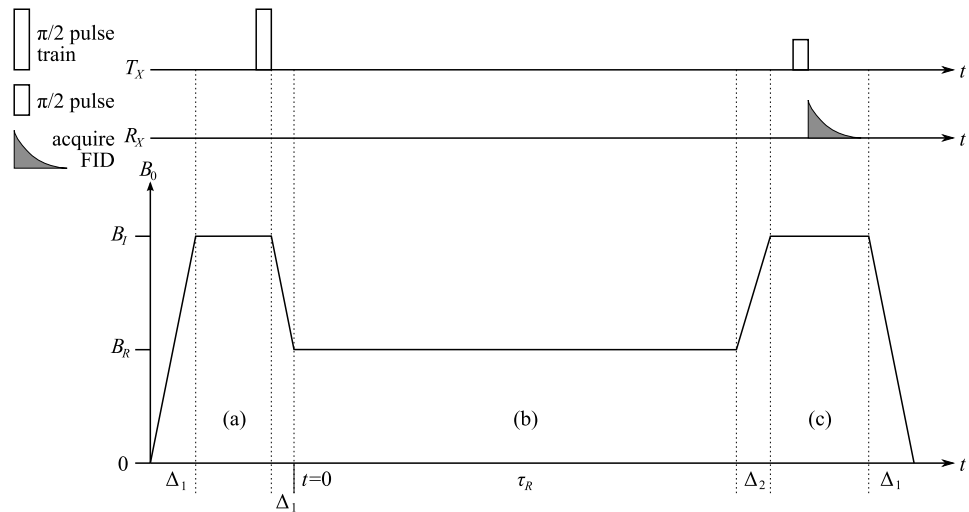


Figure 3.7: The homonuclear saturation recovery pulse sequence. Schematic: the axes are not to scale.

### 3.3.3 Homonuclear Polarisation Recovery Pulse Sequence

When the dynamic range of the NMR signal recorded with the homonuclear saturation recovery pulse sequence was insufficient, due to low  $B_R$  or high temperature, this pulse sequence was used to measure the field-dependent  $T_1$  in samples with a single non-spin-zero species.

- (a) The longitudinal magnetic field,  $B_0$ , is raised to match the primary species',  $I$ , resonance of the probe at a rate of  $\Delta_1 = 8 \text{ Ts}^{-1}$ . To recreate identical polarisation conditions at the beginning of each run the primary spins are first saturated with a train of 12  $\pi/2$  radio frequency pulses.
- (b) The spins are polarised at a field  $B_{pol}$  for a time  $\tau_{pol}$ . In all cases  $B_{pol} > B_R$  so that there is sufficient dynamic range between the polarised magnetisation measurement and thermal equilibrium magnetisation at  $B_R$ . The polarisation time  $\tau_{pol}$  is set to achieve 65%-85% polarisation at  $B_{pol}$ , and is kept constant throughout an ‘experiment’.
- (c) The sample magnetisation is allowed to recover at a field  $B_R$ , for a time  $\tau_R$ . The recovery time,  $\tau_R$ , is incremented logarithmically after each run. For convenience, the beginning of this section is set to be at time  $t = 0$ .
- (d) The field is then switched back to  $B_I$ , at a rate of  $\Delta_2 = 5 \text{ Ts}^{-1}$  for increased field stability, and the magnetisation is measured with a single  $\pi/2$  RF pulse.

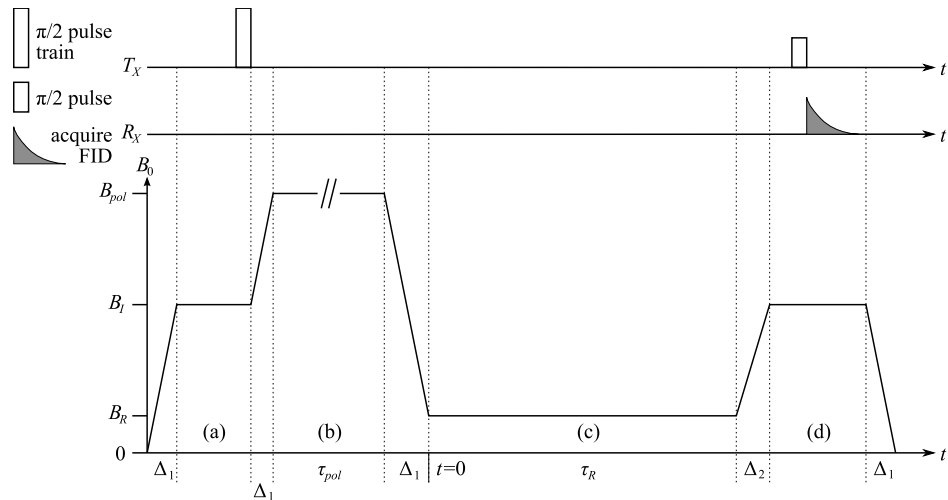


Figure 3.8: The homonuclear polarisation recovery pulse sequence. Schematic: the axes are not to scale.

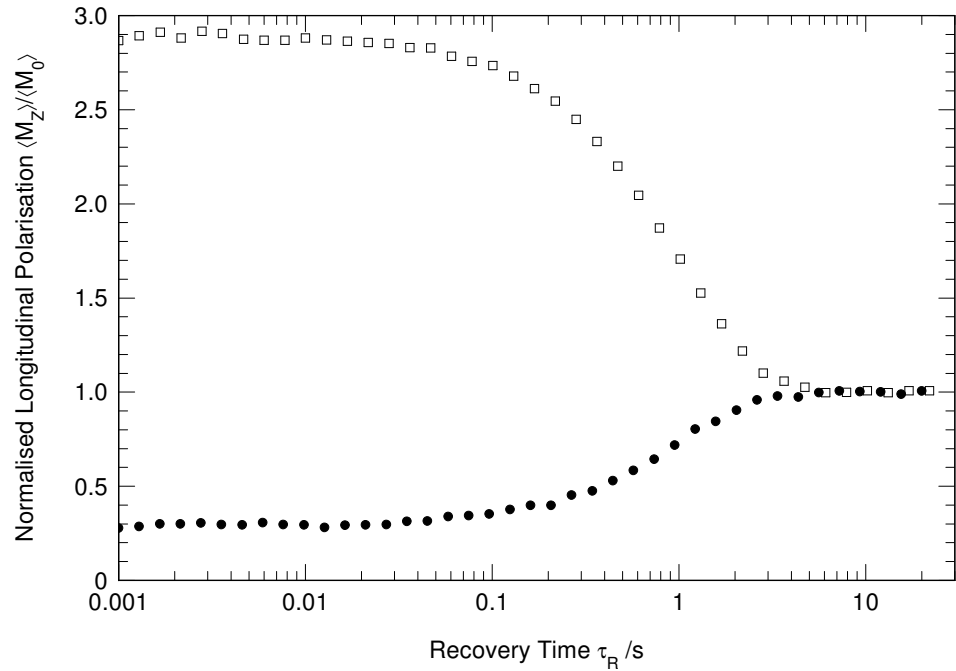


Figure 3.9: Sample polarisation recovery data (open squares) in comparison with saturation recovery data (filled circles) at the same recovery field and temperature.

Figure 3.9 shows how the data from a polarisation recovery experiment has a greater dynamic range compared to that from a saturation recovery experiment, allowing a the relaxation rate to be measured more accurately. The polarisation recovers at the same rate and towards the same thermal equilibrium for both types of experiment, differing only in their initial polarisation conditions. This pulse sequence was not used for heteronuclear samples because the initial polarisation conditions of the secondary spin species are not well known.

### 3.3.4 Heteronuclear Saturation Recovery Pulse Sequence

This pulse sequence was used for samples with two non-spin-zero species and non-zero cross-relaxation rate,  $\sigma$ , to measure the spin-lattice relaxation rates  $R_1$  and  $R_2$  as a function of field.

- (a) The  $B_0$  field is raised to match the secondary species',  $S$ , resonance of the probe at a rate of  $\Delta_1 = 8 \text{ Ts}^{-1}$ , where the secondary spins are saturated with a train of 12  $\pi/2$  RF pulses.
- (b) Then the primary species',  $I$ , spins are saturated, at their probe resonance field, with 12  $\pi/2$  RF pulses. This stage is shortened as much as possible to minimise the recovery of secondary spin magnetisation during this time, and preserve the initial polarisation conditions,  $\langle I_z \rangle_{t=0} = 0$   $\langle S_z \rangle_{t=0} = 0$ .
- (c) The sample magnetisation is allowed to recover at a field  $B_R$ , for a time  $\tau_R$ . The recovery time,  $\tau_R$ , is incremented logarithmically after each run. For convenience, the beginning of this section is set to be at time  $t = 0$ .
- (d) The field is then switched back to  $B_I$ , at a rate of  $\Delta_2 = 5 \text{ Ts}^{-1}$  for increased field stability, and the magnetisation is measured with a single  $\pi/2$  RF pulse.

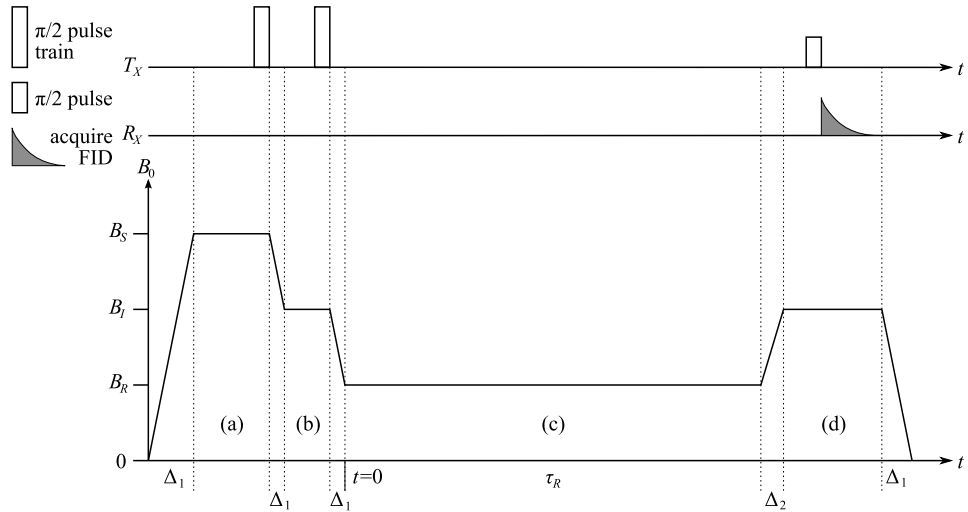


Figure 3.10: The heteronuclear saturation recovery pulse sequence. Schematic: the axes are not to scale.

### 3.3.5 Zero-Field Heteronuclear Saturation Recovery Pulse Sequence

For samples with two non-spin-zero species, non-zero cross-relaxation rate,  $\sigma$ , and a secondary species' resonance field,  $B_S$ , beyond that achievable by the hardware, this pulse sequence was used to measure the field-dependence of the spin-lattice relaxation rates  $R_1$  and  $R_2$ .

- (a) The sample is allowed to rest at zero field for a time,  $\tau_{prep}$ , which is sufficiently long for the secondary species' spins to come to thermal equilibrium, losing all polarisation and effectively becoming saturated.
- (b) Then the longitudinal magnetic field,  $B_0$ , is raised to match the primary species',  $I$ , resonance of the probe at a rate of  $\Delta_1 = 8 \text{ Ts}^{-1}$ . The primary spins are saturated with a train of  $12 \pi/2$  radio frequency (RF) pulses so as to ensure identical polarisation conditions,  $\langle I_z \rangle_{t=0} = 0 \quad \langle S_z \rangle_{t=0} = 0$ .
- (c) The sample magnetisation is allowed to recover at a field  $B_R$ , for a time  $\tau_R$ . The recovery time,  $\tau_R$ , is incremented logarithmically after each run. For convenience, the beginning of this section is set to be at time  $t = 0$ .
- (d) The field is then switched back to  $B_I$ , at a rate of  $\Delta_2 = 5 \text{ Ts}^{-1}$  for increased field stability, and the magnetisation is measured with a single  $\pi/2$  RF pulse.

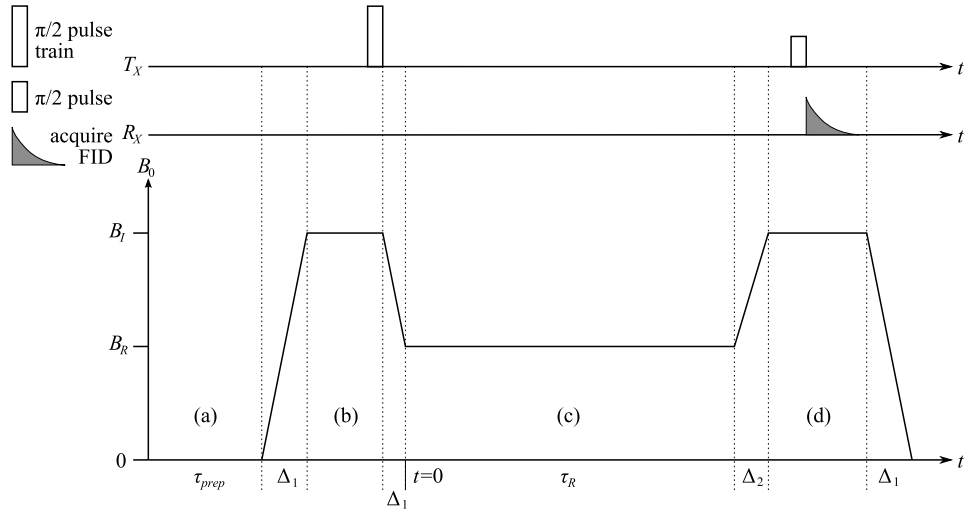


Figure 3.11: The zero-field heteronuclear saturation recovery pulse sequence. Schematic: the axes are not to scale.

### 3.3.6 Cross-Relaxation Pulse Sequence

This pulse sequence was used to measure the cross-relaxation rate,  $\sigma$ , as a function of field in samples with two non-spin-zero species.

- (a) The  $B_0$  field is raised to match the secondary species',  $S$ , resonance of the probe at a rate of  $\Delta_1 = 8 \text{ Ts}^{-1}$ . To recreate identical polarisation conditions at the beginning of each run the secondary spins are saturated with a train of 12  $\pi/2$  radio frequency (RF) pulses.
- (b) The system is polarised at a field  $B_{pol} = B_R$  for a time  $\tau_{pol}$ , allowing the secondary species' magnetisation to reach thermal equilibrium.
- (c) Then the primary species',  $I$ , spins are saturated, at their probe resonance field, with 12  $\pi/2$  RF pulses. This stage is shortened as much as possible to minimise the recovery of secondary spin magnetisation during this time, and preserve the initial polarisation conditions,  $\langle I_z \rangle_{t=0} = 0$   $\langle S_z \rangle_{t=0} = S_0$ .
- (d) The sample magnetisation is allowed to recover at a field  $B_R$ , for a time  $\tau_R$ . The recovery time,  $\tau_R$ , is incremented logarithmically after each run. For convenience, the beginning of this section is set to be at time  $t = 0$ .
- (e) The field is then switched back to  $B_S$ , at a rate of  $\Delta_2 = 5 \text{ Ts}^{-1}$  for increased field stability, and the magnetisation is measured with a single  $\pi/2$  RF pulse.

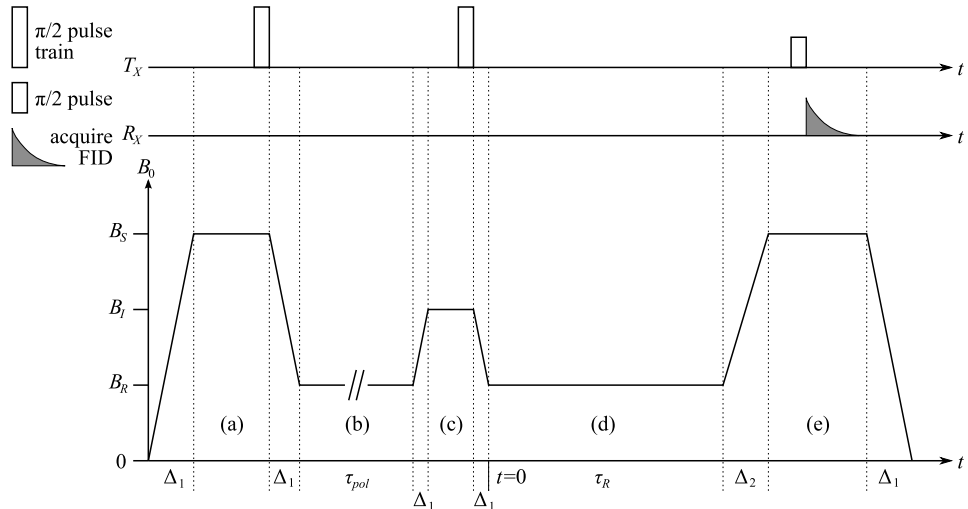


Figure 3.12: The cross-relaxation pulse sequence. Schematic: the axes are not to scale.

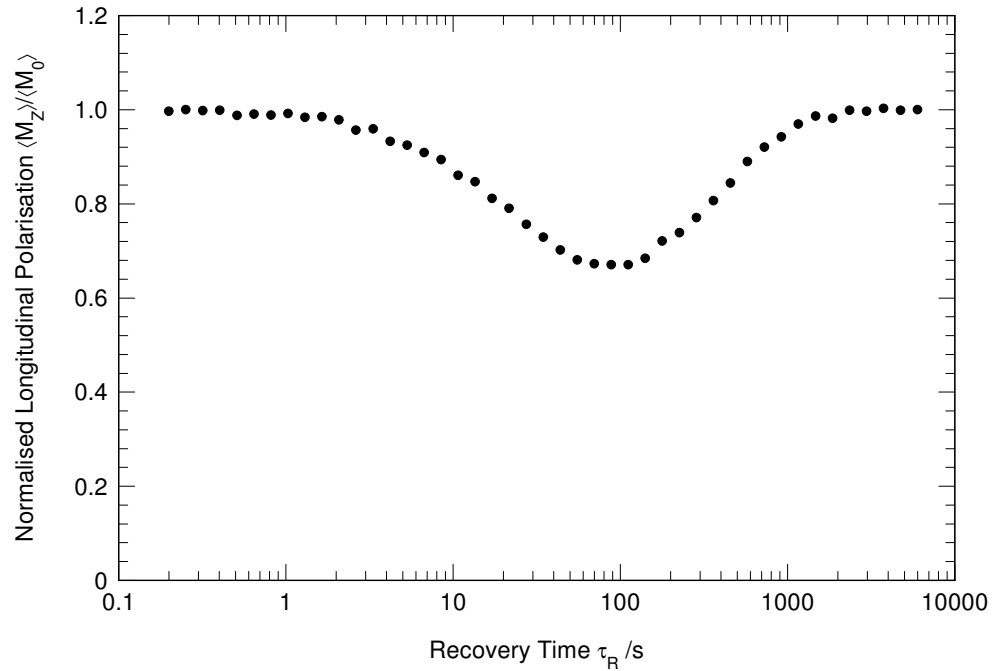


Figure 3.13: Sample cross-relaxation experiment data.

Figure 3.13 shows a typical cross-relaxation experiment data set, with the measured species' polarisation being initially disturbed from thermal equilibrium by the saturated species until the polarisations of both equilibrate. A negative value of the cross-relaxation rate,  $\sigma$ , results in a polarisation 'dip' as shown by this figure. Correspondingly, a positive cross-relaxation rate would be exemplified by an initially increasing polarisation - forming a 'peak' in the magnetisation recovery.

## Chapter 4

# The Isotope Effect

### 4.1 Introduction

This set of experiments was designed to observe experimentally and quantify the isotope effect of the carboxyl group oxygen atoms on the proton transfer dynamics of the hydrogen bonds in benzoic acid (BA). The isotope effect of the nucleon undergoing transfer, due to a change in its mass, on the tunnelling dynamics has been observed [13], with a greatly reduced correlation rate for deuterons undergoing transfer than for hydrogen nuclei. Although the importance of the particle mass undergoing transfer can be easily seen in terms of quantum mechanics, the effect on this process of a nearby atom, which is relatively stationary, is far less tangible.

In terms of the basic model of proton transfer, the molecular lattice is assumed to be stationary. In reality however, proton transfer is accompanied by distortions of the molecular lattice, such as the C–O bond length in the carboxyl group as it changes from a single to a double bond [25]. From the quantum-mechanical perspective, the motion experienced by these heavy lattice atoms during proton transfer would have a finite tunnelling matrix element [7], and a complete description of proton transfer would therefore have to take such lattice vibrations into account. However, instead of treating the entire molecular lattice as one quantum object involved in the the tunnelling phenomenon, the model can be simplified to a single particle experiencing a modified PES. This then becomes an elaboration of the basic system, of a proton within a static DMP, with the modified proton mass and PES accounting for contributions from specific molecular vibrational modes, which may augment or hinder proton transfer.

It is known that for the DMP model, the ground-state tunnelling correlation rate,  $\tau_c^{-1}$ , is proportional to the square of the tunnelling matrix element [10], and the tunnelling matrix element is known to be proportional to the exponent of the square root of the proton mass. Therefore the tunnelling matrix elements of the heavy lattice atoms will be strongly influenced by their mass, which will in turn affect the observed proton tunnelling. Following on from the discussion above, this can be applied to the modified single particle motion model; if the carboxyl oxygen motion contributes positively to proton transfer, then an increase in its mass would be accounted for by an increase in the effective proton mass. This would then manifest itself as a decrease in the low-temperature proton transfer rate, measured by spin-lattice relaxation. This effect should then diminish at high temperature as the emphasis for the proton transfer mechanism moves away from ground-state tunnelling transitions towards thermally activated barrier hopping and becoming less dependent on the particle mass.

Previous experiments using optical spectroscopy combined with preliminary calculations of the molecular lattice tunnelling matrix elements have estimated that in  $^{18}\text{O}$ -BA the reduction of the proton transfer rate in the low-temperature limit,  $k_0$ , is of the order of  $(15 \pm 7)\%$  compared with  $^{16}\text{O}$ -BA [26]. Experiments on carbon-13 enriched benzoic acid [27] attempted to show this effect, however with the added complication of heteronuclear relaxation effects, it was found too small to resolve.

The purpose of this investigation was to measure the effect on the proton transfer rate more accurately, and to show a convergence at higher temperatures away from the incoherent tunnelling regime.

## 4.2 Experimental Procedure

As explained in chapter 2, the ensemble average proton transfer rate can be directly probed using the correlation time,  $\tau_c$ , associated with the motion. Spectral density profiles were acquired by measuring the spin-lattice relaxation rate at a range of recovery fields and fixed temperature. Each spectral density was then analysed with an equation of the form (2.59) to extract a correlation time at that temperature. This procedure was then repeated for a range of temperatures for both samples to analyse their relative temperature-dependent dynamics.

Both the homonuclear saturation recovery (subsection 3.3.2) and homonuclear polarisation recovery (subsection 3.3.3) pulse sequences were used for this set of experiments. Generally speaking, for recovery fields below ca. 0.5 T the magnetisation at thermal equilibrium was too low to measure the spin-lattice relaxation time reliably using the saturation recovery sequence. In these instances the polarisation recovery sequence was used instead to increase the dynamic range of the measured magnetisation. In the high-field and low-temperature regime the spin-lattice relaxation time was very long and a reduced form of saturation recovery experiment was performed to save time. In this instance the magnetisation recovery was measured in the range  $T_1/1000 < \tau_R < 2T_1$  in addition to a single measurement of the equilibrium magnetisation at  $\tau_R = 10T_1$ . The increased signal to noise ratio at low-temperature and high-field compensated for the decreased accuracy of the  $T_1$  measurement from this experiment.

Due to the fact that the isotope effect produced by this substitution was expected to be very small, special precautions had to be taken to ensure accuracy. For both samples ultra-pure zone-refined powdered crystals of benzoic acid were used to reduce contributions from impurities and negate any sample orientation dependence from the results. The  $^{16}\text{O}$ -BA sample had 99.76% natural abundance of the oxygen-16 isotope, and  $^{18}\text{O}$ -BA was specifically prepared to have >98% abundance of the oxygen-18 isotope in the carboxyl group as shown in figure 4.1. Both  $^{16}\text{O}$  and  $^{18}\text{O}$  nuclei have spin-0, so there were no heteronuclear contributions to the relaxation time due to them.

Furthermore, a systematic comparative study had to be performed on both samples in order to reliably measure the small differences in dynamics between the two. The spectral density profiles were sampled at the same set of recovery fields for a given temperature and at the same temperatures for both samples. This avoided biasing the data for one of the samples towards a particular

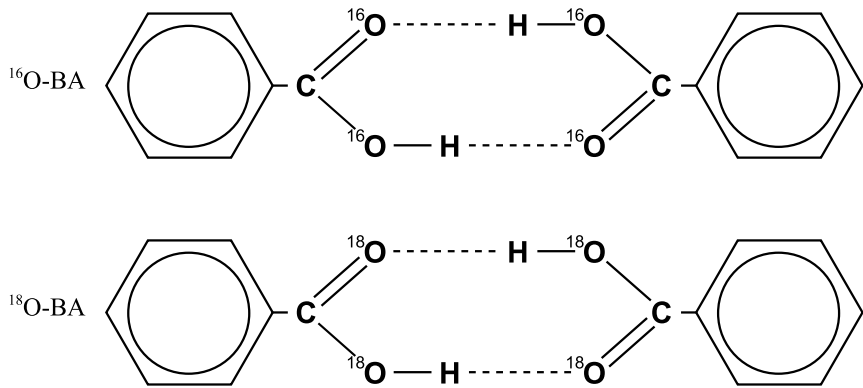


Figure 4.1: Dimerised benzoic acid molecules showing the carboxyl oxygen isotopic substitution sites.

feature of the dynamics, and not the other. To reduce inconsistency due to equipment, all measurements were performed using the 38.64 MHz probe, using the same calibration procedures for both.

Although the temperature-dependence of the benzoic acid proton transfer correlation time has already been studied across a large range of temperatures [8], this was done with a different set of equipment. For this comparative study the measurements of <sup>16</sup>O-BA were repeated with improved thermometry. However, the same sample was used here as for those experiments, so that some measure of the reliability of the previous experiments could be made.

## 4.3 Results

The results from the saturation recovery and polarisation recovery experiments were analysed with unconstrained fits to equations (3.2) and (3.4) respectively, to measure the spin-lattice relaxation time.

The spectral density profile for a given temperature should be modelled by equations (2.59, 2.60), where it is known that the dipolar coupling constant,  $C_{II}$ , and enthalpy change,  $\Delta H$ , are independent of field and temperature. To preserve this equality between the spectral densities of one sample and allow a more reliable measure of  $\tau_c$ , a two-stage fitting process was used. Firstly, the spectral densities were individually fitted to

$$\frac{1}{T_1} = D [L(\omega_I, \tau_c) + 4L(2\omega_I, \tau_c)] + b, \quad (4.1)$$

with a single combined amplitude parameter  $D$ . The constant offset,  $b$ , was added to account for small impurities in the sample, such as water adsorbed onto the crystal surface. The spectral density data and lines of best fit from this equation are shown in figures 4.3 and 4.4 for both samples. It is possible to observe the isotope effect gain prominence as the sample is cooled and the relaxation becomes dominated by ground-state tunnelling simply from a qualitative analysis of these spectral densities. At the highest measured temperature of 80 K the spectral densities appear parallel, indicating that the their width, characterised by  $\tau_c^{-1}$ , is approximately equal. With decreasing temperature however, the spectral densities of the two samples begin to cross over as their correlation rates diverge due to the isotope effect. From this casual examination it is also possible to see that the spectral density amplitudes are consistently different for the two samples across the full range of temperatures, as will be analysed in more detail in subsection 4.3.1.

After measuring the spectral density amplitudes of a given sample for all temperatures, apart from 80 K, they were fitted to the following equation

$$D = C_{II} \frac{4a}{(1+a)^2}, \quad (4.2)$$

to extract the two constants  $C_{II}$  and  $\Delta H$  for that particular sample. The maximum spectral width of the field-cycling spectrometer (2.5 T) was insufficient to reliably measure both the amplitude,  $D$ , and width,  $\tau_c^{-1}$ , of the spectral densities at 80 K. For this case it was decided to constrain the amplitude in

the spectral density equation (4.1) based on an extrapolation of equation (4.2) from the amplitudes at the other temperatures.

An added complication was discovered during the analysis of the spectral densities in the form of relaxation due to oxygen-17. It was possible to observe this relaxation contribution as ‘quadrupolar peaks’ at low field despite the low abundance of the isotope due to the inherent strength of quadrupole coupling [13]. This contribution was strongest for  $^{18}\text{O}$ -BA at the lowest temperature, 13.333 K, and could be isolated at fields below 0.175 T. The difference in contributions from the two samples could be explained by an increased proportion of  $^{17}\text{O}$  in  $^{18}\text{O}$ -BA due particularities of the isotopic substitution process. As a result of this inconsistency it was necessary to ensure that the  $^{17}\text{O}$  spectrum was completely omitted from all spectral density fits, otherwise the inequivalent small contributions would introduce a discrepancy in the comparison of the two samples. To this end, no measurements of the  $T_1$  below 0.175 T were used in the fitting to equation (4.1).

The small spectral density constant offsets,  $b$ , were analysed and were found to be equivalent for both samples, within error. Translated into an effective relaxation time, the inverse offsets are on average an order of magnitude larger than the longest  $T_1$  measured at the same temperature, but have a similar temperature-dependence. These features indicate that the impurity present in both samples has very low abundance but with dynamics similar to benzoic acid.

### 4.3.1 Spectral Density Amplitudes

Figure 4.5 shows the final data analysis of the spectral density amplitudes for the two samples. The consistent difference in spectral density amplitudes noted earlier can now be seen clearly in figure 4.5. This difference manifests itself as an offset between the two parallel lines, due to a lower dipolar coupling strength,  $C_{II}$ , for  $^{16}\text{O}$ -BA than for  $^{18}\text{O}$ -BA. A check was performed to ensure that this inequality was real and not an artifact of the fitting algorithm; by constraining  $\Delta H$  during fits to equation (4.2) to its maximum or minimum values within the measured error for that variable, the values for  $C_{II}$  shown in figure 4.5 and table 4.1 were confirmed.

This phenomenon can be explained by isotopic substitution when we consider what effect the change in atomic mass would have on the molecular structure. A heavier nucleus would have a lower energy ground state, and due

to the anharmonicity of the covalent bond potential this results in the bond lengths with  $^{18}\text{O}$ -BA being shorter than those with  $^{16}\text{O}$ -BA, see figure 4.2.

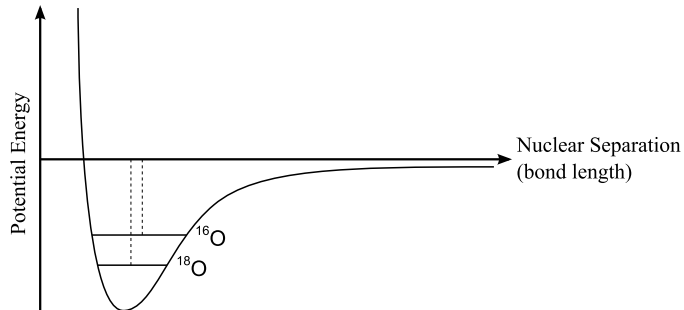


Figure 4.2: A schematic diagram of intramolecular bond lengths shortened by the nuclear isotope effect (axes not to scale).

By utilising the low-temperature crystal structure of  $^{16}\text{O}$ -BA [15] and applying equation (2.60) an estimate of the isotope effect necessary to account for the observed difference in  $C_{II}$  was made. Due to the  $r^{-6}$  dependence of  $C_{II}$  it was decided to limit the calculation to just the leading term in the dipolar sum from the nearest carboxyl protons. Also, for simplicity, it was assumed that the only structural change due to the heavier isotope was a shift of the carboxyl proton position closer to its neighbouring oxygen. These preliminary calculations showed that a displacement of just 0.038 Å was sufficient increase the  $^{16}\text{O}$ -BA  $C_{II}$  by 10.5% in accordance with the results, which equates to roughly 4% of the O–H bond length. Although the carboxylic proton separation increased with this structural change, the slight increase in the subtended angle  $\alpha$  was sufficient to counteract this, showing that the dipolar constant is highly sensitive to such small changes.

In reality however, a shortening of the oxygen atom covalent bonds will result in greater changes to the carboxylic group geometry than modelled here, as well as a compression of the entire unit cell. Therefore a more rigorous analysis of the isotope effect on the dipolar coupling strength cannot be performed until the low-temperature crystal structure of  $^{18}\text{O}$ -BA is measured.

### 4.3.2 Proton Transfer Correlation Rates

The correlation rates measured directly from the spectral densities for both samples are shown in figure 4.6. To quantify the temperature-dependence of the proton transfer dynamics, determined by the inverse correlation time, a

least-squares fit of the data was performed to equation (2.62). Because the high-temperature dynamics were not explored in this investigation, it was necessary to constrain the fit by using a previously-established parameter for the high-temperature correlation rate,  $\tau_{exc}$  [16]. The change in enthalpy,  $\Delta H$ , measured from a fit of the spectral density amplitudes to equation (4.2), was more accurate than could be achieved by fitting to the correlation rates. Hence,  $\Delta H$  for both samples was constrained in equation (2.62) to the values shown in figure 4.5 and table 4.1.

As can be seen from figure 4.6, this set of experiments has successfully shown that the isotope effect on the proton transfer dynamics becomes diminished at high temperature as the system moves away from the incoherent tunnelling regime. The low-temperature proton transfer rate constant,  $k_0$ , has been measured for both samples to a high degree of accuracy, and a careful systematic study was performed to ensure that any observed difference was due to the isotope effect. This isotope effect, due to carboxyl-oxygen substitution, can be measured as a comparison of the low-temperature rate constants,

$$1 - \frac{k_0^{(18)}}{k_0^{(16)}} = (15.2 \pm 0.5)\%, \quad (4.3)$$

which is in agreement with the previous estimate of  $(15 \pm 7)\%$ , [26].

A summary of the thermodynamic model parameters measured for each sample is shown for comparison in the table below.

	<sup>18</sup> O-BA	<sup>16</sup> O-BA
$C_{II}$	$(7.76 \pm 0.03) \times 10^7 \text{ s}^{-2}$	$(7.02 \pm 0.02) \times 10^7 \text{ s}^{-2}$
$k_0$	$(1.181 \pm 0.005) \times 10^8 \text{ s}^{-1}$	$(1.393 \pm 0.006) \times 10^8 \text{ s}^{-1}$
$\Delta H/k_B$	$84.23 \pm 0.08 \text{ K}$	$84.67 \pm 0.07 \text{ K}$
$\tau_{exc}^{-1}$	$(2.4 \pm 0.2) \times 10^9 \text{ s}^{-1}$	$(2.7 \pm 0.2) \times 10^9 \text{ s}^{-1}$
$\Delta E_{exc}/k_B$	$117 \pm 3 \text{ K}$	$125 \pm 3 \text{ K}$
$\tau_{act}^{-1}$	$1.14 \times 10^{12} \text{ s}^{-1}$ [16]	$1.14 \times 10^{12} \text{ s}^{-1}$ [16]
$\Delta E_{act}/k_B$	$560 \pm 2 \text{ K}$	$564 \pm 2 \text{ K}$

Table 4.1: Best-fit parameters used to describe the relaxation observed in <sup>18</sup>O-BA and <sup>16</sup>O-BA.

## **4.4 Summary**

This successful study has made an important advancement to further the understanding of molecular dynamics on a quantum level, whereby the entire molecule undergoes tunnelling together with the proton, allowing future theoretical descriptions to be made with more confidence based on these results. In addition, convergence of the high-temperature correlation rates clearly demonstrated that the quantum mechanical effects diminished with increasing temperature, as the de Broglie wavelength of the protons decreased.

Eliciting the subtle differences in dynamics due to the isotope effect was aided by the considerable stability of the spectrometer system and routines over the course of several months of continuous experiments. This, combined with ultra-pure zone-refined samples and meticulously consistent measurement techniques allowed great confidence to be placed in the final results being primarily due to the desired effect.

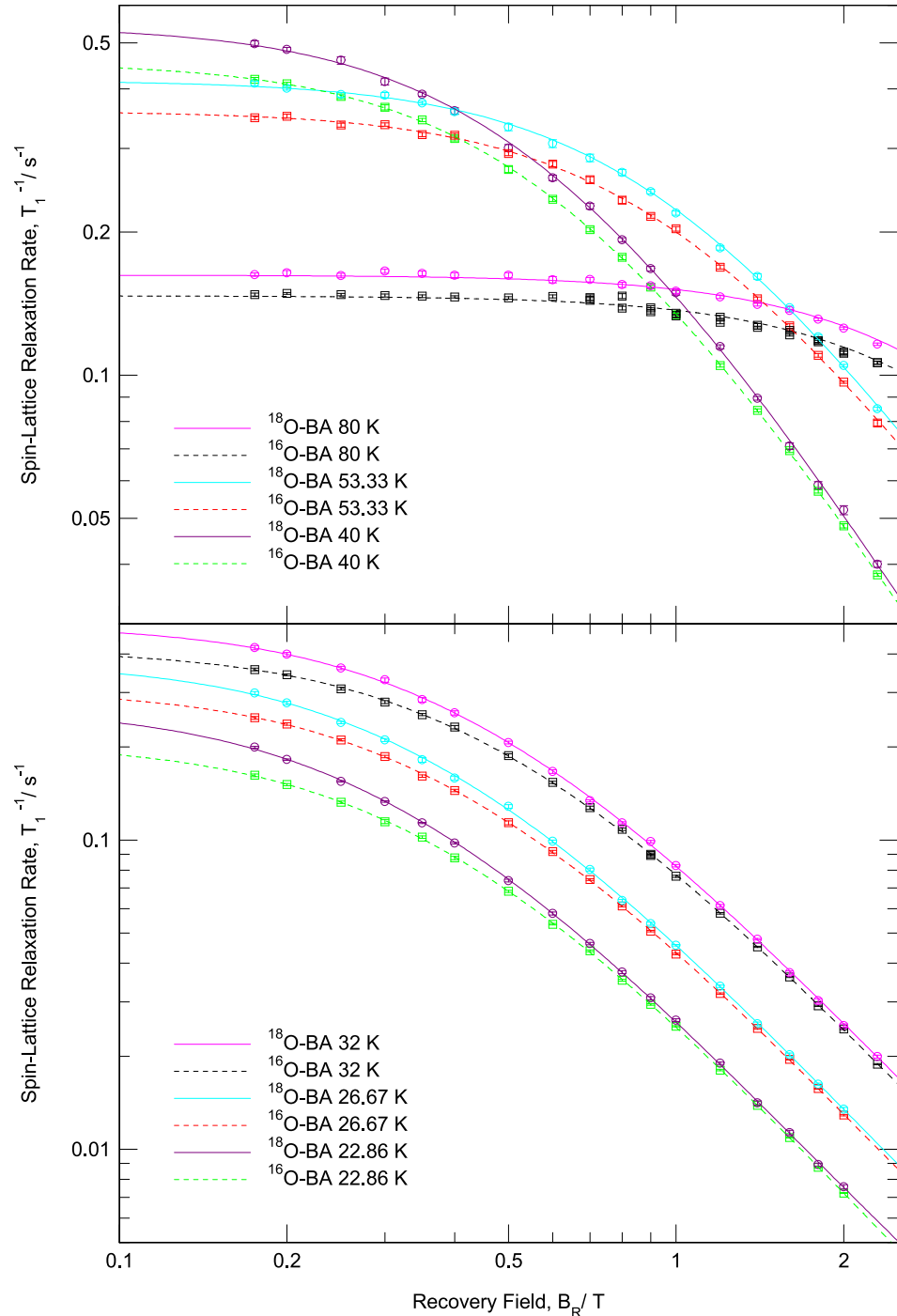


Figure 4.3: Spectral densities of  $^{18}\text{O-BA}$  (circles) and  $^{16}\text{O-BA}$  (squares) measured at a range of temperatures. The solid and dashed lines are fits to equation (4.1).

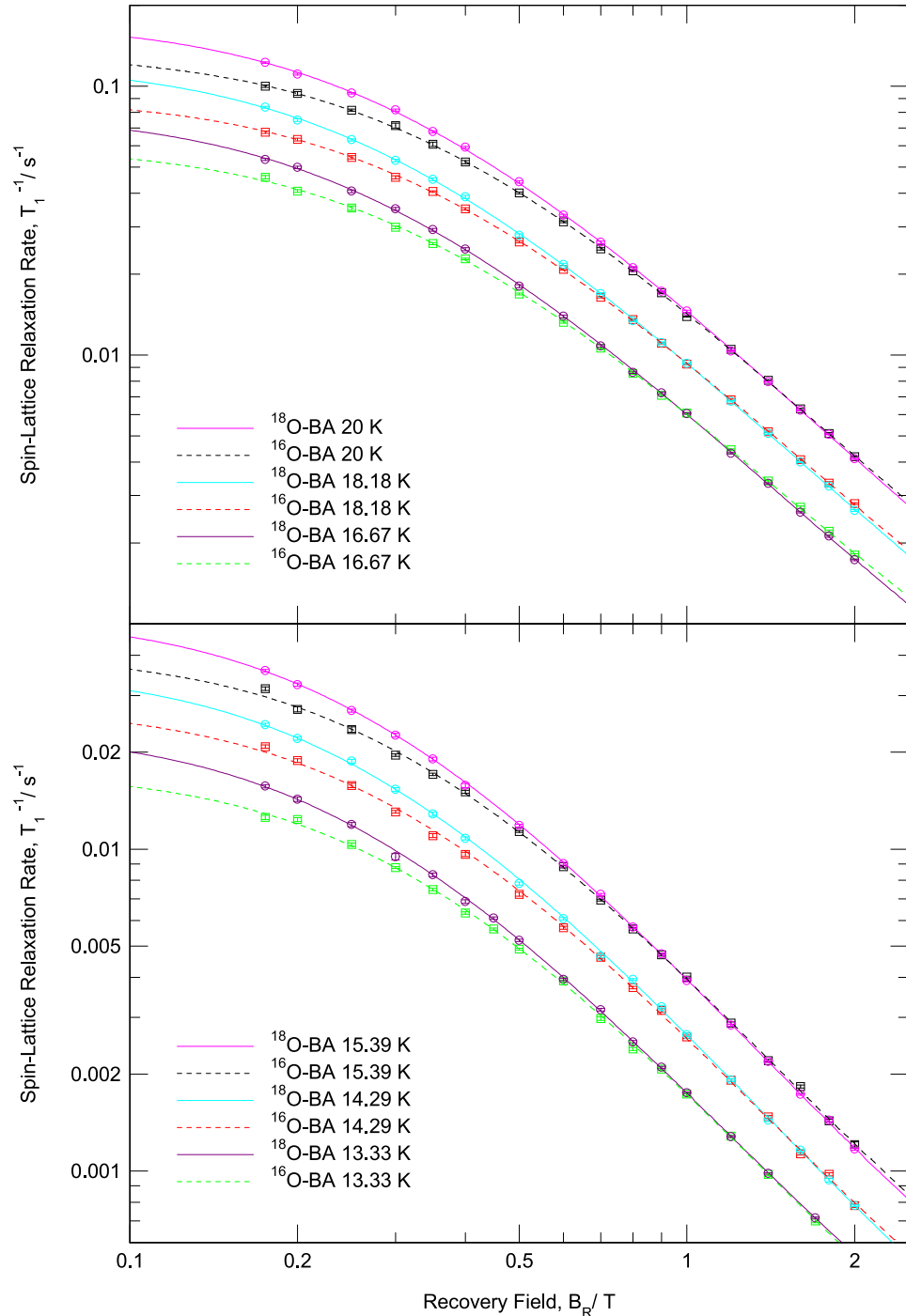


Figure 4.4: Spectral densities of  $^{18}\text{O-BA}$  (circles) and  $^{16}\text{O-BA}$  (squares) measured at a range of temperatures. The solid and dashed lines are fits to equation (4.1).

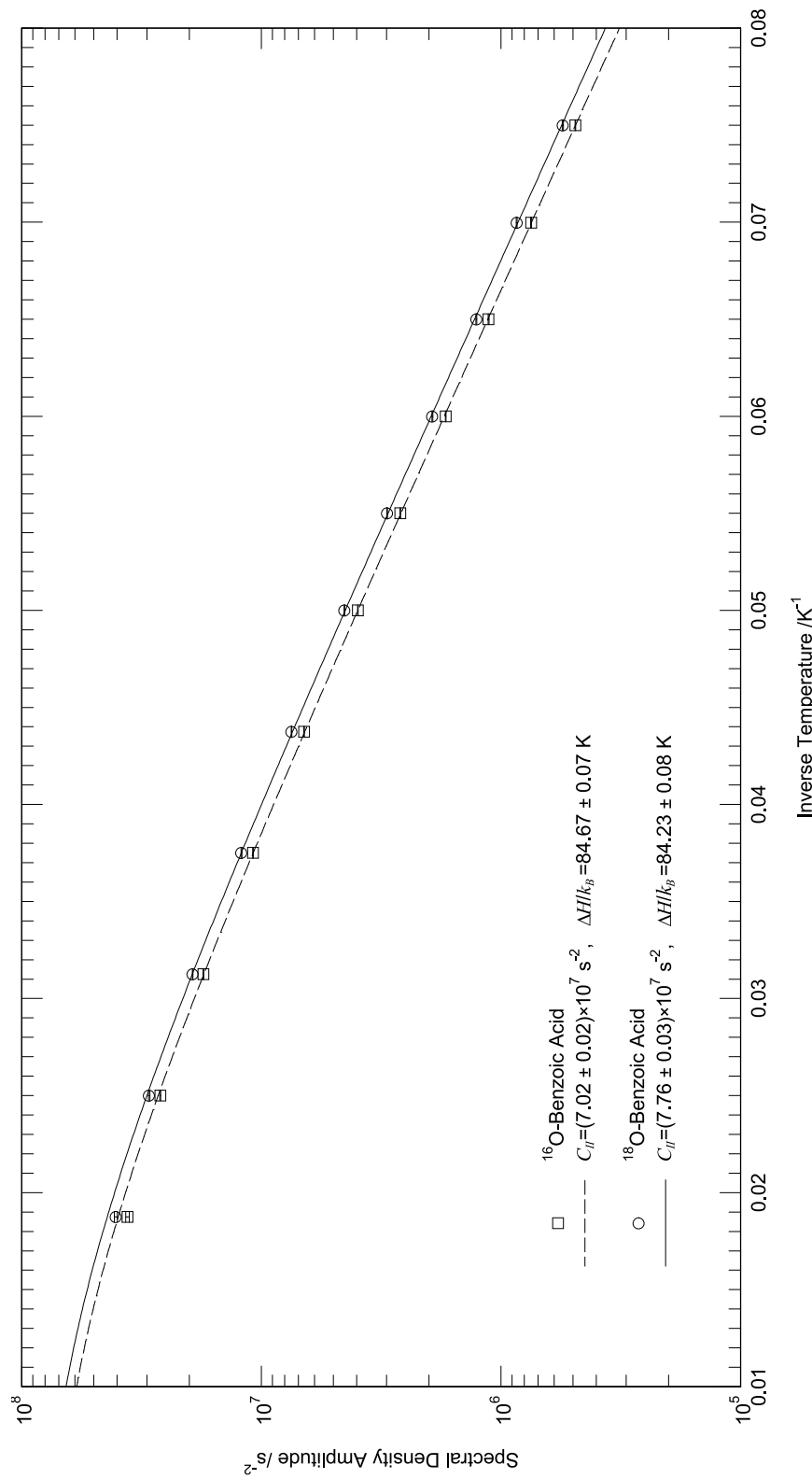


Figure 4.5: The spectral density amplitudes,  $D$ , of  $^{16}\text{O}$ -BA and  $^{18}\text{O}$ -BA are shown in this figure as a function of inverse temperature. The solid and dashed lines represent unconstrained least squares fits to equation (4.2).

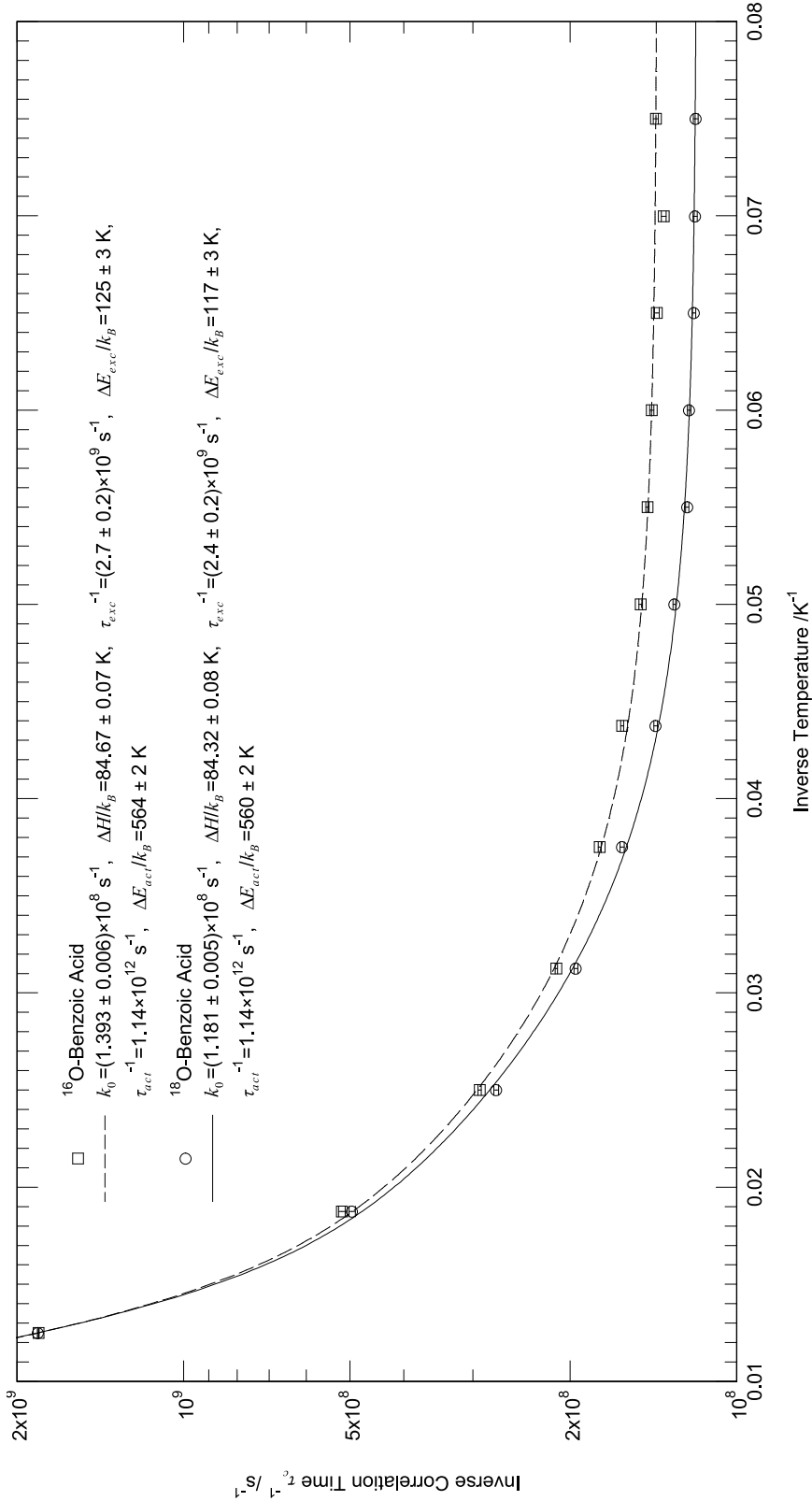


Figure 4.6: The measured inverse correlation times,  $\tau_c^{-1}$ , of both  ${}^{16}\text{O}\text{-BA}$  and  ${}^{18}\text{O}\text{-BA}$  are shown in this figure as a function of inverse temperature. The solid and dashed lines represent constrained least squares fits to equation (4.1).

## Chapter 5

# Heteronuclear Cross-Relaxation

### 5.1 Introduction

The equilibrium polarisation of  $^{13}\text{C}$  is naturally lower than that of protons due to a smaller magnetogyric ratio, see table 2.1, which hinders accurate measurement of its relaxation. However, standard measures for increasing the polarisation, by going to high field and low temperature, have the adverse effect of significantly increasing the relaxation rate and becoming increasingly expensive. By exploiting the dipolar coupling between different spin species it is possible to bypass these difficulties and transfer the large polarisation of one species to another with a low polarisation. This coupling interaction occurs through double and zero-quantum spin flips, as discussed in subsection 2.2.3, which are rendered time-dependent by the application of an RF at the matching frequency. Such transitions can either be driven manually by irradiating the sample (nuclear solid effect) [28], or allowed to happen naturally by interaction with a local dipolar field from stochastic molecular motion. The latter of these two modes will be investigated here, with the aim of adding to the development of techniques for polarisation transfer, and enhancing the understanding of relaxation in heteronuclear spin systems involving other common organic species, in this case fluorine.

In order for the local dipolar field to have sufficient bandwidth to drive these transitions, the stochastic molecular motion should be relatively fast at low temperature, where the polarisation is largest. Incoherent proton transfer

in the carboxylic dimer of benzoic acid provides such a system, and therefore presents a good ‘host molecule’ for studying cross-relaxation effects.

These experiments were conducted as a continuation of earlier work on compounds that exhibited coupling between the heteronuclear and homonuclear Zeeman reservoirs. Non-zero off-diagonal relaxation matrix elements,  $\sigma$ , were detected in carbon-13 substituted benzoic acid ( $^{13}\text{C}$ -BA), based on initial studies showing that the  $^{13}\text{C}$  spin-lattice relaxation rate depended strongly on the initial polarisation state of the proton reservoir [27]. In addition, a preliminary temperature-dependent study of 2,4,6-fluorobenzoic acid (2,4,6-FBA) exhibited multiple relaxation rates of the proton reservoir at low temperature. This is strongly indicative of a cross-relaxation process, supported by measurements of  $\sigma$  in previous work on a similar sample (2,3,5,6-FBA) [29].

Figures 5.1 and 5.2 show the the molecular structure of the benzoic acid dimers studied. For 2,4,6-FBA, three of the aromatic-group hydrogen atoms had been replaced with fluorine, in specific positions around the benzene ring. It is likely that significant changes would occur to the crystal lattice as a result of this substitution, compared with pure benzoic acid. As discussed in section 2.2, this would in turn affect the DMP characteristics such as the asymmetry, and has been demonstrated by previous studies on other fluorobenzoic acids [30, 29].

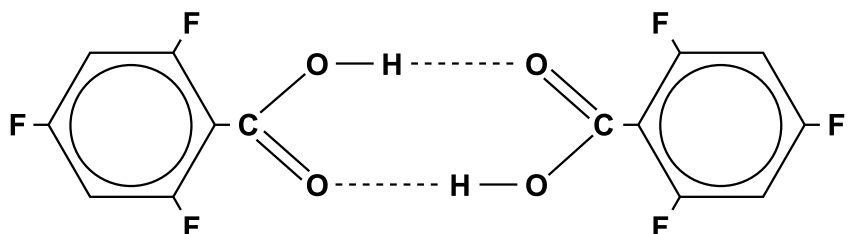


Figure 5.1: Molecules of 2,4,6-fluorobenzoic acid in a dimer configuration.

The  $^{13}\text{C}$ -BA sample was prepared by isotopic substitution of just the carboxyl group carbons with carbon-13 to 99% purity, as shown in figure 5.2. In contrast to the fluorobenzoic sample, this substitution would have little effect on the crystal lattice, and the static DMP is expected to undergo little change. However, as discussed in chapter 4, if vibrational modes involving this carbon atom contribute to proton transfer, then an isotope effect could manifest itself as a small change in the ground-state tunnelling rate  $k_0$ .

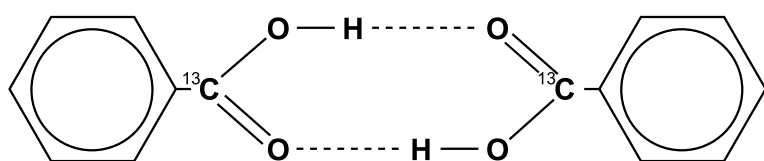


Figure 5.2: Molecules of carbon-13 substituted benzoic acid in a dimer configuration.

Utilising the field-cycling spectrometer, these experiments attempted to characterise the frequency-dependence of the off-diagonal relaxation matrix elements,  $\sigma$ . In the case of <sup>13</sup>C-BA the magnetisation recovery of <sup>13</sup>C spins were detected directly, to determine the scope of cross-polarisation. An accurate measurement of fluorine spins in 2,4,6-FBA was not possible because the the fluorine signal from the Kel-F NMR coil former provided significant interference. Although making a coil former from sulphur or ceramic could overcome this obstacle, it was not feasible for this study due to time constraints. Therefore, the cross-relaxation rate was measured from the proton magnetisation recoveries instead.

## 5.2 Experimental Procedure

The spin-lattice relaxation of 2,4,6-FBA was first measured as a function of temperature to establish the temperature range over which cross-relaxation is observed. To ensure reproducible results, the initial polarisations of both fluorine and proton spin reservoirs were controlled by employing the heteronuclear saturation recovery pulse sequence for these measurements (subsection 3.3.4). The recovery field used was 0.61 T.

Following these preliminary experiments, the cross-relaxation pulse sequence (subsection 3.3.6) was used with both samples, to measure the deviation from equilibrium of the secondary species magnetisation as the primary species recovered from saturation. For the 2,4,6-FBA measurements, due to the Kel-F former, only the proton spins could be observed. Therefore these experiments measured the proton (primary) magnetisation being disturbed by saturation of the fluorine (secondary) spins.

Using a range of recovery fields allowed the spectral density profile of the cross-relaxation matrix element to be measured from the primary and secondary relaxation rates,  $R_1$  and  $R_2$ . The specific fields used were: 0.3 – 2 T for  $^{13}\text{C}$ -BA, and 0.2 – 1.3 T for 2,4,6-FBA. The experiments were conducted at low temperature (20 K for  $^{13}\text{C}$ -BA and 18 K for 2,4,6-FBA) as a compromise between the increased SNR and relaxation times. A measurement of the ground-state tunnelling frequency,  $k_0$ , was also desired from the  $^{13}\text{C}$ -BA measurements, to determine if any isotope effect was present in the proton transfer dynamics.

Due to a low abundance of the  $^{13}\text{C}$  spins, small magnetogyric ratio, and narrow lineshape, the  $^{13}\text{C}$ -BA NMR signal was much weaker compared to protons. In order to reliably distinguish the deviations from equilibrium magnetisation, as a result of cross-relaxation, it was necessary to average the signal amplitudes over several runs for each recovery time. This was also required to a lesser degree for 2,4,6-FBA at low recovery fields.

It can be seen from table 2.1 that the magnetogyric ratios of protons and fluorine are very similar. During cross-relaxation experiments on 2,4,6-FBA, where it is intended for one spin species to be saturated whilst the other maintains a constant polarisation, it was found that the fluorine saturation pulses were also affecting the proton reservoir. For the reasons discussed in subsection 3.1.1 it is generally advantageous to use short, powerful pulses, which have a broad frequency-space distribution. In this case however, long fluorine saturation pulses had to be used, to reduce their perturbation of the

proton reservoir. It was impossible to completely eliminate these concurrent affects, and also ensure complete saturation of the fluorine spins; therefore, the polarisation field,  $B_{pol}$ , was generally set to 0.05 T higher than the recovery field to compensate.

Both samples used were powdered crystals, with purity levels of 98% for 2,4,6-FBA, and 99% for  $^{13}\text{C}$ -BA.

### 5.3 Results

In these heteronuclear samples, with non-zero cross-relaxation, it is sometimes the case that the weighting coefficients and relaxation rates combine in such a way as to make the magnetisation recovery appear to have a single relaxation rate, as discussed in subsection 2.2.3. This was the case for the temperature-dependent 2,4,6-FBA measurements above c.a. 40 K, which were therefore analysed with equation (3.2) to extract an effective relaxation time. Below that temperature multiple relaxation rates could be reliably measured, and the magnetisation recovery data was fitted to equation (3.3). To extract more accurate measurements of the relaxation rates, no constraints on the weighting coefficients,  $c_1$  and  $c_2$ , were placed for these fits based on initial polarisation conditions.

Unless the system is completely decoupled from the lattice it is not possible to measure the cross-relaxation rate directly; it instead has to be inferred from the heteronuclear relaxation rates,  $R_1$  and  $R_2$ . The cross-relaxation pulse sequence is designed to allow clear separation of these relaxation rates, even if they are of similar magnitude. Therefore the cross-relaxation magnetisation recovery curves were analysed using equation (3.3) to measure the two rates. Based on the initial reservoir polarisations, the weighting coefficients were constrained during these fits to  $c_2 = -c_1$ . This was done for both samples to ensure that any model derived from the measurements was self-consistent and could be used to reproduce the data.

Technically, analysis of the  $^{13}\text{C}$ -BA cross-relaxation data produces a measurement of  $\sigma_I$ , whereas for 2,4,6-FBA the other cross-relaxation rate is measured  $\sigma_S$ , based on equations (2.31) and (2.28) respectively. However, because all the magnetic species in these heteronuclear samples have the same spin quantum number,  $I = S = 1/2$ , the two rates are equivalent,  $\sigma_I = \sigma_S$ . Furthermore, under such circumstances it becomes convenient to assign a general heteronuclear dipolar constant for powdered samples,

$$C_{IS} = \frac{\gamma_I^2 \gamma_S^2 \hbar^2 S(S+1)}{30N_I} \left(\frac{\mu_0}{4\pi}\right)^2 \sum_{k,j} \left[ r_{kjL}^{-6} - r_{kjL}^{-3} r_{kjR}^{-3} (3 \cos^2 \alpha - 1) + r_{kjR}^{-6} \right], \quad (5.1)$$

in contrast to the homonuclear dipolar constant  $C_{II}$  given by equation (2.60).

### 5.3.1 $^{13}\text{C}$ -Benzoic Acid

The cross-relaxation experiment magnetisation recoveries at 20 K and various recovery fields are shown in figure 5.4. It can be seen clearly from these plots that the  $^{13}\text{C}$  polarisation increases as the saturated proton reservoir cross-relaxes into the  $^{13}\text{C}$  reservoir. This enhancement is most significant at low recovery fields, decreasing from around 25% at 0.3 T towards approximately 10% at 2 T.

This increase in the  $^{13}\text{C}$  polarisation is indicative of a positive off-diagonal relaxation matrix element, despite a negative Lorentzian contribution shown in equation (2.53). This is due to the relatively small  $^{13}\text{C}$  magnetogyric ratio compared with protons, meaning that  $(\omega_I - \omega_S) \approx (\omega_I + \omega_S)$ , and the resulting cross-relaxation rate effectively becoming dependent on  $5L(\omega_I)$ . This is contrary to fluorobenzoic acids, where the wide  $-L(\omega_I - \omega_S)$  component tends to dominate.

It can also be seen from figure 5.4 that despite copious signal amplitude averaging, the magnetisation recovery curves still show significant experimental scatter. The resulting signal quality was insufficient to enable a procedure based solely on constrained fits to this data, so a modelling approach was adopted instead. Using model parameters derived from the nuclear solid effect and temperature-dependent experiments [28, 27] as a basis, the magnetisation recovery curves were simulated using equation (2.26b). This approach showed a much better agreement and required only a small adjustment of the model parameters to describe the data presented here within experimental error. Table 5.1 shows the thermodynamic model parameters that best describe all available data and are used to calculate the solid lines in figure 5.4. The cross-relaxation rate,  $\sigma$ , field-dependence at 20 K was then calculated based on these parameters and is shown in figure 5.3.

The low-temperature proton transfer tunnelling rate limit,  $k_0$ , measured from these results is slightly smaller than that of pure benzoic acid ascertained in previous experiments, presented in chapter 4. This implies that motion of the carboxyl carbon atoms contributes to proton transfer; similarly to the oxygen atoms in their vicinity but to a lesser degree. An estimate of the isotope effect can therefore be made from this difference in rates,  $1 - k_0^{(13\text{C})}/k_0^{(16\text{O})} = 8\%$ . Unfortunately, this measurement is within systematic experimental uncertainties, but can be improved by conducting a comparative study, similar to that presented in chapter 4.

Generally speaking, determination of a positive cross-relaxation rate, from direct measurement of the  $^{13}\text{C}$  spins, bolsters the avenue of research into enhancing the polarisation of a naturally weak carbon signal. Similarly to the nuclear solid effect, the intrinsic dipolar coupling present in such molecular systems provides a cross-polarisation pathway to the  $^{13}\text{C}$  reservoir by manipulating the abundant proton spins.

$^{13}\text{C-BA}$	
$C_{II}$	$6.93 \times 10^7 \text{ s}^{-2}$
$C_{IS}$	$1.22 \times 10^7 \text{ s}^{-2}$
$k_0$	$(1.28 \pm 0.6) \times 10^8 \text{ s}^{-1}$
$\Delta H/k_B$	80 K
$\tau_{exc}^{-1}$	$1 \times 10^{10} \text{ s}^{-1}$ [16]
$\Delta E_{exc}/k_B$	180 K [16]
$\tau_{act}^{-1}$	$1.14 \times 10^{12} \text{ s}^{-1}$ [16]
$\Delta E_{act}/k_B$	600 K [16]

Table 5.1: Best-fit parameters used to describe the relaxation observed in  $^{13}\text{C-BA}$ .

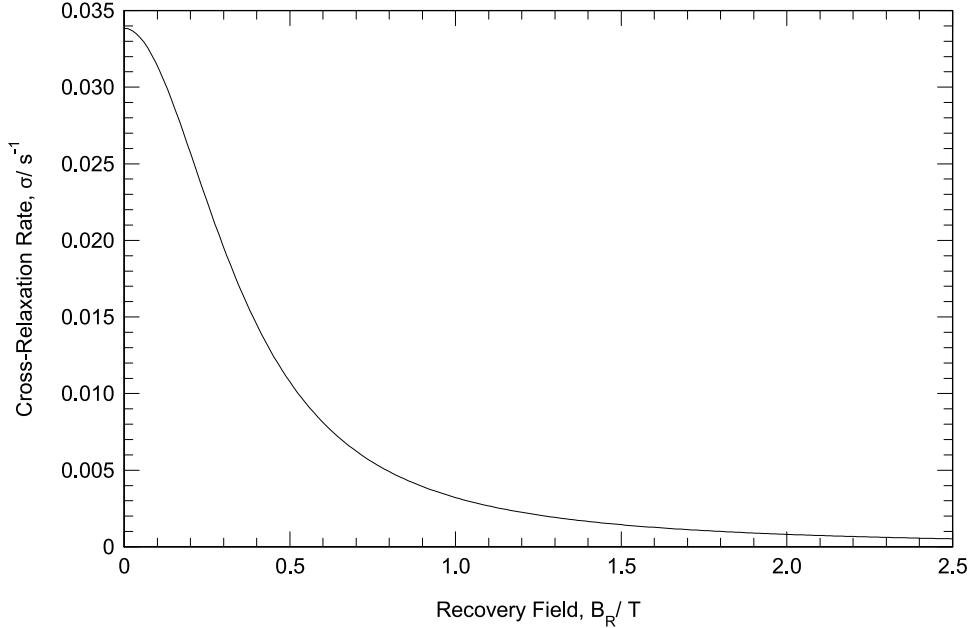


Figure 5.3: Cross-relaxation rate of  $^{13}\text{C-BA}$  as a function of field at 20 K, calculated from equation (2.53) based on parameters in table 5.1.

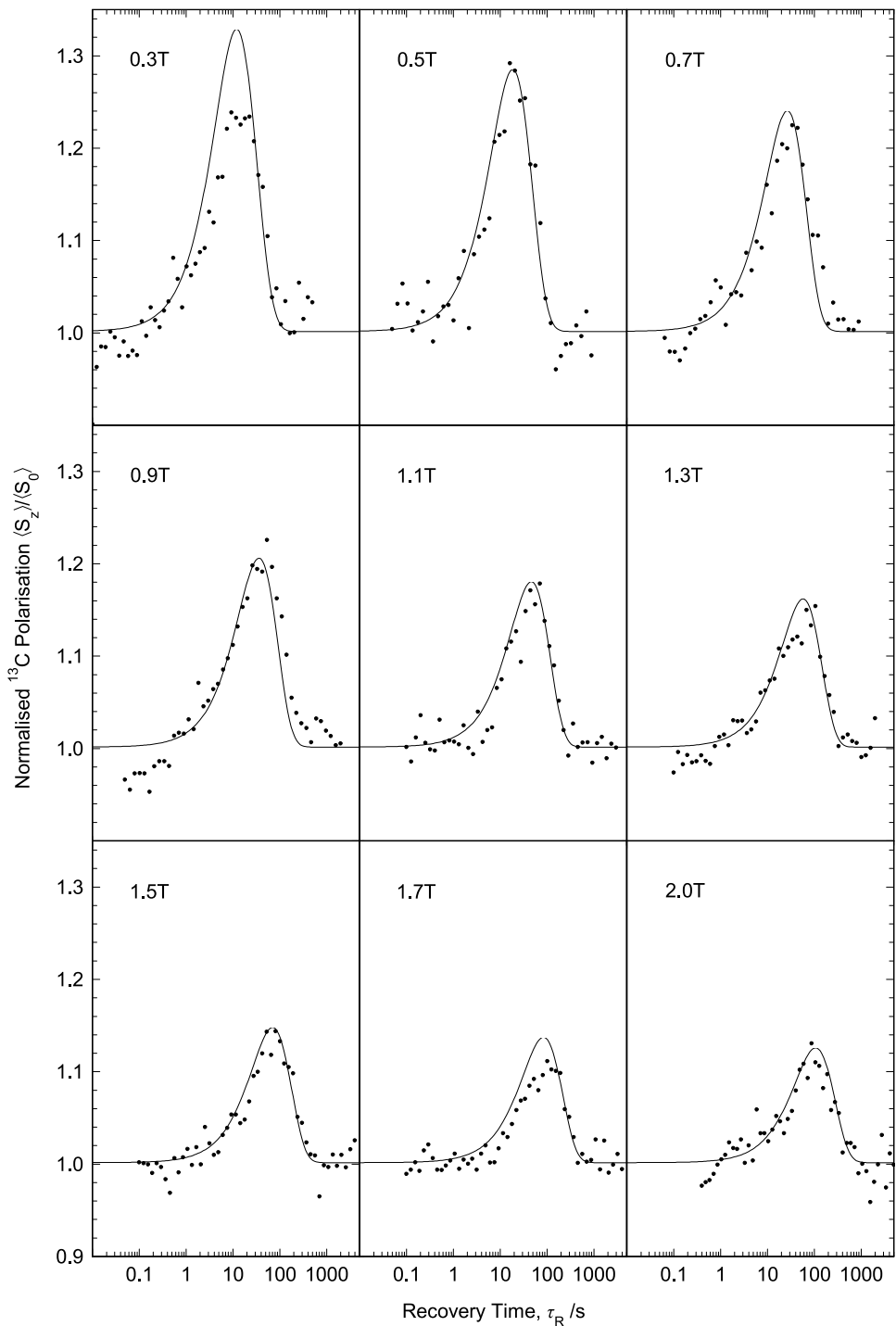


Figure 5.4: Measured magnetisation recovery of <sup>13</sup>C spins in <sup>13</sup>C-BA during the cross-relaxation pulse sequence (subsection 3.3.6) at several recovery fields shown as points. Solid lines calculated from equation (2.26b) based on parameters in table 5.1.

### 5.3.2 2,4,6-Trifluorobenzoic Acid

Figure 5.6 shows the results from measuring the 2,4,6-FBA spin-lattice relaxation across a wide range of temperatures. The region of interest lies below c.a. 40 K where clear evidence of a significant cross-relaxation rate is found in the form of reliably identifiable relaxation rates  $R_1$  and  $R_2$ . Above those temperatures, the negligible weighting coefficient  $c_2^I$  makes separation of these rates unfeasible. The apparent secondary relaxation peak at around 28 K is likely due to the  $L(\omega_H - \omega_F)$  component of the relaxation, conferring a much broader spectral density contribution than the others due to  $\omega_H \approx \omega_F$ . Such secondary minima are also observed in similar samples of 2,3,5,6-FBA [29] and tetrafluoroterephthalic acid (TFTA) [31].

As mentioned earlier in this section, the cross-relaxation experiment data was analysed by fitting to equation (3.3), under the constraint of  $c_2 = -c_1$ . The measured relaxation rates and weighting coefficient  $c_1^I$  were then combined using equation (2.28) to extract the off-diagonal relaxation matrix element. This cross-relaxation rate measured as a function of field at 18 K, is shown in figure 5.5, and is of the same order of magnitude as measured for 2,3,5,6-FBA at the same temperature. Also, the broad difference-frequency Lorentzian component,  $L(\omega_H - \omega_F)$ , which is expressed in the cross-relaxation rate as a negative contribution, can be seen to dominate above c.a. 0.1 T. This negative  $\sigma$  results in the fluorine spin reservoir coming to thermal equilibrium quicker, since polarisation is also transferred from the proton spins as well as the lattice.

A complete model of the dynamics in this sample was made to describe the temperature and field-dependent results based on equation (2.24). At low temperatures, the two relaxation rates can be clearly separated according to equation (2.27), whereas at high temperature the effective relaxation rate is calculated from equation (2.34). The solid and dashed lines on figures 5.5 and 5.6 show that that model parameters, as seen in table 5.2, describe the data reasonably well at low and high temperatures. The secondary minimum at intermediate temperatures is however poorly modelled. This discrepancy is indicative of the inadequacy of standard relaxation theory, based on the high-field approximation, at the low frequencies associated with the  $L(\omega_H - \omega_F)$  component.

These results add to earlier work on TFTA [31, 32], and other fluorobenzoic acid compounds [29], not all of which exhibit cross-relaxation behaviour. Such studies should lead to an increased understanding of the source of strong

intra-reservoir coupling in heteronuclear samples, and further its application in NMR.

2,4,6-FBA	
$C_{II}$	$1.2 \times 10^8 \text{ s}^{-2}$
$C_{IS}$	$7.8 \times 10^6 \text{ s}^{-2}$
$k_0$	$1.46 \times 10^7 \text{ s}^{-1}$
$\Delta H/k_B$	69 K
$\tau_{exc}^{-1}$	$1 \times 10^9 \text{ s}^{-1}$
$\Delta E_{exc}/k_B$	150 K
$\tau_{act}^{-1}$	$5 \times 10^{11} \text{ s}^{-1}$
$\Delta E_{act}/k_B$	750 K

Table 5.2: Best-fit parameters used to describe the relaxation observed in 2,4,6-FBA.

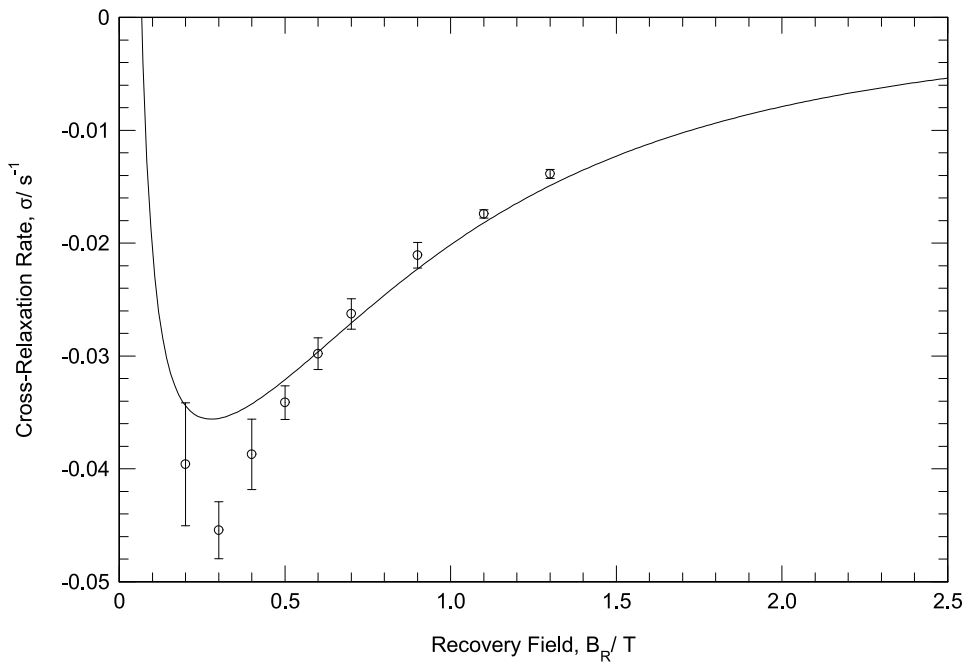


Figure 5.5: Cross-relaxation rate of 2,4,6-FBA measured as a function of field at 18 K shown as points. Solid line modelled using equation (2.54) based on parameters in table 5.2.

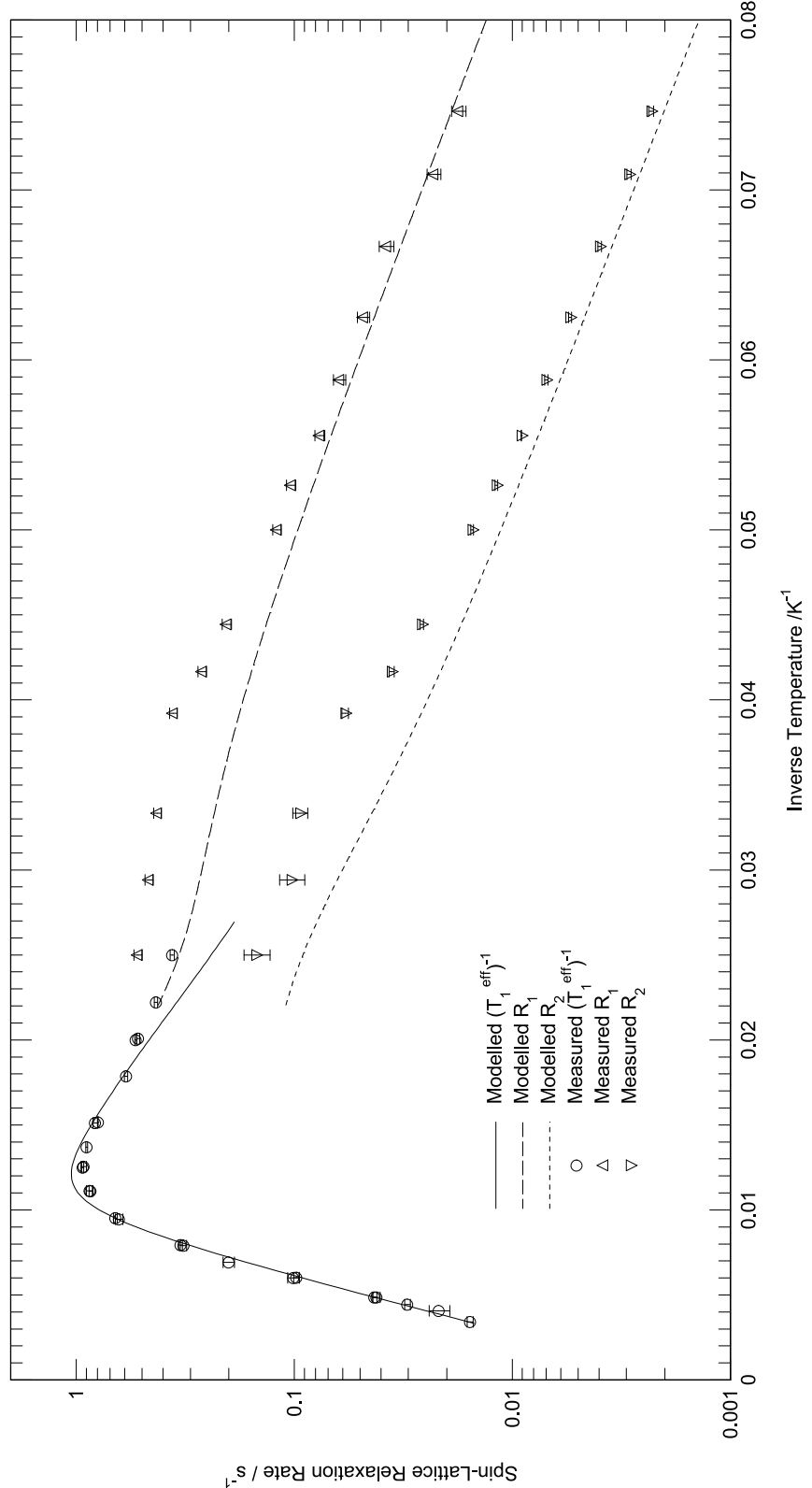


Figure 5.6: Spin-lattice relaxation rates of 2,4,6-FBA measured at  $B_R = 0.61$  T as a function of temperature, shown here as points. The heteronuclear relaxation rates,  $R_1$  and  $R_2$ , (dashed lines) are modelled based on equation (2.27), using parameters in table 5.2. The same parameters are used to calculate the effective relaxation rate,  $T_1^{\text{eff}}$ , (solid line) according to equation (2.34).

## 5.4 Summary

Study of the relaxation processes exhibited by carbon nuclei is significant because it is ubiquitous in biological systems, which are a popular subject of NMR analysis due to the non-invasive nature of its techniques. However, because its magnetic isotope is very dilute in natural abundance and interacts weakly with magnetic fields it is important that every step is taken to maximise the  $^{13}\text{C}$  signal strength. In some cases the natural abundance can be increased through isotopic substitution, but this can prove difficult or impossible, especially with studies done *in vivo*. Decreasing the temperature becomes problematic for the stability of biological samples, and strong magnetic fields quickly become prohibitively expensive. When these considerations are taken into account, being able to enhance the  $^{13}\text{C}$  polarisation by inherent molecular processes, even by 25%, can bear far-reaching consequences in terms of time and cost efficiency. The results presented here have demonstrated and measured the extent to which  $^{13}\text{C}$  polarisation can be increased through interaction with a nearby dynamic process, requiring only the proton spins to be saturated beforehand.

Although fluorine is not as prevalent in biological molecules, and has an induced magnetic moment comparable to that of protons, an understanding of heteronuclear interactions gleaned through such studies is nevertheless important. For example, observation of the polarisation transfer pathways can aid the determination molecular structures based on the strength of dipolar coupling, which depends strongly on the nuclear separation. Additionally, the negative cross-relaxation rate measured by these experiments allows the proton spins to recover at an increased rate as polarisation is transferred from both the lattice than fluorine spins. This can be exploited to expedite the proton magnetisation recovery after measurement and effectively reduce pulse sequence recycle delays.

## Chapter 6

# Short, Strong Hydrogen Bond Motion

### 6.1 Introduction

This study is concerned with compounds that form short, strong hydrogen bonds (SSHBs), typically found to be 2.5 Å in length. Gradual temperature-dependent migration between 300 K and 15 K of the hydrogen in such a bond has been recently measured by neutron diffraction in several compounds [33]. This occurs as the proton moves from the vicinity of one heteroatom to the other it shares a bond with, undergoing a total displacement of about 0.1 Å. Meanwhile, the separation of the heteroatoms in the hydrogen bond remains roughly constant with temperature, and cannot account for this migration.

Molecular dynamics (MD) simulations [33] of such compounds have shown that the high-temperature structures, in which the proton has migrated, are stabilised by lattice vibrations present at those temperatures. At intermediate temperatures during this process, the proton goes through a bistable regime where it is closest to either one of the heteroatoms, whilst avoiding an unstable central position. As a time average, the occupancy of these two sites is also observed to be approximately equal. Based on this information it was decided to elucidate the proton dynamics in this intermediate stage from spin-lattice relaxation measurements.

The specific compound studied here was pyridine-3,5-dicarboxylic acid (3,5-PDA). In the solid state this molecule shares two strong hydrogen bonds with its neighbours, forming infinite two-dimensional planar sheets that are weakly

stacked on each other. Of the two strong hydrogen bonds, only the  $\text{N}\cdots\text{H}-\text{O}$  bond exhibits proton migration, whilst the  $\text{O}\cdots\text{H}-\text{O}$  bond is relatively stationary with temperature. A neutron scattering study of this compound [34] found that the mobile proton tends to be tightly bound to the nitrogen atom at low temperature, forming a hydrogen bond with the nearby oxygen; whereas at high temperature it is closest to the oxygen without the nitrogen-oxygen separation having changed significantly, as shown in figure 6.1.

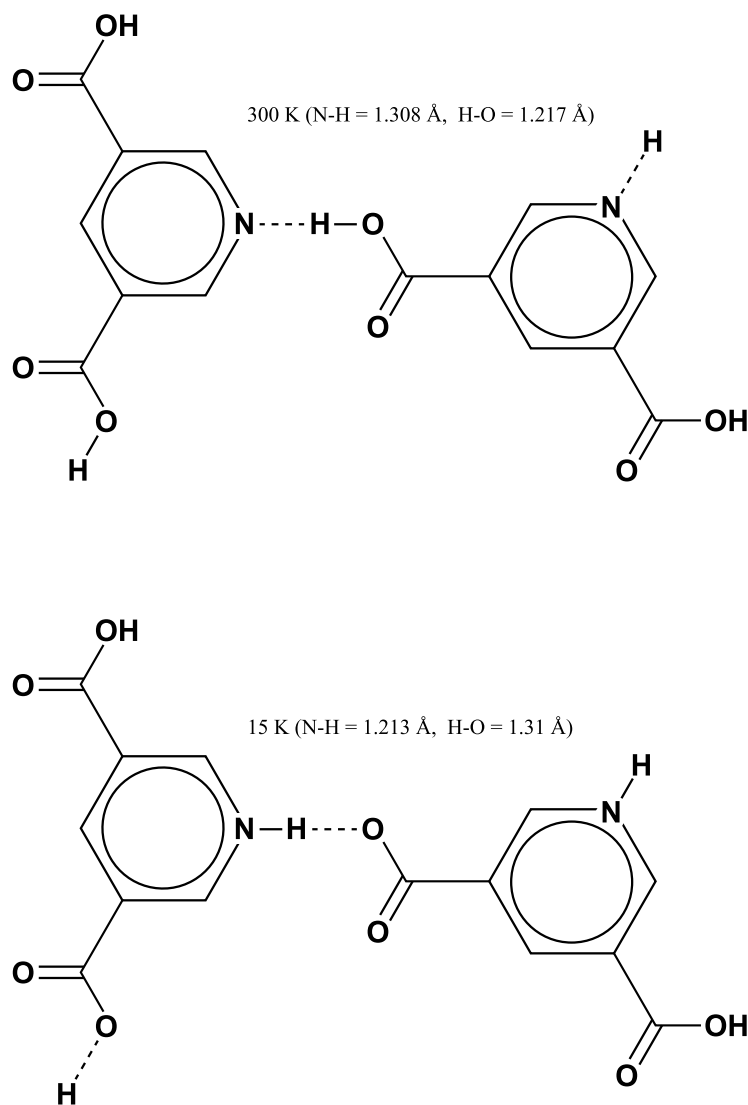


Figure 6.1: Two molecules of 3,5-PDA showing the temperature-dependent migration of protons in the  $\text{N}\cdots\text{H}-\text{O}$  hydrogen bond [34].

As part of the molecular dynamics simulation of 3,5-PDA [33], the potential energy environment of the mobile proton was modelled in three positions along the transfer coordinate, close to the nitrogen, in the middle, and close to the oxygen. It can be seen from figure 6.2 that the proton experiences a single-well potential, which changes significantly with its position along the transfer coordinate. This is in contrast to the case of benzoic acid, where the PES is a double-minimum well, and is relatively stable irrespective of the proton position [7]. The potential well profiles in figure 6.2 were measured relative to each potential minimum rather than relative to each other, hence they appear to have equivalent energy minima. Based on the bistable time-average distribution of the proton position, it can be inferred that at intermediate temperatures the potential minimum of the central position is much higher than the other two. This would then imply that the DMP model for proton transfer could be applied to describe this motion.

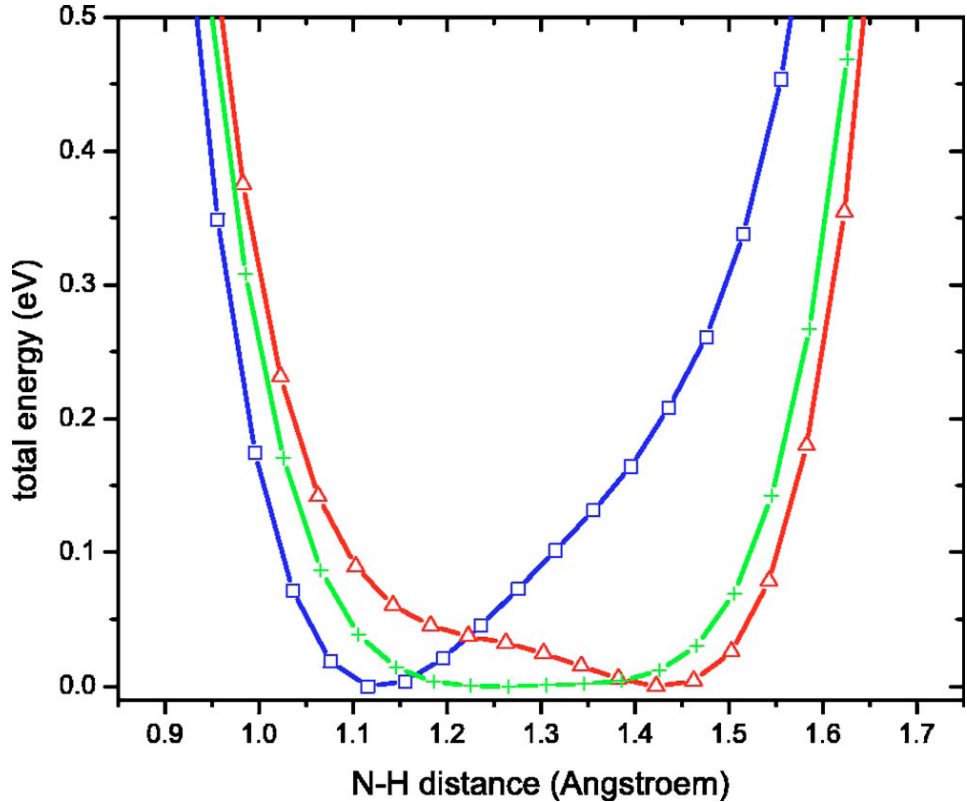


Figure 6.2: Simulated potential energy experienced by the mobile hydrogen bond proton in 3,5-PDA. Three positions along the transfer coordinate are modelled: close to the nitrogen (blue squares), close to the oxygen (red triangles), and a central position (green crosses). Figure taken from [33].

The MD computational analysis on 3,5-PDA also revealed specific molecular vibrational modes that were responsible for stabilising the high-temperature structure, with the proton nearest the oxygen. As discussed in chapter 2, the effective DMP includes contributions from vibrational modes of the molecule that influence proton transfer. Therefore, if the DMP model can be used for this system, then the PES will likely be temperature-dependent. This characteristic can be represented by a non-zero entropy term  $\Delta S$  in the DMP asymmetry, such that at low temperature the nitrogen-vicinity potential is lowest, but gradually increases with temperature such that the oxygen-vicinity potential becomes lowest and more favourable at high temperature.

Further simulations of proton migration in 3,5-PDA found confirmation of DMP characteristics by taking into account contributions from vibrational modes, as shown in figure 6.3. This multi-dimensional PES clearly displays two potential minima approximately 0.1 Å apart along the proton transfer coordinate. However, both minima would not be simultaneously revealed if the transfer coordinate is considered without vibrational mode contributions, as seen in figure 6.2. In other words, the effective PES experienced by the proton along a trajectory from one minimum to the other, requires a translation along the vibrational coordinate as well as the proton transfer coordinate. This then forms an asymmetric double-minimum potential well that can conceivably facilitate incoherent tunnelling.

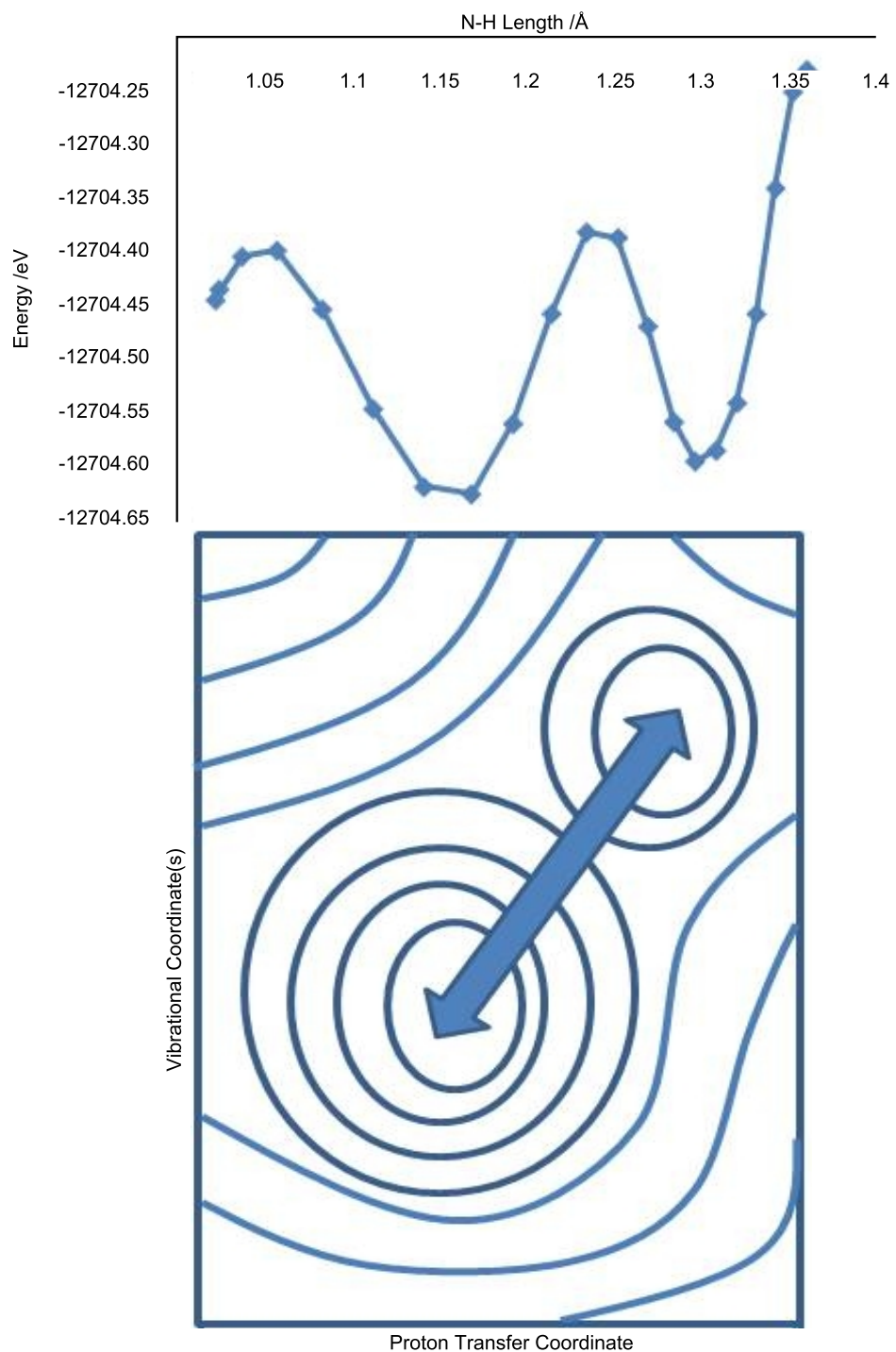


Figure 6.3: Simulated multi-dimensional PES experienced by the mobile hydrogen bond proton in 3,5-PDA (below), and the energy profile traced along the path between minima (above). Figure adapted from personal communication with Mark Johnson, Institut Laue-Langevin.

## 6.2 Experimental Procedure

Close proximity of the nitrogen atom to the mobile proton in the hydrogen bond introduces a heteronuclear reservoir to the relaxation dynamics. In the context of this investigation, the heteronuclear aspects of this sample were of little interest, but presented a challenge to the task of accurately determining the characteristics of proton motion. Preliminary experiments showed it was important to systematically prepare the nitrogen reservoir polarisation at the beginning of each run.

The relatively small magnetogyric ratio of nitrogen meant that its resonance field,  $B_R \approx 12$  T, was beyond that achievable by the spectrometer. Lacking the ability to directly irradiate the nitrogen spins, the zero-field heteronuclear saturation recovery pulse sequence (subsection 3.3.5) was therefore used to measure the spectral densities. For the temperature-dependent measurements, the static-field homonuclear saturation recovery pulse sequence (subsection 3.3.1) was found to produce results with no appreciable difference to those done using the zero-field saturation recovery sequence. This can probably be attributed to a negligible cross-relaxation component,  $\sigma$ , of the relaxation matrix at that field.

Rapid motion of the protons in the  $\text{N}\cdots\text{H}-\text{O}$  hydrogen bonds, occurring during their gradual migration with temperature, would induce spin-lattice relaxation in the nearby magnetic nuclei. If such a regime occurs, then the temperature range over which the proton motion is significant should be characterised by a peak in the relaxation rate. Therefore, to determine the extent of the motion, a series of  $T_1$  measurements were made in the range 50 – 200 K, using the static-field saturation recovery pulse sequence (subsection 3.3.1) at 0.864 T.

Several spectral densities were then recorded between 71.43 – 125 K, where the relaxation was most pronounced, and the correlation time measured to determine the rate of the associated motion. These measurements were made using the zero-field saturation recovery sequence (subsection 3.3.5) to ensure the initial polarisations of both Zeeman reservoirs were known for each run. Quadrupolar dips of  $^{14}\text{N}$  were observed to contribute to relaxation at recovery fields below 0.15 T and were omitted from data analysis in order to isolate the dipolar interaction.

The 3,5-PDA sample used was a single crystal, which provided a much larger density of spins than a powder sample, and an increased SNR as a

result. However, using a single crystal also introduced an added complication of angular-dependence to the dipolar coupling constants. The sample was mounted in the probe with the  $c^*$  crystal axis aligned parallel to  $B_0$ .

### 6.3 Results

Magnetisation recovery curves recorded during the temperature-dependent relaxation analysis showed some evidence of multiple relaxation components, which became more pronounced at lower temperature, and were best described by equation (3.3). However, the relaxation rates measured this way had large uncertainties associated with them, and the recoveries could be represented more reliably by some average  $T_1^{eff}$  from fitting to equation (3.2). The results from both types of fitting procedure are shown in figure 6.5. It is expected that these multiple relaxation rates are due to the presence of a heteronuclear spin reservoir.

The temperature-dependence of the  $T_1^{-1}$ , shown in figure 6.5, exhibits a clear single peak at around 105 K, indicating one dominant relaxation process, which was assumed to be the bi-stable proton motion at intermediate temperature. Above 160 K and below 63 K the relaxation rate shows a gradual trend towards a constant value. Such temperature-independent plateau features are generally not observed in other systems using the DMP model, such as benzoic acid, and their source in this sample was not clear.

Due to the length of time necessary to prepare the Zeeman reservoir polarisations for each run of the zero-field saturation recovery sequence, the field-dependent relaxation rates could not be measured as accurately as for the temperature-dependent experiments. As a result, only the average spin-lattice relaxation time,  $T_1^{eff}$ , could be measured with reasonable accuracy. The spectral densities from fitting the magnetisation recovery curves to equation (3.2) are displayed in figure 6.4.

These spectral densities appear to have the standard Lorentzian form that would be expected from a single dynamic process. To gauge the defining characteristics of the associated motion, the data were initially fitted to the following simple equation:

$$\frac{1}{T_1} = C [\alpha L(\omega_I, \tau_c) + \beta L(2\omega_I, \tau_c)]. \quad (6.1)$$

This equation is based on the purely homonuclear relaxation of a single crystal (2.46), with unknown amplitude,  $C$ , and unknown dipolar lattice sums  $\alpha$  and  $\beta$ . The results of this initial analysis indicated a temperature-dependent spectral density amplitude, and a decreasing correlation rate that tended towards a constant at low temperature. Both of these aspects indicate dynamics that

could effectively be modelled by a DMP.

To better define the high-temperature correlation rate trend it was decided to record another spectral density at 142.86 K, also shown in figure 6.4. However, due to the long relaxation times involved it was necessary to use the more expedient homonuclear saturation recovery sequence described in subsection 3.3.2. It was known from previous studies [27] that the spectral densities of samples with small cross-relaxation rates, prepared with different initial polarisation conditions, tend to have identical correlation rates and only show a difference in amplitude. This was confirmed experimentally in this sample from spectral densities measured at 83.33 K. Therefore, only the correlation rate measured at 142.86 K was used in further analysis, and the amplitude was disregarded.

### 6.3.1 Spectral Density Function

To measure the spectral density amplitudes and correlation rates more accurately, the spectral density function should encompass all relevant relaxation paths in the system, as illustrated in figure 2.5. However, uncertainties in the data require that some approximations are made to simplify the model.

Simulations of heteronuclear magnetisation recoveries based on equation (2.24) were compared to recorded data. This analysis revealed that the heteronuclear relaxation rate,  $\rho_S$ , and cross-relaxation rates,  $\sigma$ , were about an order of magnitude smaller than homonuclear relaxation  $\rho_I$ . Therefore, as a first-order approximation they can be treated as negligible, and the relaxation equation (2.24) can be reduced to

$$\frac{d}{dt}\langle\hat{I}_z\rangle = -(\rho_{II}^{IS} + \rho_{II}^{II}) [\langle\hat{I}_z\rangle - I_0]. \quad (6.2)$$

A further approximation can then be made due to the large difference between the magnetogyric ratios of nitrogen and hydrogen,  $\omega_I \pm \omega_S \approx \omega_I$ . Taking the single crystal relaxation equations (2.42) and (2.46), and noting that for 3,5-PDA  $I = 1/2$ ,  $S = 1$ , and  $N_J = 5$ , these relaxation rates can be reduced to

the following forms:

$$\begin{aligned}
 \rho_{II}^{IS} &= \frac{\gamma_I^2 \gamma_S^2 \hbar^2 S(S+1)}{24N_I} \left(\frac{\mu_0}{4\pi}\right)^2 \frac{4a}{(1+a)^2} \\
 &\quad \times [L(\omega_I - \omega_S)G_{Het}^0 + 18L(\omega_I)G_{Het}^1 + 9L(\omega_I + \omega_S)G_{Het}^2] \\
 &= \frac{\gamma_I^2 \gamma_S^2 \hbar^2}{60} \left(\frac{\mu_0}{4\pi}\right)^2 \frac{4a}{(1+a)^2} \\
 &\quad \times [L(\omega_I - \omega_S)G_{Het}^0 + 18L(\omega_I)G_{Het}^1 + 9L(\omega_I + \omega_S)G_{Het}^2] \\
 &\approx \frac{\gamma_I^2 \gamma_S^2 \hbar^2}{60} \left(\frac{\mu_0}{4\pi}\right)^2 \frac{4a}{(1+a)^2} [L(\omega_I)G_{Het}^0 + 18L(\omega_I)G_{Het}^1 + 9L(\omega_I)G_{Het}^2]
 \end{aligned} \tag{6.3}$$

$$\begin{aligned}
 \rho_{II}^{II} &= \frac{3\gamma_I^4 \hbar^2 I(I+1)}{2N_I} \left(\frac{\mu_0}{4\pi}\right)^2 \frac{4a}{(1+a)^2} [L(\omega_I)G_{Homo}^1 + L(2\omega_I)G_{Homo}^2] \\
 &= \frac{9\gamma_I^4 \hbar^2}{40} \left(\frac{\mu_0}{4\pi}\right)^2 \frac{4a}{(1+a)^2} [L(\omega_I)G_{Homo}^1 + L(2\omega_I)G_{Homo}^2]
 \end{aligned} \tag{6.4}$$

Labelling the heteronuclear and homonuclear constant pre-factors

$$P_{Het} = \frac{\gamma_I^2 \gamma_S^2 \hbar^2}{60} \left(\frac{\mu_0}{4\pi}\right)^2, \quad \text{and} \quad P_{Homo} = \frac{9\gamma_I^4 \hbar^2}{40} \left(\frac{\mu_0}{4\pi}\right)^2,$$

the total proton relaxation rate can be expressed as a sum of two Lorentzian components  $L(\omega_I)$  and  $L(2\omega_I)$ .

$$\begin{aligned}
 \rho_{II}^{IS} + \rho_{II}^{II} &= \frac{4a}{(1+a)^2} [L(\omega_I)P_{Het}G_{Het}^0 + 18L(\omega_I)P_{Het}G_{Het}^1 + 9L(\omega_I)P_{Het}G_{Het}^2] \\
 &\quad + \frac{4a}{(1+a)^2} [L(\omega_I)P_{Homo}G_{Homo}^1 + L(2\omega_I)P_{Homo}G_{Homo}^2] \\
 &= \frac{4a}{(1+a)^2} [(P_{Het}G_{Het}^0 + 18P_{Het}G_{Het}^1 + 9P_{Het}G_{Het}^2 + P_{Homo}G_{Homo}^1)L(\omega_I) \\
 &\quad + P_{Homo}G_{Homo}^2L(2\omega_I)] \\
 &= \frac{4a}{(1+a)^2} [C_1 L(\omega_I) + C_2 L(2\omega_I)]
 \end{aligned} \tag{6.5}$$

To express this equation in the usual spectral density function form, the

constants  $C_1$  and  $C_2$  should be combined into one dipolar constant  $C_D$ .

$$\begin{aligned}\rho_{II}^{IS} + \rho_{II}^{II} &= (C_1 + C_2) \frac{4a}{(1+a)^2} \left[ \frac{C_1}{C_1 + C_2} L(\omega_I) + \frac{C_2}{C_1 + C_2} L(2\omega_I) \right] \\ &= C_D \frac{4a}{(1+a)^2} [cL(\omega_I) + (1-c)L(2\omega_I)]\end{aligned}\quad (6.6)$$

where the dipolar constant is

$$\begin{aligned}C_D &= C_1 + C_2 \\ &= (P_{Het}G_{Het}^0 + 18P_{Het}G_{Het}^1 + 9P_{Het}G_{Het}^2 + P_{Homo}G_{Homo}^1) + (P_{Homo}G_{Homo}^2),\end{aligned}\quad (6.7)$$

and the weighting coefficient is

$$c = \frac{C_1}{C_1 + C_2}. \quad (6.8)$$

The dipolar coupling strengths  $G$  were calculated from the crystal structure [34], according to equations (2.47 - 2.51); considering only the nearest six proton and three nitrogen sites in the sums. Using these values the dipolar constant and weighting coefficient were then calculated to be

$$\begin{aligned}C_D &= 1.6258 \times 10^7 \text{ s}^{-2}, \\ c &= 0.39176.\end{aligned}$$

### 6.3.2 Further Data Analysis

The dipolar coupling strength sums are very sensitive to small changes in the atom coordinates and it is difficult to assign uncertainties to the calculated values of  $C_D$  and  $c$ . The reduced spectral density function (6.6) was therefore constrained only in terms of the weighting coefficient  $c$ , based on the crystal structure. Measurement of the dipolar constant  $C_D$  and quality of the spectral density fits was then used to gauge the validity of the assumptions made in subsection 6.3.1. The spectral density data was fitted again to the following function:

$$\frac{1}{T_1} = D [0.39176L(\omega_I, \tau_c) + 0.60824L(2\omega_I, \tau_c)]. \quad (6.9)$$

The spectral density amplitudes,  $D$ , shown in figure 6.6, have a distinctive temperature-dependence with a peak at c.a. 106 K. This peak coincides with

the relaxation rate maximum as a function of temperature, seen in figure 6.5. These results can be explained well in terms of the DMP model with non-zero entropy. By performing an unconstrained fit of the amplitudes to

$$D = C_D \frac{4a}{(1+a)^2}, \quad (6.10)$$

where  $a = \exp(\frac{\Delta H - T\Delta S}{k_B T})$ , the relevant parameters were measured to be:

SSHB Proton Transfer	
$C_D$	$(1.18 \pm 0.01) \times 10^7 \text{ s}^{-2}$
$\Delta H/k_B$	$(611 \pm 11) \text{ K}$
$\Delta S/k_B$	$(5.8 \pm 0.1)$

Table 6.1: Best-fit parameters used to describe the peak relaxation observed in 3,5-PDA.

Good agreement of the measured and calculated dipolar constants indicates that the observed spin-lattice relaxation can be attributed with certainty to the SSHB proton motion, rather than some other mechanism. Also, the change in enthalpy  $\Delta H$  measured from this fit is in agreement with the DMP asymmetry from MD simulations shown in figure 6.3.

The role of entropy at stabilising the high-temperature structure and giving rise to maximum proton disorder at c.a. 106 K can be illustrated in terms of proton populations as a function of temperature. In the bi-stable SSHB model the protons mostly occupy the two stable sites, nearest the nitrogen and oxygen atoms, with Boltzmann statistics determining the relative populations,  $p_N$  and  $p_O$  respectively:

$$p_N = \frac{a}{1+a} \quad (6.11a)$$

$$p_O = 1 - \frac{a}{1+a} = \frac{1}{1+a} \quad (6.11b)$$

Using the parameters in table 6.1, these populations are shown in figure 6.6. The low and high-temperature regimes are characterised by the proton populations being predominantly in the vicinity of the nitrogen and oxygen respectively, as measured by neutron diffraction. In the intermediate region however, as the DMP asymmetry tends to zero, the protons undergo rapid motion leading to a peak in relaxation and an equilibration of the populations.

The necessity of a finite entropy term can be demonstrated by attempting to fit the spectral density amplitudes to equation (6.10), whilst constraining

the change in entropy,  $\Delta S$ , to zero. It is clear from the resulting fit, shown in figure 6.7, that the ensuing dipolar constant (y-axis intercept) is more than an order of magnitude larger than the value calculated in subsection 6.3.1, and would give rise to a proportionately higher relaxation peak. In addition, it is impossible to model the observed peak and decrease in the intermediate and high-temperature spectral density amplitudes respectively without an entropy term. Figure 6.7 also shows the resulting oxygen and nitrogen-vicinity site populations, again assuming  $\Delta S = 0$ . Such population distributions are reminiscent of benzoic acid, where equilibration of populations only occurs in the limit of infinite temperature, which is in disagreement with the neutron scattering results for 3,5-PDA [34].

The spectral density correlation rates measured by fitting to equation (6.9) are shown in figure 6.5. Additional correlation rates were also deduced from the relaxation measured as a function of temperature, by constraining equation (6.9) according to the parameters in table 6.1. Then, For each measured value of  $T_1^{eff}$  in the vicinity of the relaxation peak, the equation was solved numerically to extract a correlation time. As can be seen in figure 6.5, the two sets of data are in good agreement, and appear to describe an s-shaped curve. Such a trend in proton transfer motion has not been observed previously, and the mechanism responsible for it remains an open question. The data were found to correlate well with the following phenomenological function:

$$\tau_c^{-1} = 8 \times 10^7 + \frac{8 \times 10^8}{1 + a^{2.5}}. \quad (6.12)$$

It is worth noting that both the high and low temperature turning points in the correlation rate, at 127 K and 83 K respectively, occur at  $|\Delta G| \approx 128$  K. The Debye cut-off frequency for phonon contributions is known to be  $\omega_D \approx 116$  K for benzoic acid [35], and is expected to be of a similar magnitude for 3,5-PDA. When the asymmetry exceeds the Debye frequency, incoherent tunnelling can no longer occur between the two ground states of the DMP. In such a regime, incoherent tunnelling instead happens between the ground state of one potential well and an excited state of the other, leading to different proton transfer rates [30]. For a sample with a temperature-dependent asymmetry,  $\Delta G$ , a transition from one tunnelling state to the other is expected to occur at  $\Delta G \approx \pm \omega_D$ . However, further theoretical analysis will be necessary to identify the exact mechanism observed in this sample.

### 6.3.3 Data Modelling

To model the relaxation caused by the SSHB proton transfer, the full coupled heteronuclear relaxation equation (2.24) was used, together with the single crystal relaxation matrix elements derived in subsection 2.3.1. In order to account for the slight discrepancy between the calculated and measured dipolar constants, the calculated dipolar coupling strengths  $G$  were multiplied by an adjustment factor of  $C_D^{Meas}/C_D^{Calc}$ . The DMP asymmetry was calculated based on the measured parameters in table 6.1, and the correlation rates were described by equation (6.12).

To calculate the heteronuclear relaxation rates  $R_1$  and  $R_2$ , the initial spin reservoir polarisations needed to be known. The zero-field saturation recovery pulse sequence ensured that the spectral densities were consistently recorded with  $\langle \hat{I}_z \rangle_{t=0} = 0$   $\langle \hat{S}_z \rangle_{t=0} = 0$ . Conversely, for the temperature-dependent measurements the initial polarisation condition of the nitrogen spin reservoir was unknown. However, it was assumed that this reservoir was relatively undisturbed during the static-field experiments, due to a small cross-relaxation rate, and the initial polarisations were taken to be  $\langle \hat{I}_z \rangle_{t=0} = 0$   $\langle \hat{S}_z \rangle_{t=0} = S_0$ . From these heteronuclear relaxation rates, the average  $T_1^{eff}$  was then calculated according to equation (2.34).

It can be seen from figures 6.4 and 6.5 that the average spin-lattice relaxation,  $T_1^{eff}$ , agrees well with the spectral density data, and temperature-dependent data in the region of interest. This justifies the assumptions made in subsection 6.3.1, and validates the dynamics parameters in subsection 6.3.2 measured using the reduced spectral density function. The disagreement observed between the measured and calculated heteronuclear relaxation rates could not be reconciled in terms of a slight misalignment of the crystal relative to the magnetic field. It is however possible that the crystal is twinned into two domains with slightly different orientations, one of which is larger than the other and dominates the relaxation, represented by the average  $T_1$ .

Figure 6.5 shows that the current model does not adequately describe the trend towards a constant relaxation rate at high and low temperatures. It is difficult to ascribe a temperature-independent relaxation rate in terms of a particular dynamic process, and this data is likely due to background relaxation. Conducting spectral density measurements at lower temperatures could reveal additional Lorentzian components to characterise this relaxation, but the small relaxation rates would likely make such experiments unfeasible.

## 6.4 Summary

Hydrogen bonds akin to the ones studied here are known to be vital in bonding and reactions of complex biological molecules such as DNA. When considering studying such systems in detail it becomes imperative to appreciate the dynamics they exhibit in order to advance the field.

Proton migration in 3,5-PDA has been found to be temperature-dependent, caused by different molecular vibrational modes becoming dominant at different temperatures, and defining the multi-dimensional PES within which the proton resides. At around 105 K the proton demonstrated greatest mobility between the two nearby PES minima, when neither site was greatly more energetically favourable than the other, with the dynamics described very well in terms of incoherent tunnelling in a DMP. Furthermore, the non-zero entropy term, revealed clearly from field-dependent measurements, was found to be crucial in describing the proton migration with temperature. It seems incredible that such an inherently complex system, as the subtle competition of two nuclear position equilibria stabilised by molecular vibrations, could be described so concisely within the framework of the DMP model.

The experiments presented here posed a significant technical challenge due to the inherent heteronuclear effects; requiring the lengthy zero-field saturation recovery pulse sequence to be employed to maintain known initial polarisation conditions for accurate data modelling and interpretation. Further experiments on such molecular systems would be made more efficient if the nitrogen spins could be directly manipulated with RF pulses.

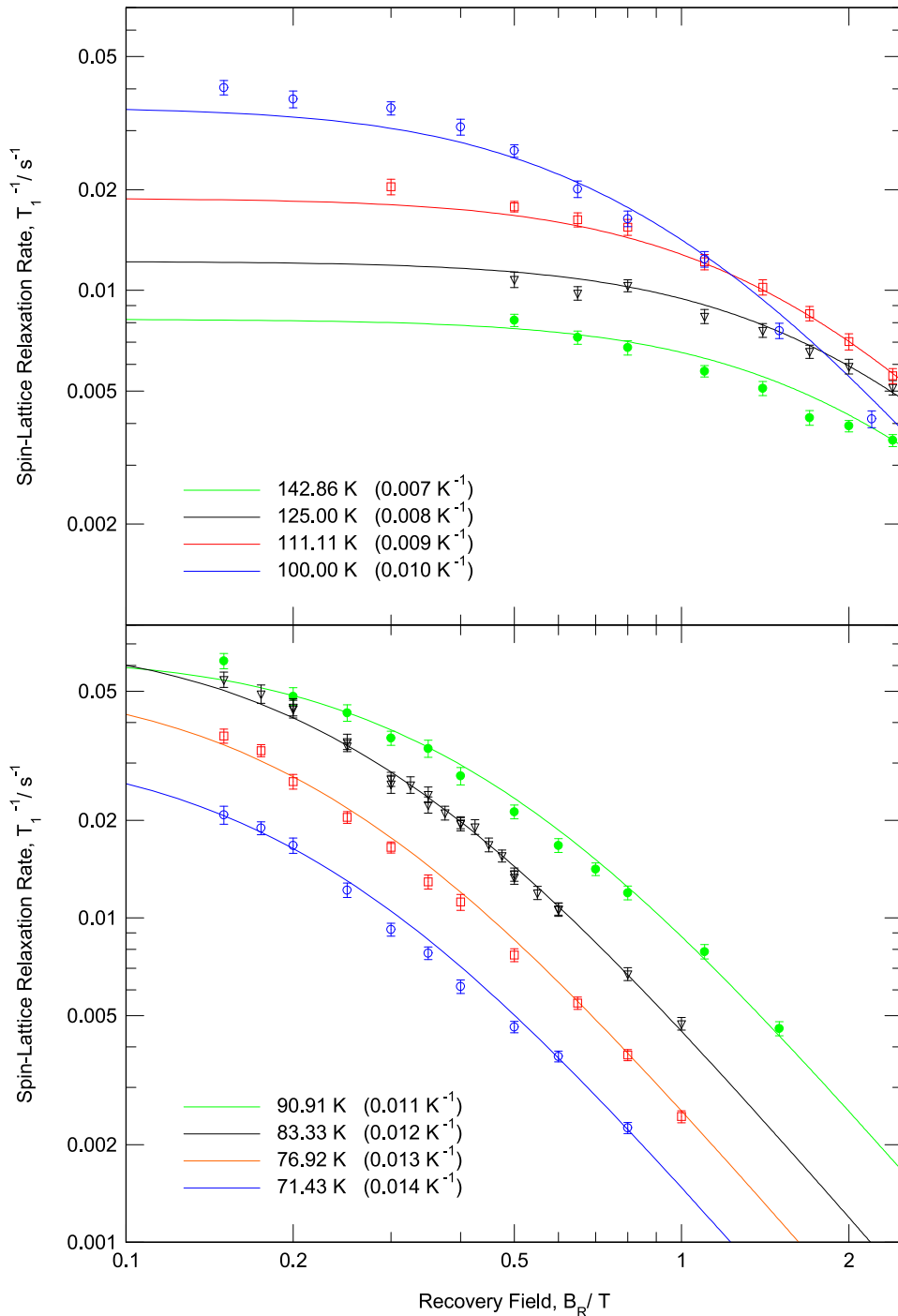


Figure 6.4: Spectral densities of 3,5-PDA measured across a range of temperatures, shown as points. Each solid line is the modelled proton relaxation rate at that temperature according to equation (2.24). The dynamics parameters in table 6.1 were used, and the correlation rate described by equation (6.12). The spectral density at 142.86 K was recorded using the homonuclear saturation recovery pulse sequence.

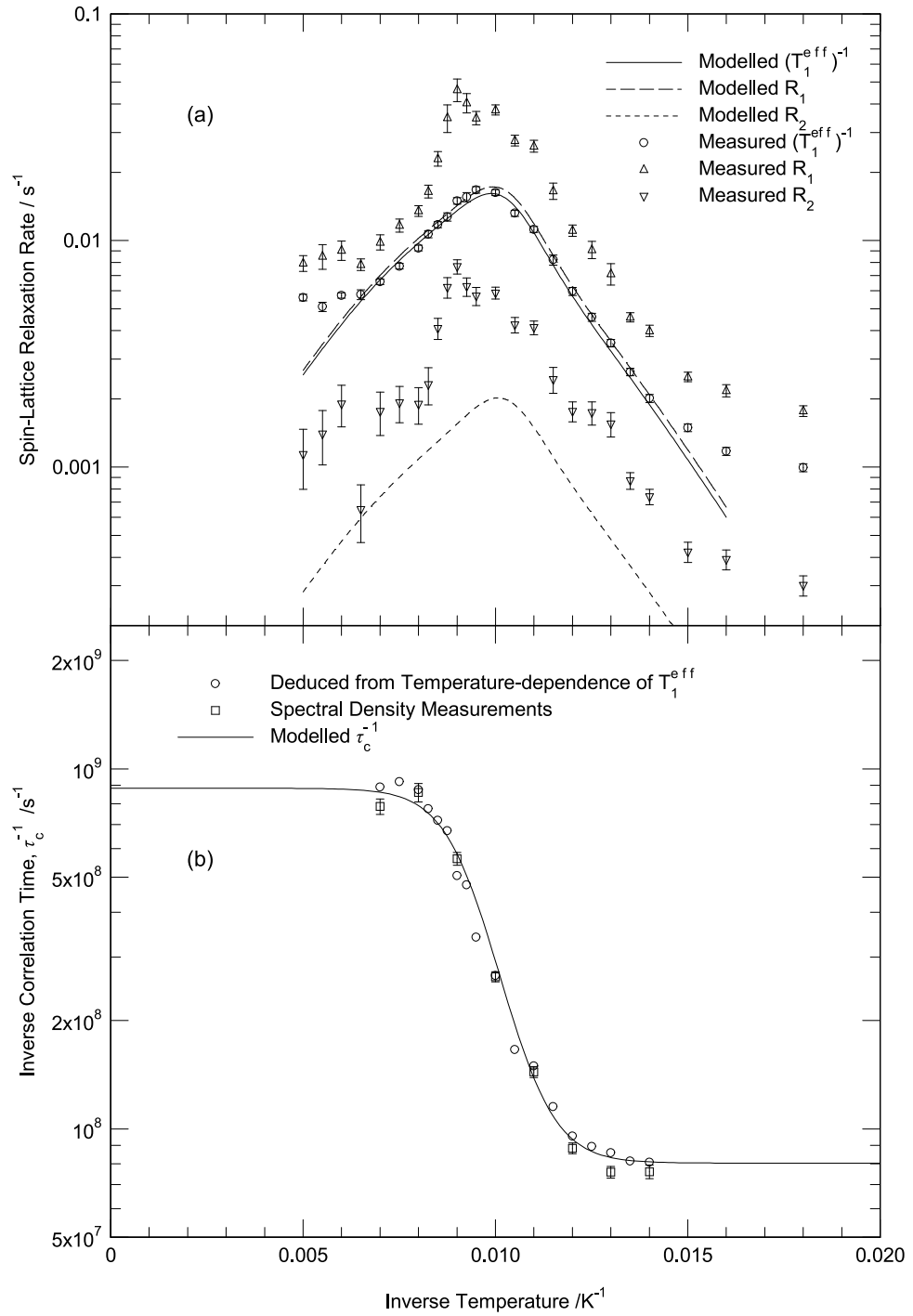


Figure 6.5: (a) The temperature-dependent measurements of spin-lattice relaxation rates at  $B_R = 0.864$  T are shown as points. The solid and dashed lines are modelled according to equation (2.24); using parameters in table 6.1 and the correlation rate given by (6.12). (b) Measured correlation rates are shown as points, with the solid line being a phenomenological fit described by equation (6.12).

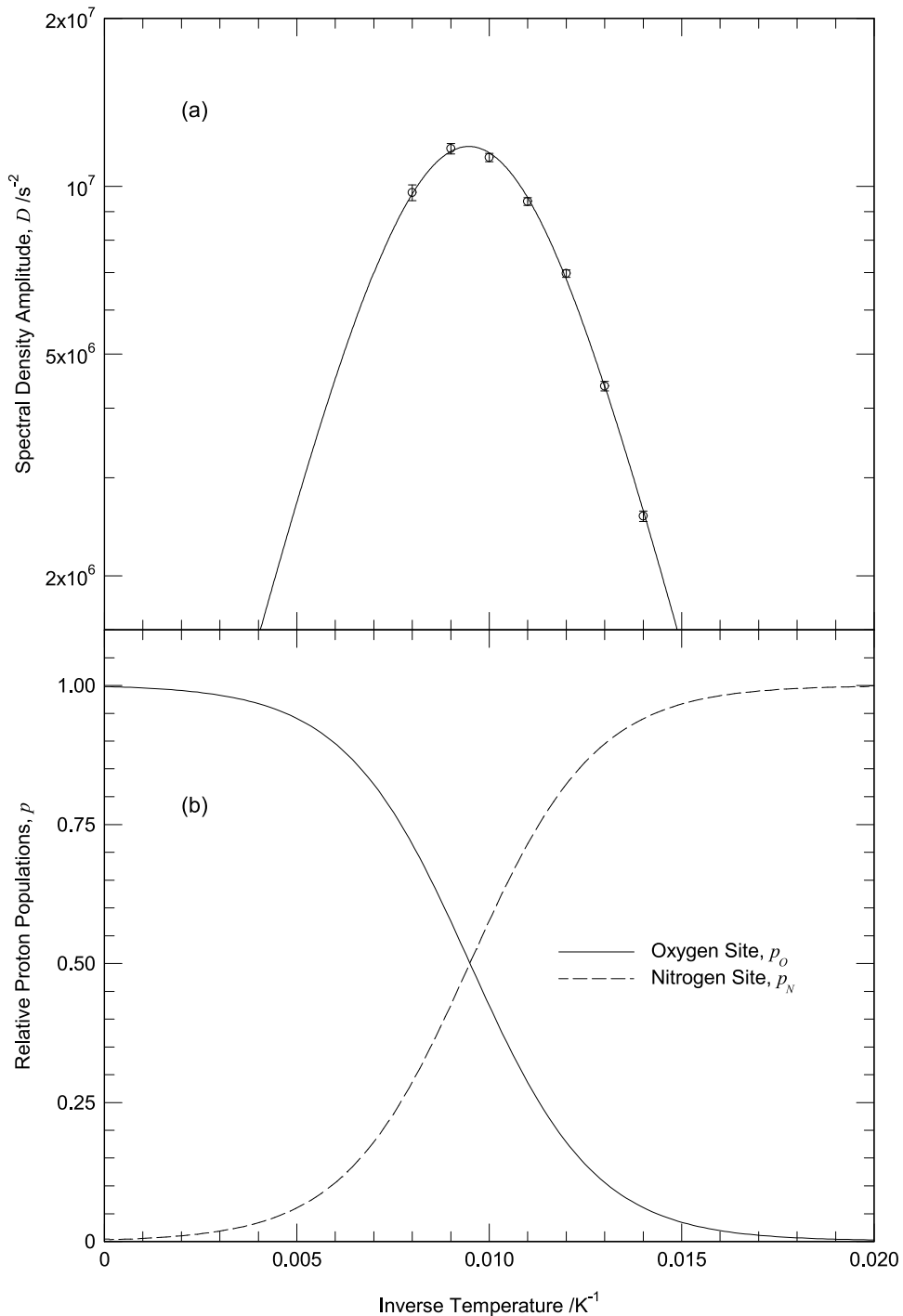


Figure 6.6: (a) Measured spectral density amplitudes represented by points, with the solid line being a fit to equation (6.10), and the resulting parameters shown in table 6.1. (b) Proton populations in the two stable SSHB configurations modelled according to equations (6.11) and the parameters in table 6.1.

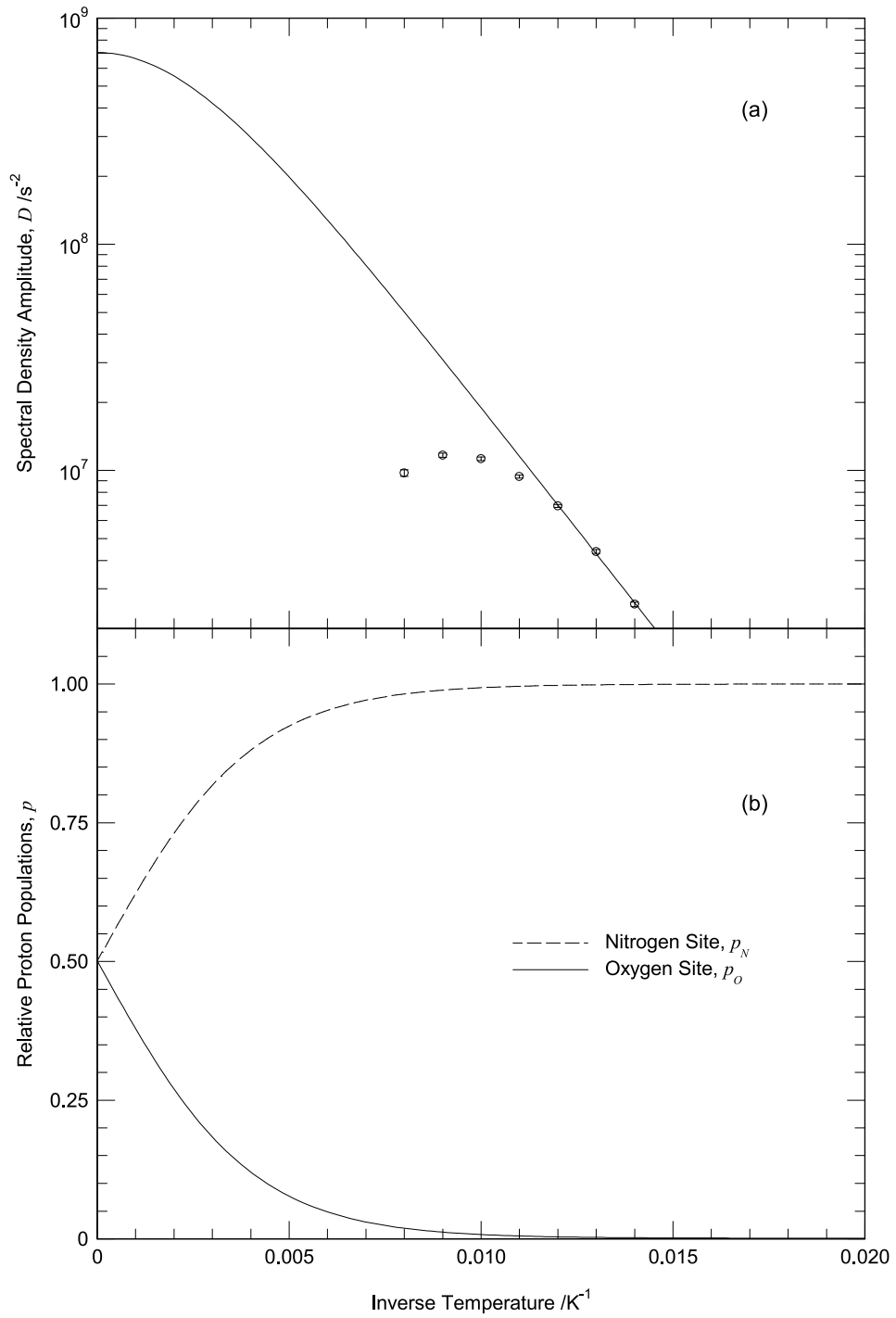


Figure 6.7: (a) Measured spectral density amplitudes represented by points, with the solid line being a fit to equation (6.10) assuming  $\Delta S = 0$ :  $C_D = (7 \pm 2) \times 10^8 \text{ s}^{-2}$  and  $\Delta H/k_B = (500 \pm 20) \text{ K}$ . (b) Proton populations in the two stable SSHB configurations modelled according to equations (6.11) and the above parameters. Comparison to figure 6.6 highlights necessity for finite  $\Delta S$ .

# Chapter 7

## Multiple Relaxation Sources

### 7.1 Introduction

A great advantage of the field-cycling NMR technique is its ability to effectively separate and identify the sources of relaxation within a complex system containing different types of molecular motion [36, 9]. This investigation was designed to test such capabilities on a sample of 4-methylbenzoic acid (4-MBA), also known as *p*-toluic acid, see figure 7.1.

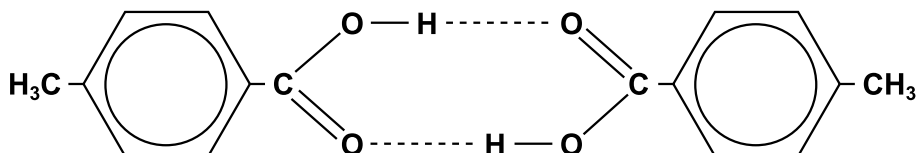


Figure 7.1: Molecules of 4-methylbenzoic acid in a dimer configuration.

Although the relaxation due to proton transfer in carboxylic acid dimers and methyl group rotation are individually well understood [13, 17], the combined case of both processes has received little consideration. One motivation for studying this sample was to determine whether the motion of one group would have any effect on the other.

Current models of the two types of motion involve some PES, on which a particle moves via translation or rotation. These potential energy surfaces are generally assumed to be static and independent of temperature, for both proton transfer in benzoic acid and for hindered methyl rotors. However, in the case of a 4-MBA crystal the two groups are situated relatively close to each other, see figure 7.2, and the PES of one could feasibly be influenced

by the motion of the other. More specifically, the carboxyl proton positions change from being nearly equally distributed between *L* and *R* states at high temperature, to being predominantly in the *L* state at low temperature. This change, if experienced by the methyl rotor PES, would manifest itself as an anomaly in the measured correlation rate, and as a temperature-dependence of the lattice sum dipolar constants,  $C_{AE}$  and  $C_{EE}$ .

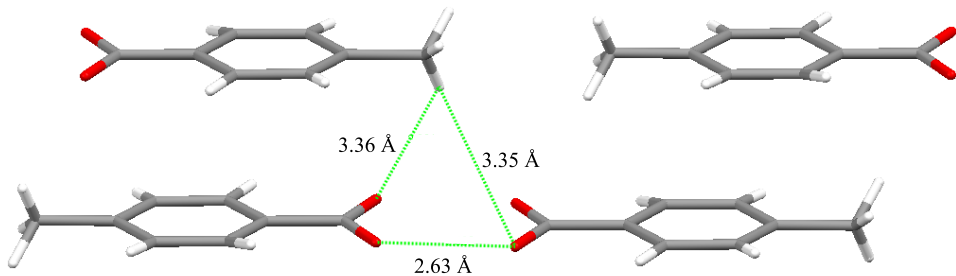


Figure 7.2: Crystal structure of neighbouring 4-MBA molecules [37]. The highlighted internuclear distances show the proximity of a methyl group to the nearest carboxylic dimer.

A combination of temperature-dependent and field-dependent measurements of  $T_1$  would allow any changes to the dynamics to be effectively identified. Knowing that the stochastic motion correlation rate is directly dependent on the PES, measurements of  $\tau_c^{-1}$  from spectral density distributions over a range of temperatures should show whether there is a temperature-dependence to the methyl rotor PES that cannot be described by the static model. Similarly, the spectral density amplitudes give a measure of the dipolar lattice sums, which in the static model should remain constant for all measured temperatures.

Strictly speaking, this set of experiments was concerned only with the relaxation of protons, but for the purposes of keeping within the theme of this thesis the methyl group hydrogens can be considered heteronuclei, providing alternative relaxation pathways. From a mathematical point of view however, efficient spin diffusion is expected within the proton reservoir, which must then be characterised by a single polarisation. Therefore, if there are multiple relaxation pathways from this reservoir to the lattice, then they would be observed as a single-exponential magnetisation recovery characterised by a combined relaxation rate:

$$\frac{1}{T_1^{obs}} = \frac{1}{T_1^A} + \frac{1}{T_1^B} + \dots \quad (7.1)$$

## 7.2 Experimental Procedure

Determining whether a complex temperature-dependent inter-relation between the dynamics of the two types of motion is present required the 4-MBA spectral density profiles to be measured across a wide range of temperatures. Since the main source of relaxation in this sample was the variation of dipolar interactions between hydrogen nuclei, the homonuclear saturation recovery (subsection 3.3.2) and polarisation recovery (subsection 3.3.3) pulse sequences were employed to measure  $T_1$  at high and low recovery fields respectively.

Initially, a measurement of  $T_1$  as a function of temperature at an intermediate field,  $B_R = 1$  T, was made across a broad range of temperatures, 12.82 – 250 K. These preliminary measurements were used to identify the main regions of relaxation and the temperature ranges over which they dominated. Based on this information, 25 spectral densities were then systematically recorded in the temperature range 12.82 – 83.33 K to separate and measure the relaxation components. The range of recovery fields used for each spectral density depended on how much resolution seemed necessary to determine the apparent dynamics at each temperature. Generally speaking, this consisted of 29 spin-lattice relaxation time measurements at recovery fields of 0.08 – 2.3 T.

A powdered sample 4-MBA was used for this set of experiments, which removed the angular dependence of the dipolar lattice sums,  $G$ . The purity of this sample was 98%.

### 7.3 Results

The saturation recovery and polarisation recovery data were analysed using equations (3.2) and (3.4) to measure the  $T_1$ . On a few occasions an apparent discontinuity was revealed in what should be a smooth spectral density profile for a particular temperature. This anomaly was confined to high temperatures where the signal to noise ratio is inherently large and can be attributed to the abrupt change in SNR between polarisation recovery and saturation recovery experiments, as discussed in subsection 3.2.1. Due to time constraints those results could not be improved, but instead introduced slightly greater uncertainty to measurements made during further data analysis of the spectral densities.

The initial spin-lattice relaxation measurements as a function of temperature at  $B_R = 1$  T are shown in figure 7.3. Brief inspection of this data reveals three distinct relaxation components, with peaks at 71.5 K, 35.7 K, and 26.3 K. It is known from previous experiments that for methyl groups the Haupt peak generally appears close to the BPP peak at approximately this recovery field, and always at the high-temperature side of the BPP component. In addition, it is known that a  $T_1$  minimum at around 65 K is typical for a benzoic acid dimer at 1 T. Therefore, these components are most likely due to proton transfer, Haupt, and BPP mechanisms in order of decreasing temperature. However, without the frequency-space resolution provided by recording the  $T_1$  at multiple recovery fields they cannot be assigned with certainty to specific sources of relaxation.

The ground-state tunnelling frequency of 4-MBA has been previously measured by neutron scattering to be  $\omega_t^{(0)} = 81.7 \text{ } \mu\text{eV} = 1.98 \times 10^{10} \text{ rad s}^{-1}$  [38]. According to the methyl thermometer model [39], assuming a purely three-fold potential, this would correspond to a  $T_1$  minimum at c.a. 40 K, in agreement with the previous deduction. Under the same assumption, the high-temperature activation energy can also be estimated from this frequency to be  $E_H/k_B \approx 280 \text{ K}$  [40].

Since the tunnelling frequency is much greater than the maximum proton Larmor frequency at 2.5 T, we can make the approximation  $(\omega_t \pm 2\omega_L)^2 \approx \omega_t^2$ . In this high tunnelling frequency regime the Haupt component of relaxation

from equation (2.63) can be simplified to a field-independent form:

$$\frac{1}{T_1^{AE}} \approx \frac{10\tau_c C_{AE}}{1 + \omega_t^2 \tau_c^2}. \quad (7.2)$$

This means that the Haupt contribution can initially be effectively represented by a constant offset of the spectral density profile that changes with temperature. However, there are too many unknown parameters in this equation to extract exact values from such measurements.

The temperature-dependent contributions from each source of relaxation can be clearly seen in the spectral density profiles in figures 7.4 and 7.5. The highest temperature spectral density appears to be solely due to proton transfer motion, the lineshape being characterised by a single correlation time (width). At lower temperatures, the spectral densities show an increasing constant offset from the distinctive, flat Haupt relaxation component, which becomes dominant at around 33 K. Below this temperature, the BPP component quickly rises in dominance and appears to persist thereafter.

To isolate the parameters governing the dominant features of the observed spin-lattice relaxation behaviour, the relevant temperature ranges were initially considered separately. At high temperatures, in the range 38.46 – 83.33 K, the carboxylic dimer proton transfer provided the largest relaxation component, with some contribution from the Haupt component. Therefore, these spectral densities were fitted to the following equation:

$$\frac{1}{T_1} = D [L(\omega_I, \tau_c^{PT}) + 4L(2\omega_I, \tau_c^{PT})] + b, \quad (7.3)$$

where the constant offset  $b$  accounted for the increasing Haupt component contribution.

If the proton transfer and Haupt components can be effectively separated by the field-cycling technique, then the correlation rate measured using equation (7.3) will be that of the carboxylic dimer. These measurements, shown in figure 7.6, agree qualitatively with the expected trend for a dimer, indicating the validity of this approach.

A measure of the proton transfer rate parameters can then be made by fitting this data to equation (2.62). Also, the spectral density amplitudes,  $D$ , shown in figure 7.7, can be modelled by

$$D = C_{II} \frac{4a}{(1+a)^2}, \quad (7.4)$$

where  $C_{II}$  is the dipolar constant for the dimer (2.60), and  $\Delta G$  is the DMP asymmetry.

Following this, it was attempted to isolate and analyse the BPP component of the methyl group rotation, which appeared to be dominant at temperatures below 25 K. In the high tunnelling frequency approximation, equation (2.63) can be expressed as:

$$\frac{1}{T_1} = C_{EE} [L(\omega_I, \tau_c^{MR}) + 4L(2\omega_I, \tau_c^{MR})] + b, \quad (7.5)$$

where the offset  $b$  again represents the Haupt component. Assuming an effective separation of the relaxation components, then the correlation rate here,  $\tau_c^{MR}$ , would be that of the methyl rotor, shown in figure 7.6. By fitting this data to equation (2.64), and using the high-temperature activation energy derived earlier from the tunnelling frequency, the methyl group correlation rate parameters were deduced.

In the lowest temperature range, 12.82 – 17.24 K, the observed spectral densities could not be fully described in terms of methyl group relaxation, requiring some other source of relaxation that becomes more dominant with decreasing temperature. This new component had the characteristic shape of a BPP-type contribution with a much larger correlation rate than the one observed at higher temperature. To identify the dynamics of this component the spectral densities were analysed with a combined equation for two BPP components:

$$\begin{aligned} \frac{1}{T_1} = & C_{EE} [L(\omega_I, \tau_c^{MR}) + 4L(2\omega_I, \tau_c^{MR})] \\ & + C^N [L(\omega_I, \tau_c^N) + 4L(2\omega_I, \tau_c^N)]. \end{aligned} \quad (7.6)$$

To isolate the dynamics of this new component, the BPP parameters ( $C_{EE}$ ,  $\tau_c^{MR}$ ) known from data at higher temperature were constrained in these fits. As can be seen from figures 7.6 and 7.7, a decreasing spectral density amplitude  $C^N$  and constant correlation rate  $\tau_c^N$  were measured, which are characteristic of a carboxylic dimer rather than a methyl group.

It was considered as a possibility that the new relaxation component was due to the methyl group experiencing a change in its PES, thus affecting its dynamics. However, upon closer analysis of the high-temperature proton transfer correlation rate in figure 7.6, it can be seen that the greatest changes

in carboxyl proton distribution occur above c.a. 30 K, and is predominantly in the *L* configuration below that. Therefore the spectral density changes observed below 17.24 K cannot be attributed to this process.

It is far more likely that the unknown component is due to carboxylic dimers in the vicinity of a crystal lattice defect such as would be created by an impurity in the sample. It is known from previous experiments on benzoic acid, intentionally doped with an optical dye to 0.005%, that the tiny proportion of dimers in their vicinity can be effectively measured due to the different dynamics they exhibit [41]. More specifically, a reduction of the DMP asymmetry  $\Delta G$  and an increase of the ground-state tunnelling rate were observed for the affected dimers. This is in agreement with the measured characteristics of the new component shown in figures 7.6 and 7.7. Considering a 0.005% optical level of impurities had a measurable effect, it is conceivable that the 2% of impurities in this sample would also produce sufficient defects to be detected at low temperature.

### 7.3.1 Data Modelling

In an attempt to fully describe the observed relaxation across all temperatures, a comprehensive model was built to combine the relaxation from the methyl rotor and two different carboxylic dimer environments according to equation (7.1). The parameters measured from preliminary fitting procedures were used as initial estimates at this stage, but required minor adjustment to better describe the overall dynamics. Both the carboxylic proton transfer components were modelled using equation (2.59), with different sets of parameters. The methyl rotor was also modelled fully using equation (2.63). Assuming a purely three-fold methyl hindering potential, with an amplitude of  $V_3$ , the first ten excitation energies and tunnelling frequencies were calculated by numerical diagonalisation of the rotational Hamiltonian eigenvalues [17]. These were then used to calculate the temperature-dependence of the observed tunnelling frequency according to the generalised Allen model [19, 17].

The results of this modelling procedure are shown as solid and dashed lines in figures 7.3 - 7.7, and the parameters used to generate them are displayed in table 7.1. To describe the Haupt component it was found necessary to increase the hindering potential, such that the ground-state tunnelling frequency was reduced to  $\omega_t^{(0)} = 1.06 \times 10^{10} \text{ rad s}^{-1}$ , about half of the previously measured value [38]. Since this frequency is highly-dependent on the hindering potential,

it is therefore likely that the potential is not purely three-fold, and contains contributions with six-fold symmetry. However, quantifying such contributions is beyond the scope of this study. Methyl group coupling effects [42] were also considered as a source of multiple tunnelling frequencies, but such phenomena tend to be restricted to dynamics with much lower hindering potentials.

As can be seen from these figures, the current model of non-interacting methyl rotor and two carboxylic dimer environments describes the data well across all measured temperatures and recovery fields. It has been shown that effective separation of relaxation components can be achieved using field-cycling NMR to measure spectral densities, to the extent of identifying low levels of impurity within the sample. This would be impossible to do with such accuracy based only on the relaxation rate as a function of temperature. In addition, independent measurements of correlation rates can be reliably extracted for each type of motion from spectral density fits in their dominant temperature range. This is best illustrated in figure 7.6, where these independent measurements are in close agreement with those modelled when considering all sources of relaxation simultaneously.

No dependence of methyl motion on the neighbouring carboxylic dimer proton distributions was observed due to being obscured by the bulk proton transfer relaxation component above c.a. 50 K, where these changes are expected to occur. Such a mechanism could be revealed in this temperature range by deuterating the carboxyl protons, thereby reducing the correlation rate and shifting their relaxation component to higher temperature [9].

## 7.4 Summary

The ability to probe spin-lattice relaxation across the frequency domain, utilising field-cycling NMR techniques, has been shown in this study to be invaluable for the accurate measurement and interpretation of dynamics in complex systems. Temperature-dependent analysis has proven to be complimentary to this goal, but is not sufficient on its own, especially for the separation of individual contributing components and their different dynamic rates.

The copious amounts of data, collected across many temperatures and fields during this investigation, also represent a prolonged effort to ensure that the theoretical models used were suitable at accurately describing the entirety of the observed results.

Methyl Rotor	
$C_{AE}$	$4.5 \times 10^8 \text{ s}^{-2}$
$C_{EE}$	$1.7 \times 10^8 \text{ s}^{-2}$
$V_3/k_B$	386 K
$\tau_{0L}^{-1}$	$8 \times 10^8 \text{ s}^{-1}$
$E_L/k_B$	75 K
$\tau_{0I}^{-1}$	$1.8 \times 10^{11} \text{ s}^{-1}$
$E_I/k_B$	165 K
$\tau_{0H}^{-1}$	$1.2 \times 10^{13} \text{ s}^{-1}$
$E_H/k_B$	320 K

Bulk Proton Transfer	
$C_{II}$	$5.59 \times 10^7 \text{ s}^{-2}$
$k_0$	$7.4 \times 10^7 \text{ s}^{-1}$
$\Delta H/k_B$	93.8 K
$\tau_{exc}^{-1}$	$2 \times 10^9 \text{ s}^{-1}$
$\Delta E_{exc}/k_B$	211 K
$\tau_{act}^{-1}$	$1.7 \times 10^{11} \text{ s}^{-1}$
$\Delta E_{act}/k_B$	530 K

Impurity Proton Transfer	
$C_{II}$	$7 \times 10^7 \text{ s}^{-2}$
$k_0$	$5 \times 10^8 \text{ s}^{-1}$
$\Delta H/k_B$	58 K
$\tau_{exc}^{-1}$	$3 \times 10^{10} \text{ s}^{-1}$
$\Delta E_{exc}/k_B$	150 K
$\tau_{act}^{-1}$	$2 \times 10^{12} \text{ s}^{-1}$
$\Delta E_{act}/k_B$	600 K

Table 7.1: Best-fit parameters used to describe the relaxation observed in 4-MBA.

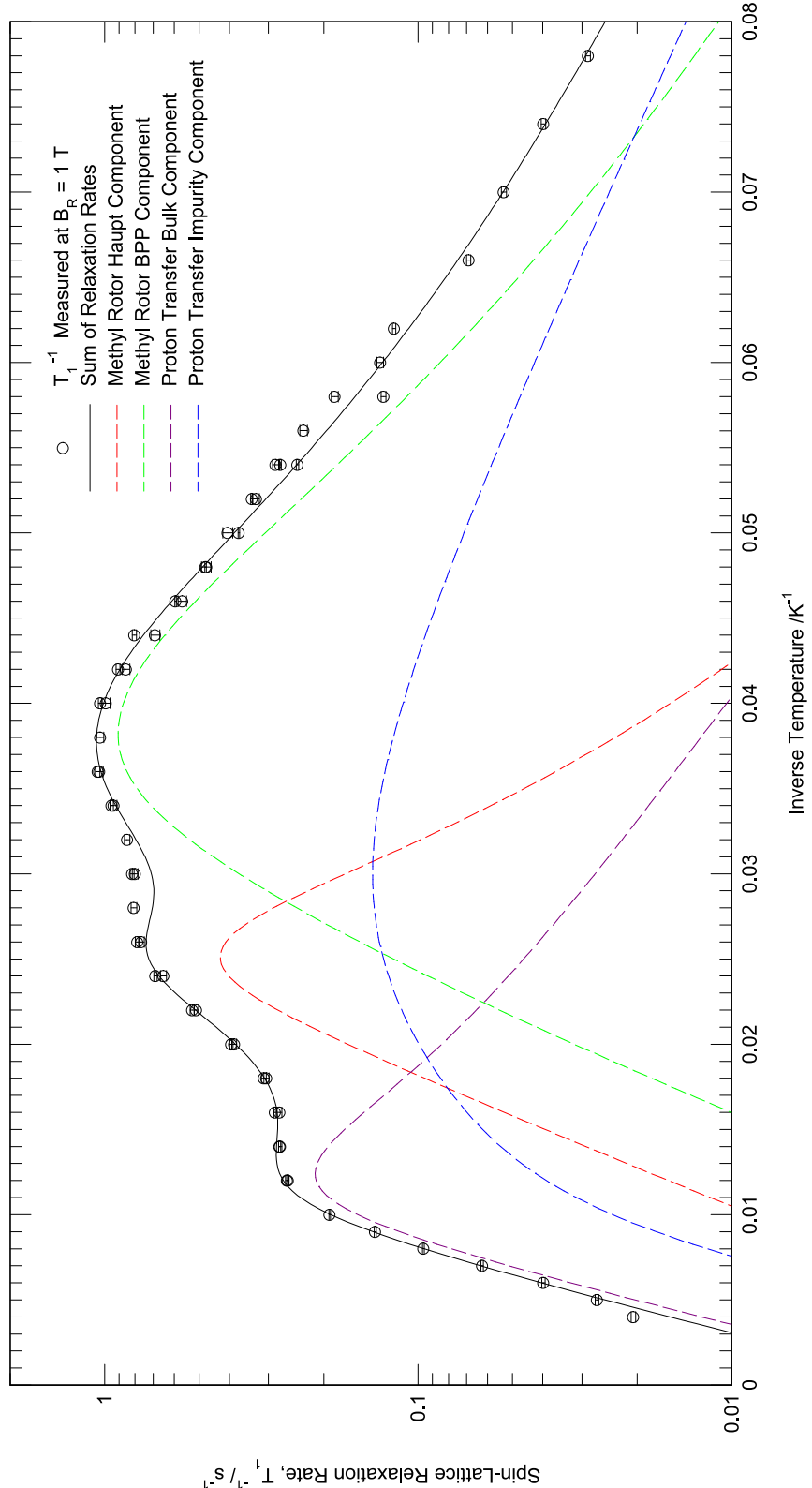


Figure 7.3: The spin-lattice relaxation rate of 4-MBA measured at  $B_R = 1$  T as a function of temperature, shown as open circles. The dashed lines are modelled relaxation components based on equations (2.63) and (2.59), using parameters shown in table 7.1. The solid line is the sum of these components according to equation (7.1).

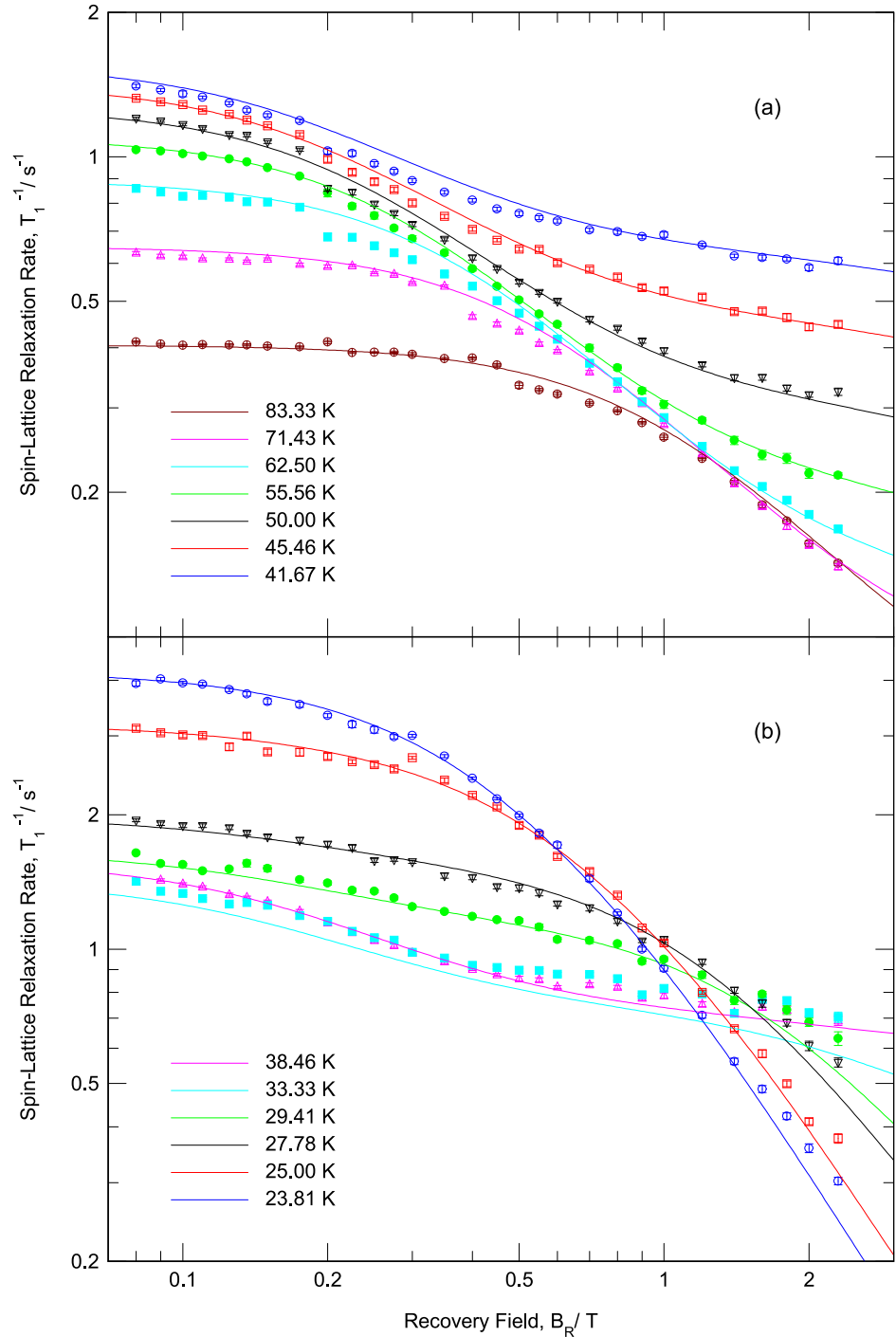


Figure 7.4: Spectral densities of 4-MBA measured across a range of temperatures, shown as points. Each solid line is the modelled relaxation rate at that temperature, and is a sum of components according to equation (7.1). The relaxation components are based on equations (2.63) and (2.59), using parameters shown in table 7.1. (a) Bulk proton transfer and Haupt components are dominant. (b) Haupt and BPP components are dominant.

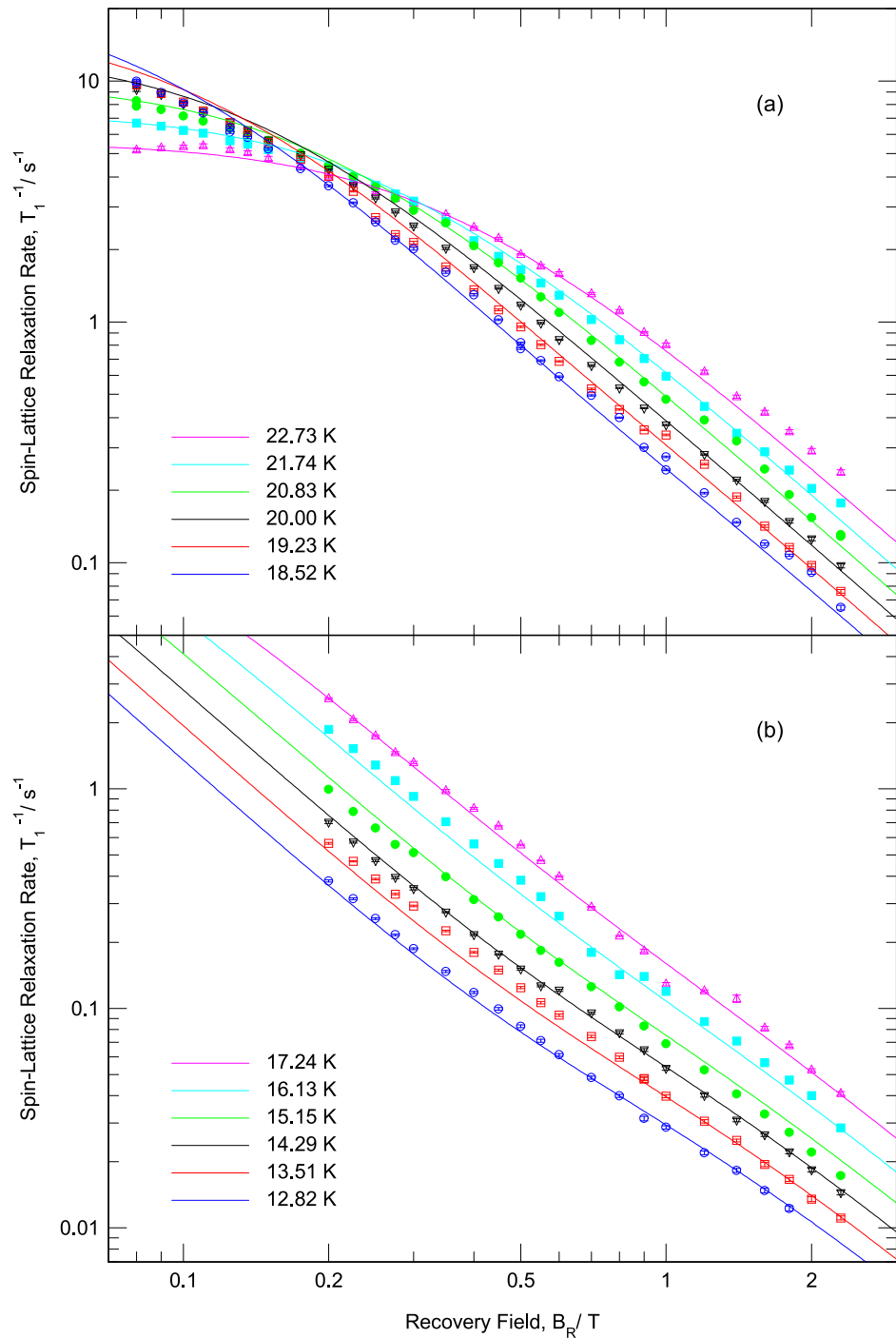


Figure 7.5: Spectral densities of 4-MBA measured across a range of temperatures, shown as points. Each solid line is the modelled relaxation rate at that temperature, and is a sum of components according to equation (7.1). The relaxation components are based on equations (2.63) and (2.59), using parameters shown in table 7.1. (a) Methyl rotor BPP component is dominant. (b) BPP and impurity proton transfer components are dominant.

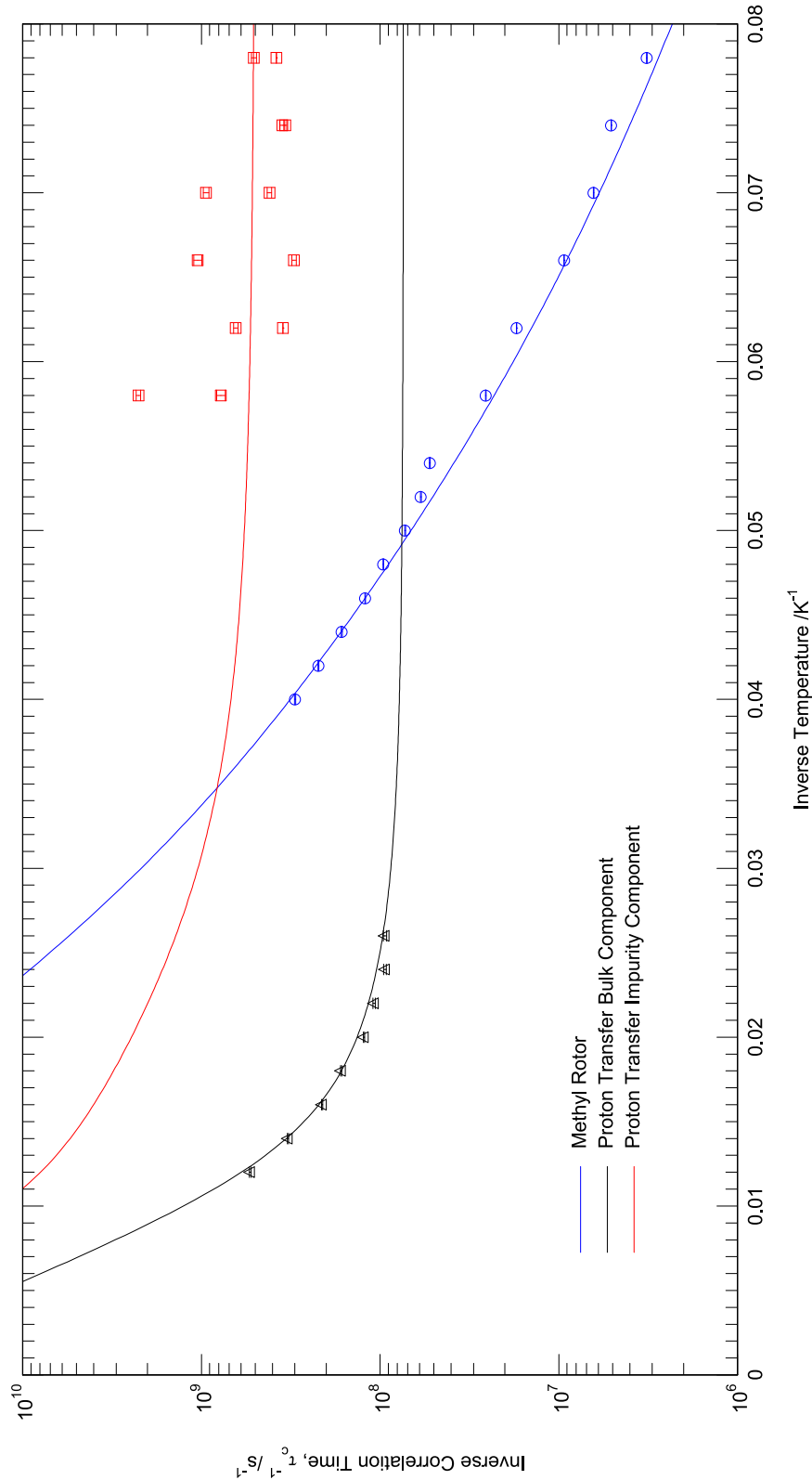


Figure 7.6: Correlation rates for the methyl rotor (circles), bulk proton transfer (triangles), and impurity proton transfer (squares); measured by fitting spectral densities to equations (7.5), (7.3), and (7.6) respectively. Solid lines are modelled based on equations (2.64) and (2.62), using parameters shown in table 7.1.

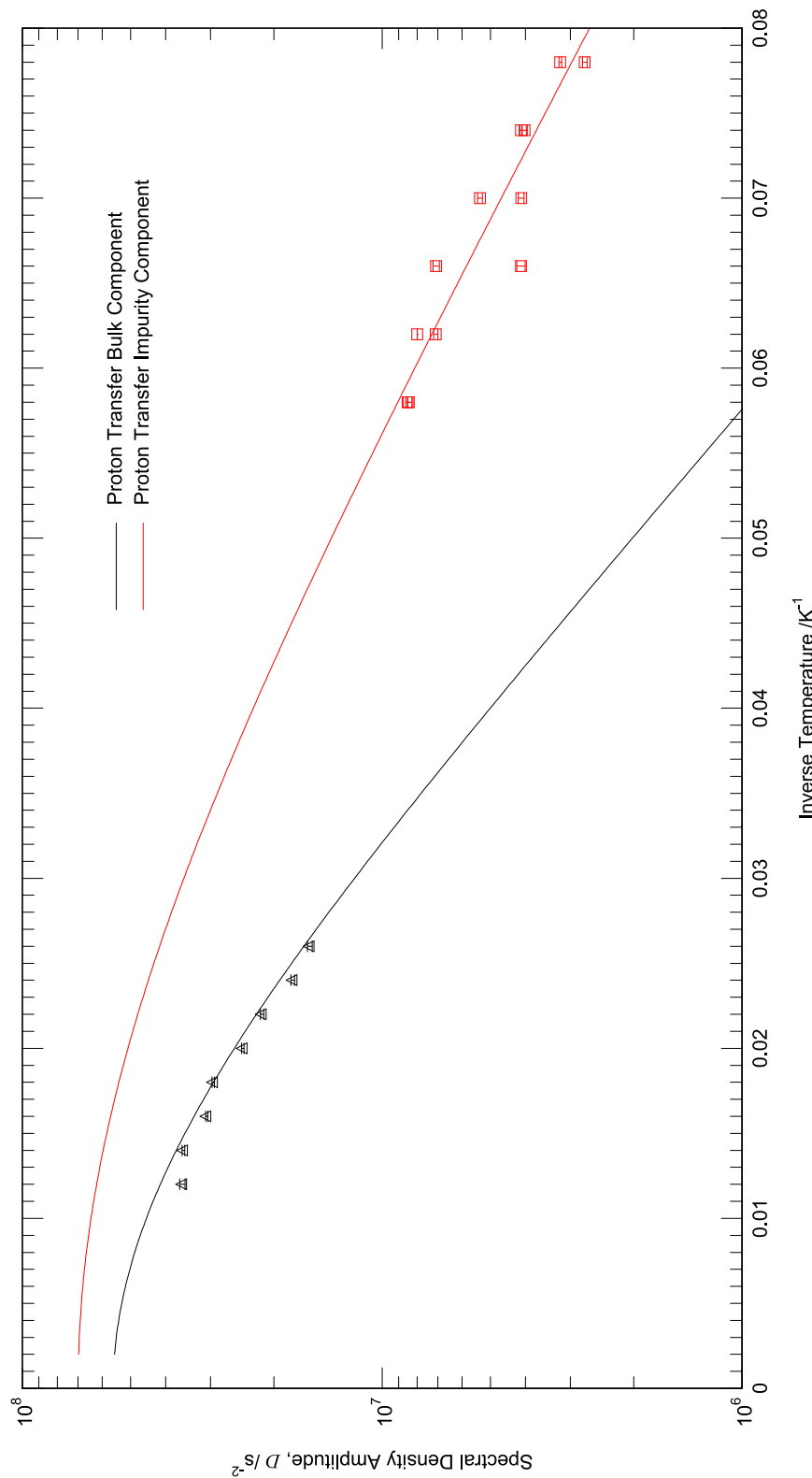


Figure 7.7: Spectral density amplitudes for the bulk proton transfer (triangles) and impurity proton transfer (squares); measured by fitting spectral densities to equations (7.3) ( $D$ ), and (7.6) ( $C^N$ ) respectively. Solid lines are modelled based on equation (7.4) using parameters shown in table 7.1.

## Chapter 8

# Summary and Concluding Remarks

This study, at its core, measured the quantum tunnelling motion of protons in the hydrogen bond. By employing field-cycling NMR techniques to map the spectral density functions of spin-lattice relaxation rates, the proton motion correlation rates were directly measured. In addition, field-cycling facilitated the manipulation and measurement of different spin species reservoirs within the same experiment. A combination of these procedures allowed the heteronuclear effects on quantised proton transfer and coupled nuclear Zeeman reservoirs to be investigated. Effects from both magnetic and non-magnetic nuclear species outside the hydrogen bond were considered.

The isotope effect on proton transfer in benzoic acid, due to isotopic substitution of the carboxyl group oxygen atoms with  $^{18}\text{O}$ , was determined. To ensure all possible differences between the two sets of measurements could only be attributed to the isotope effect, the investigation constituted a careful comparative study on ultra-pure samples. A reduction of the low-temperature correlation rate by  $(15.2 \pm 0.5)\%$  was observed when compared with pure  $^{16}\text{O}$  benzoic acid, indicating that the vibrational modes involving those oxygen atoms contribute constructively to proton transfer. This accurate measurement will be applied to further develop the theoretical understanding and accurate modelling of tunnelling in molecular systems. The isotope effect also induced an observable difference in the dipolar coupling strengths of the two systems, attributed to small changes in their crystal structures.

Two samples,  $^{13}\text{C}$ -enriched benzoic acid and 2,4,6-fluorobenzoic acid, in

which strong coupling between the heteronuclear and proton Zeeman reservoirs has been detected, were the subject of experiments to measure their cross-relaxation rates as a function of field. The off-diagonal relaxation matrix element, characterising the cross-relaxation rate, was found to be negative for 2,4,6-FBA above approximately 0.1 T, due to the strong difference-frequency contribution. Conversely, this spectral density contribution is a lot weaker in  $^{13}\text{C}$ -BA, leading to a positive cross-relaxation rate that enhanced the  $^{13}\text{C}$  polarisation; a 25% increase in the equilibrium magnetisation was observed at 0.3 T. Also, from comparison of  $^{13}\text{C}$ -BA with measurements of pure benzoic acid at low temperature, the isotope effect was estimated to be 8%, but this could equally be attributed to systematic experimental errors.

Recent molecular dynamics studies on gradual temperature-dependent proton migration in the intermolecular N–H $\cdots$ O hydrogen bonds of 3,5-PDA, led to the prediction of a bistable regime at intermediate temperature where relatively fast proton transfer through incoherent tunnelling is expected. Apart from being a different molecular environment, this investigation constituted a deviation from the tunnelling dynamics observed in benzoic acid. The potential energy path linking the two minima, representing the stable proton sites, can only resemble the form of a DMP, within which tunnelling can occur, if vibrational modes of the molecule are considered. Without this translation along the vibrational coordinate, only single-minimum wells are experienced at any point along the proton transfer coordinate.

Heteronuclear effects due to the proximity of  $^{14}\text{N}$  to the mobile proton in 3,5-PDA required that the nitrogen reservoir polarisation was consistently prepared during the experiments, so that the results were reproducible and could be modelled appropriately. The bistable regime hypothesis was confirmed, with a peak in the relaxation rate around 105 K attributed to proton tunnelling. Spectral density measurements also revealed that there was a change in entropy associated with proton transfer between the two stable sites, which made one conformation preferable over the other at each extreme in temperature. The observed correlation rate was akin to no known system and will require further theoretical analysis to understand in terms of first principles.

Separating multiple relaxation sources in 4-methylbenzoic acid presented a challenge to the field-cycling technique that could not have been overcome with only temperature-dependent measurements. The associated dynamic rates of both the proton transfer and methyl rotor motions, extracted from

unconstrained fits of the spectral densities, were found to be very accurate with comparison to modelling of all relaxation sources combined - demonstrating the potency of field-cycling NMR. Furthermore, analysis of the low-temperature spectral densities revealed an additional weak proton transfer component, believed to originate from dimers with distorted PESs around impurity centres. Another facet of this study probed whether the temperature-dependent proton distribution in the carboxylic dimer would have an observable effect on the nearby methyl group potential energy surface. Unfortunately in this case, the temperature region of interest, where the greatest change in proton distribution occurred, was obscured by relaxation from proton transfer in the dimer.

Ab initio calculations of cross-relaxation between Zeeman reservoirs belonging to two different spin-1/2 species showed the possible necessity of additional factors in the off-diagonal relaxation matrix elements. To isolate the cross-relaxation, this hypothetical scenario considered a system of two reservoirs, *I* and *S*, both decoupled from the lattice. Conservation of energy within this isolated system required that the cross-relaxation rates be dependent on the relative reservoir size and magnetogyric ratio dilution factors. More precisely, it is proposed that  $\sigma_{IS}$  is proportional to  $\frac{\gamma_S N_S}{\gamma_I N_I}$ , and  $\sigma_{SI}$  should then be proportional to  $\frac{\gamma_I N_I}{\gamma_S N_S}$ . There was, however, insufficient time to explore such extensions to the theory fully, by considering arbitrary spin species and verification by comparison with results.

# Bibliography

- [1] Andreas Oppenländer, Christophe Rambaud, H. Peter Trommsdorff, and Jean-Claude Vial, “Translational tunneling of protons in benzoic-acid crystals,” *Physical Review Letters*, vol. 63, pp. 1432–1435, 1989.
- [2] Albert W. Overhauser, “Polarization of Nuclei in Metals,” *Physical Review*, vol. 92, pp. 411–415, 1953.
- [3] A. Abragam, *The Principles of Nuclear Magnetism*, Clarendon Press, Oxford, 1961.
- [4] C. P. Slichter, *Principles of Magnetic Resonance*, Springer-Verlag, 1992.
- [5] Malcolm H. Levitt, *Spin Dynamics: Basics of Nuclear Magnetic Resonance*, John Wiley & Sons Ltd., 2005.
- [6] M. A. Neumann, S. Craciun, A. Corval, M. R. Johnson, A. J. Horsewill, V. A. Benderskii, and H. P. Trommsdorff, “Proton Dynamics and the Tautomerization Potential in Benzoic Acid Crystals,” *Berichte der Bunsengesellschaft*, vol. 102, pp. 325–334, 1998.
- [7] V. A. Benderskii, E. V. Vetoshkin, S. Yu. Grebenshchikov, L. von Laue, and H. P. Trommsdorff, “Tunneling splitting in vibrational spectra of non-rigid molecules. I. Perturbative instanton approach,” *Chemical Physics*, vol. 219, pp. 119–142, 1997.
- [8] W. Wu, D. L. Noble, and A. J. Horsewill, “The correspondence between quantum and classical mechanics: an experimental demonstration of the smooth transition between the two regimes,” *Chemical Physics Letters*, vol. 402, pp. 519–523, 2005.
- [9] Q. Xue, A. J. Horsewill, M. R. Johnson, and H. P. Trommsdorff, “Isotope effects associated with tunneling and double proton transfer in the hydro-

## BIBLIOGRAPHY

---

- gen bonds of benzoic acid,” *Journal of Chemical Physics*, vol. 120, pp. 11107–11119, 2004.
- [10] J. L. Skinner and H. P. Trommsdorff, “Proton transfer in benzoic acid crystals: A chemical spinboson problem. theoretical analysis of nuclear magnetic resonance, neutron scattering, and optical experiments,” *Journal of Chemical Physics*, vol. 89, pp. 897–907, 1988.
- [11] D. C. Look and I. J. Lowe, “Effect of hindered molecular rotation between unequal potential wells upon nuclear magnetic resonance spinlattice relaxation times and second moments,” *The Journal of Chemical Physics*, vol. 44, pp. 3437 – 3441, 1966.
- [12] E. R. Andrew and L. Latanowicz, “Solid-state proton transfer dynamics and the proton NMR second moment and proton relaxation rates,” *Journal of Magnetic Resonance*, vol. 98, pp. 232–239, 1986.
- [13] A. J. Horsewill, “Quantum tunnelling in the hydrogen bond,” *Progress in Nuclear Magnetic Resonance Spectroscopy*, vol. 52, pp. 170–196, 2008.
- [14] T.P. Jarvie, A.M. Thayer, J.M. Millar, and A. Pines, “Effect of correlated proton jumps on the zero field nmr spectrum of solid p-toluic acid,” *The Journal of Physical Chemistry*, vol. 91, pp. 2240–2242, 1987.
- [15] C. C. Wilson, N. Shankland, and A. J. Florence, “A single-crystal neutron diffraction study of the temperature dependence of hydrogen-atom disorder in benzoic acid dimers,” *Journal of the Chemical Society, Faraday Transactions*, vol. 92, pp. 24, 1996.
- [16] D. F. Brougham, A. J. Horsewill, and R. I. Jenkinson, “Proton transfer dynamics in the hydrogen bond: a direct measurement of the incoherent tunnelling rate by NMR and the quantum-to-classical transition,” *Chemical Physics Letters*, vol. 272, pp. 69–74, 1997.
- [17] A. J. Horsewill, “Quantum tunnelling aspects of methyl group rotation studied by NMR,” *Progress in Nuclear Magnetic Resonance Spectroscopy*, vol. 35, pp. 359–389, 1999.
- [18] J. Haupt, “Einfluß von quanteneffekten der methylgruppenrotation auf die kernrelaxation in festkörpern,” *Zeitschrift für Naturforschung A*, vol. 26a, pp. 1578, 1971.

## BIBLIOGRAPHY

---

- [19] P. S. Allen, “A model for a temperature-dependent frequency distribution of methyl group tunnelling splittings,” *Journal of Physics C: Solid State Physics*, vol. 7, pp. L22–L25, 1974.
- [20] J. Haupt and W. Müller-Warmuth, ,” *Zeitschrift für Naturforschung A*, vol. 24a, pp. 1066, 1969.
- [21] F. Noack, “NMR field-cycling spectroscopy: principles and applications,” *Progress in Nuclear Magnetic Resonance Spectroscopy*, vol. 18, pp. 171–276, 1986.
- [22] Rainer Kimmich and Esteban Anoardo, “Field-cycling NMR relaxometry,” *Progress in Nuclear Magnetic Resonance Spectroscopy*, vol. 44, pp. 257–320, 2004.
- [23] Qiang Xue, *Proton tunnelling in the hydrogen bond studied by NMR*, Ph.D. thesis, The University of Nottingham School of Physics & Astronomy, March 2003.
- [24] Eiichi Fukushima and Stephen B. W. Roeder, *Experimental Pulse NMR: A Nuts and Bolts Approach*, Addison-Wesley Publishing Company, Inc., 1981.
- [25] Soichi Hayashi and Noriyuki Kimura, “Infrared spectra and molecular configuration of benzoic acid,” *Bulletin of the Institute for Chemical Research, Kyoto University*, vol. 44, pp. 335–340, 1966.
- [26] Lukas von Laue, *Transferts de protons par effet tunnel dans l'acide benzoïque: le rôle des vibrations moléculaires*, Ph.D. thesis, Université Joseph Fourier, 1997.
- [27] W. Wu, D. L. Noble, J. R. Owers-Bradley, and A. J. Horsewill, “A  $^{13}\text{C}$  field-cycling NMR relaxometry investigation of proton tunnelling in the hydrogen bond: Dynamic isotope effects, the influence of heteronuclear interactions and coupled relaxation,” *Journal of Magnetic Resonance*, vol. 175, pp. 210–221, 2005.
- [28] D.L. Noble, I. Frantsuzov, and A.J. Horsewill, “Field-cycling nmr investigations of  $^{13}\text{C}^1\text{H}$  cross-relaxation and cross-polarisation: The nuclear solid effect and dynamic nuclear polarisation,” *Solid State Nuclear Magnetic Resonance*, vol. 34, pp. 110–117, 2008.

## BIBLIOGRAPHY

---

- [29] D. L. Noble, *Field-Cycling NMR Investigations of Proton Tunnelling and Nuclear Spin Relaxation*, Ph.D. thesis, The University of Nottingham School of Physics & Astronomy, September 2006.
- [30] A. J. Horsewill, C. J. McGloin, H. P. Trommsdorff, and M. R. Johnson, “Proton tunnelling in the hydrogen bonds of halogen-substituted derivatives of benzoic acid studied by NMR relaxometry: the case of large energy asymmetry,” *Chemical Physics*, vol. 291, pp. 41–52, 2003.
- [31] A. J. Horsewill, A. Ikram, and I. B. I. Tomsah, “Hydrogen bond dynamics in tetrafluoroterephthalic acid studied by NMR and INS,” *Molecular Physics*, vol. 84, pp. 1257–1272, 1995.
- [32] A. J. Horsewill and W. Wu, “Proton tunneling in a hydrogen bond measured by cross-relaxation field-cycling NMR,” *Journal of Magnetic Resonance*, vol. 179, pp. 169–172, 2006.
- [33] F. Fontaine-Vive, M. R. Johnson, G. J. Kearley, J. A. Cowan, J. A. K. Howard, and S. F. Parker, “Phonon driven proton transfer in crystals with short strong hydrogen bonds,” *The Journal of Chemical Physics*, vol. 124, pp. 234503–234511, 2006.
- [34] John A. Cowan, Judith A. K. Howard, Garry J. McIntyre, Samuel M.-F. Lo, and Ian D. Williams, “Variable-temperature neutron diffraction studies of the short, strong hydrogen bonds in the crystal structure of pyridine-3,5-dicarboxylic acid,” *Acta Crystallographica Section B*, vol. 61, pp. 724730, 2005.
- [35] G. T. Furukawa, R. E. McCoskey, and G. J. King, “Calorimetric properties of benzoic acid from 0 to 410k,” *Journal of research of the National Bureau of Standards*, vol. 47, pp. 256, 1951.
- [36] Cheng Sun, *Quantum dynamics and tunnelling of methyl rotors studied by field-cycling NMR*, Ph.D. thesis, The University of Nottingham School of Physics & Astronomy, 2009.
- [37] M. G. Takwale and L. M. Pant, “The structure of *p*-toluic acid,” *Acta Crystallographica Section B*, vol. 27, pp. 1152 – 1158, 1971.
- [38] M. Prager and A. Heidemann, “Rotational Tunneling and Neutron Spectroscopy: A Compilation,” *Chemical Reviews*, vol. 97, pp. 2933–2966, 1997.

## *BIBLIOGRAPHY*

---

- [39] S. Clough, A. Heidemann, A. J. Horsewill, J. D. Lewis, and M. N. J. Paley, “The rate of thermally activated methyl group rotation in solids,” *Journal of physics C, Solid state physics*, vol. 15, pp. 2495, 1982.
- [40] A. S. Montjoie and W. Müller-Warmuth, ,” *Zeitschrift für Naturforschung A*, vol. 40a, pp. 596, 1985.
- [41] D. F. Brougham, A. J. Horsewill, and H. P. Trommsdorff, “A field-cycling NMR relaxometry investigation of proton tunnelling in a partially disordered system of hydrogen bonds,” *Chemical Physics*, vol. 243, pp. 189–199, 1999.
- [42] Clough, A. Heidemann, A.J. Horsewill, and M.N.J. Paley, “Coupled tunnelling motion of a pair of methyl groups in lithium acetate studied by inelastic neutron scattering,” *Zeitschrift für Physik B Condensed Matter*, vol. 55, pp. 1–6, 1984.